Viscous triple shock reflections relevant to detonation waves, and Detonation dynamics predicted by the Fickett model

doctoral thesis by

Sébastien She-Ming Lau-Chapdelaine

Thesis submitted to the
Faculty of Graduate and Postdoctoral Studies
In partial fulfilment of the requirements
For the Ph.D. degree in
Mechanical Engineering

Department of Mechanical Engineering
Faculty of Engineering
University of Ottawa

Abstract

Two aspects of detonation dynamics are addressed in this thesis by articles. The first part of the thesis investigates shock reflection phenomena believed to be responsible for enhancing reaction rates in detonations, namely Kelvin-Helmholtz instability and Mach stem bifurcation caused by forward jetting. Three papers are presented.

The first numerically investigates shock reflections from a wedge under detonation-like conditions. A state of the art solver of the Euler equations is used. The shock reflection configuration is shown to depend on solver type, wedge implementation, and resolution. The type of reflection (i.e. regular or irregular) is found to depend on corner geometry, even far from the corner, showing initial conditions can play important roles in shock reflections.

These complications are addressed with shock-resolved viscous simulations and a new initial condition: the triple point reflection. The numerical method is demonstrated in the second paper, and the presence of Kelvin-Helmholtz instability is investigated. Viscosity is found to play an important role in delaying the instability, which is found not to be a likely source of reaction acceleration on time scales commensurate with autoignition behind the Mach stem, but may become important on scales associated with the detonation cell.

Mach stem bifurcations are investigated experimentally and numerically in the third paper. Experimental shock reflections are performed from a free-slip boundary in gases with differing isentropic exponents. Bifurcations are found in experiments, viscous and inviscid simulations. Viscosity is found to delay bifurcations. Inviscid simulations are used to approximate the limits of Mach stem bifurcation in the phase space of Mach number, isentropic exponent, and reflection angle. A maximum isentropic exponent is found beyond which bifurcations do not occur, matching the irregular/regular boundary of the detonation cellular structure. Flow field instability is found in experiments at high Mach number and low isentropic exponent.

The second part of the thesis, comprised of one paper, investigates the dynamics of detonations with multiple thermicity peaks using Fickett's detonation analogue. Steady state analysis predicts multiple possible steady states, but only the fastest is singularity-free. Simulations show other solutions develop shock waves that eventually establish a detonation travelling at the fastest velocity allowed by the generalized Chapman-Jouguet criterion. Characteristic and linear stability analysis shows these shocks are found to arise due to instability at the sonic points.

Résumé

Deux aspects de la dynamique des détonations sont soulevés dans cette thèse par articles. La première partie de cette thèse est une étude des phénomènes impliqués dans la réflexion d'ondes de choc, suspectées d'être responsables de l'accélération des réactions dans les détonations, à travers des instabilités de Kelvin-Helmholtz et la bifurcation du 'Mach stem' causée par un jet. Trois articles sont présentés.

Le premier est une étude numérique de la réflexion d'ondes de choc sous des conditions associées aux détonations. Un solveur avancé est utilisé pour résoudre les équations d'Euler. Il est démontré que la configuration de réflexion est dépendante du type de solveur, de l'implémentation du coin et de la résolution spatiale. Le type de réflexion (i.e. régulière ou irrégulière) dépend de la géométrie du coin, même loin du coin, montrant que les conditions initiales jouent un rôle important.

Ces complications sont adressées dans des simulations visqueuses impliquant des chocs résolus, en prenant pour nouvelles conditions initiales la réflexion d'un point triple. La méthode numérique est développée dans le deuxième article et la présence d'instabilités de Kelvin-Helmholtz y est étudiée. La viscosité joue un rôle important en retardant l'instabilité. Il est constaté que cette dernière ne joue pas un rôle important dans le processus d'accélération des réactions sur des échelles de temps comparables à celles de l'autoignition derrière le *Mach stem*, mais pourrait le devenir sur des échelles associées à une cellule de détonation.

La bifurcation des *Mach stem* est étudiée expérimentalement et numériquement dans le troisième article. Les réflexions de chocs expérimentales sont réalisées sur une surface de glissement libre dans des gaz ayant différents indices adiabatiques. Les bifurcations sont observées dans les expériences, et les simulations visqueuses et non-visqueuses. La viscosité retarde les bifurcations. Les simulations non-visqueuses sont utilisées pour approximer les limites des bifurcations, en fonction du nombre de Mach, de l'indice adiabatique, et de l'angle de réflexion. Un indice adiabatique maximum au-delà duquel aucune bifurcation n'est observée est trouvé. Il correspond à la limite irrégulière/régulière de la structure cellulaire des détonations. Une instabilité est observée dans les expériences à haut nombre de Mach et petit indice adiabatique.

La deuxième partie de cette thèse comprend un article. Elle traite la dynamique des détonations avec plusieurs pics de thermicité, en utilisant l'analogie de Fickett. Une analyse d'états stationnaires prédit l'existence de plusieurs états stationnaires possibles, dont uniquement le plus rapide est sans singularité. Des simulations montrent que les autres solutions développent des ondes de choc internes, qui permettent éventuellement l'établissement de détonations qui se propagent à la vitesse maximale permise par le critère de Chapman-Jouguet généralisé. Des analyses caractéristiques et de stabilité linéaire démontrent que les chocs internes sont dûs à des instabilités aux points soniques.

Acknowledgements

This thesis was made possible by the invaluable help, support, and guidance from my supervisor Dr. Matei Radulescu, my colleagues, family, and friends.

Financial support was provided by the Ontario Ministry of Training, Colleges and Universities via an Ontario Graduate Scholarship (OGS), and by the Natural Sciences and Engineering Research Council of Canada (NSERC) in the form of the Alexander Graham Bell Canadian Graduate Scholarship (CGS).

Table of Contents

List of Figures

Introduction

Detonation waves can propagate through a variety of reactive media, ranging from hydrocarbon mixtures, solid explosives, dusty environments, to nuclear and stellar media. Detonations are supersonic reaction waves, meaning they travel faster than the speed of sound in the reactive medium. They are comprised of a shock wave followed by energy release from a reaction, as illustrated in figure 1. As the shock wave passes through the reactive medium, it increases temperature, induces flows, and compresses the medium. The large compression and temperature increase makes for a rapid reaction which expands the medium. The expansion in turn drives the leading shock wave, making detonations a self-sustained process.

The speed at which a detonation travels is determined by the net energy release from the reaction available to the shock front. The minimum steady speed of an detonation is known as the Chapman-Jouguet (CJ) velocity [1]. Detonations travelling faster than the Chapman-Jouguet velocity may be sustained if the detonation is supported by a sufficiently fast piston, for example. They otherwise decay to the Chapman-Jouguet speed as expansion signals are able to reach the front. Detonations travelling at velocities below the steady speed are unsteady; these detonations may accelerate to the Chapman-Jouguet speed if the energy release is sufficiently coupled to the shock, otherwise the lead shock will decay, the heat-releasing reactions will slow exponentially and eventually uncouple from the shock front, and the detonation will be quenched. The formation of a detonation by a shock wave travelling above or below the Chapman-Jouguet velocity is known as direct initiation and will be one of the problems investigated in the second part of the thesis.

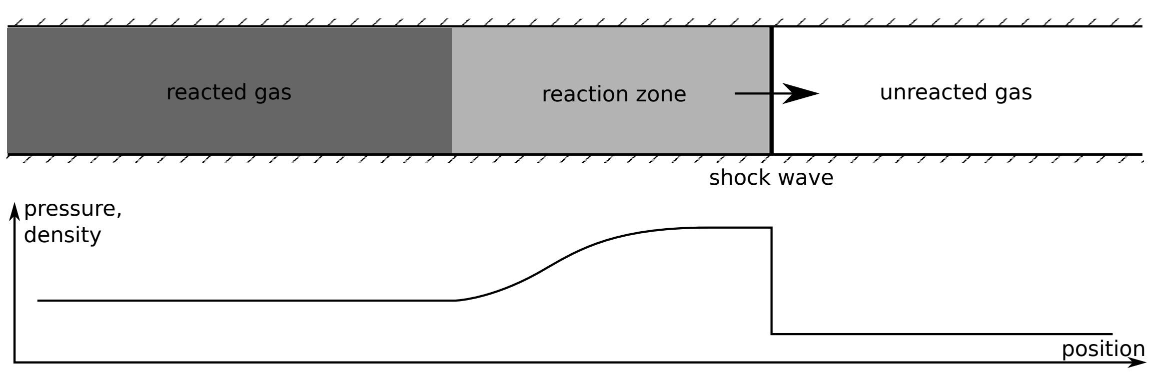

Figure 1: Illustration of a steady one-dimensional detonation, travelling from left to right, with pressure and density profile below

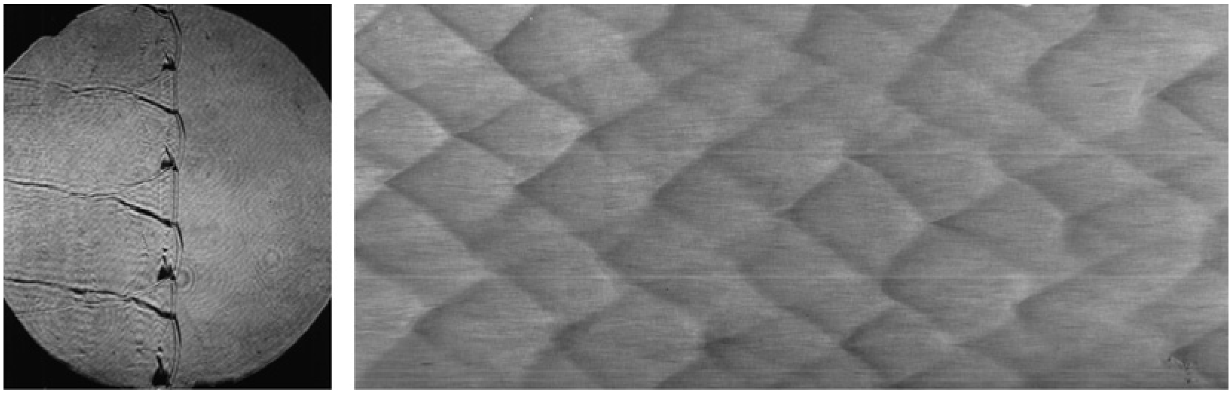

Figure 2: Schlieren photograph (left) of a detonation travelling from left to right and the corresponding traces left on a soot foil (right) [4]

Steady detonations, however, are not observed in reality. Two modes of instability are typically seen: one-dimensional pulsating instabilities and multi-dimensional cellular instabilities. It has been shown that unstable mixtures are more readily detonable and have the ability to sustain detonations when subjected to losses [2,3] exceeding their current theoretical limits. Accordingly, determining the mechanisms associated with their instability is of particular interest.

Experiments and simulations in multiple dimensions have shown the detonation front takes on a cellular structure [1], as opposed to a planar front. The so-called cellular structure is named from the fish-scale-like pattern left behind by an unstable detonation passing over a soot-covered foil, an example is shown on the right of figure 2. Cell size has been correlated with many limiting detonation criteria, such as propagation limits, initiation, and failure criteria. The cellular structure is a result of transverse shocks waves travelling along the detonation front, seen as bold oblique lines on the left of figure 2, reflecting from each other. The reflections of shock waves create hot spots, turbulence, increase reaction and energy release rates, and are believed to play an important role in detonation propagation. The first part of this thesis will focus on shock wave reflections under detonation-like conditions.

The high speed hydrodynamics and the small spatial and temporal scales of the chemical reactions involved have made experimental work challenging. Numerical simulations have proved to be a useful tool to support experiments and analysis. Simulations typically use the Euler equations, which are the Navier-Stokes equations without diffusion terms. This assumption is generally acceptable when looking at gross properties of detonations, as the high speeds (on the order of kilometres per second) of detonations overwhelm diffusive effects, and neglecting diffusion simplifies simulations. However, the Euler equations do also have drawbacks. They are complicated to treat analytically, their numerical solutions do not converge in multiple dimensions, and the diffusive effects ignored by the Euler equations may be important to damping instabilities on the small scales leading up to exothermic reactions. Reaction mechanisms further complicate the system, as realistic chemistry adds complexity to the system and requires finely tuned constants.

The study addresses these issues in two parts. The first part will study aspects of shock reflections in detonations. Reactions will be neglected in this part of the study, limiting the focus to the early stages of shock reflection in two-dimensional detonation propagation. The unsteady problem of inviscid shock reflection over a concave wedge will first be investigated. Converged numerical simulations of the Navier-Stokes equations will then be used to examine the effect of diffusion-dependent structures in the shock reflection process, followed with experiments of shock reflections over a plane of symmetry.

In the first part, section 1.1, will review the relevance of shock wave reflections to detonations. The similar problem of shock reflections from wedges will be reviewed in section 1.2 with additional detail to interesting aspects of shock reflection in sections 1.3 and 1.4, summarized in section 1.5. The parameter range for the study will be presented in section 1.6 and the numerical methods used to study shock reflections will be briefly covered in section 1.7. The first part is concluded with three papers examining aspects of shock reflections relevant to detonations.

The second part will take the opposite approach and make use of a simplified model with simple reactions to gain insight into detonation initiation in one-dimensional detonations. The simplified models allow some complexities of the Euler equations to be avoided, while retaining some aspects that are important to detonations. The asymptotic derivation of a simplified detonation model will first be shown in section 2.1. Hybrid detonations are introduced in section 2.2 and studied using Fickett's detonation analogue in section 2.3.

Contributions of this body of work to the state of the art are summarized in chapter 3.

Chapter 1

Triple shock reflections relevant to detonations

1.1 Shock reflections in detonations

Detonations are supersonic combustion waves lead by a shock wave. As the shock passes through the reactive medium, a gas in this case, it suddenly compresses and heats the medium. The gas rapidly reacts due to the increased temperature, and expands as it does so. The expansion feeds pressure waves forward which drive the lead shock. Detonations are inherently unstable and in multiple dimensions, the front adopts a well known cellular structure [1]. The front of a detonation is not planar. It is corrugated with some portions travelling faster than others. The fast parts, called Mach shocks, overtake the slower incident shocks and periodically reflect from one another.

The series of schlieren photographs (density gradients) superimposed in figure 1.1 show the front of a detonation travelling from left to right. The first frame shows that the shock front is formed from two curved shocks called Mach stems (or Mach shocks) on the top and bottom, connected by a straight vertical shock known as the incident shock wave. The kinks joining the Mach stems to the incident wave are known as triple points. The bright textured features behind (to the left of) the shocks are caused by gas expansion from reactions. Two pairs of additional features are seen protruding to the left from the triple points. The short bright lines are shocks travelling towards the centre, called the reflected (transverse) shocks, and the dark rippled features are contact surfaces. The incident shock, Mach stem, transverse shock, and contact surface are joined at the triple point and form the triple shock structure. The triple shock structures on the top half of figure 1.1 are illustrated on the left side of figure 1.2.

The pair of triple points shown in figure 1.1 travel towards the right and towards the centre. In the first two frames of figure 1.1, the pair of triple points move towards each other and upon their arrival they, and the Mach stems that follow, reflect from the plane of symmetry. The reflection forms two new triple points which travel apart, seen in the last three frames and illustrated on the right side of figure 1.2.

The trajectory of triple points in detonations can also be recorded with soot foils (smoke deposited on a metal foil) placed on walls in contact with the flow, first used by Denisov and Troshin [6]. Figure 1.3 shows a soot foil for a detonation travelling from left to right. The oblique white lines traced by the triple points outline the fish-scale-shaped detonation cells, and their intersections correspond to the collision of triple points. Triple shock structures are sketched onto figure 1.3 in yellow before and after reflections to show how the triple points travel along these white traces and reflect from axes of symmetry, like shown in figure 1.1.

The soot foil technique was a popular way to gather information concerning the detonation wave structure. Strehlow *et al.* [7,8] used soot foils to study Mach stem interactions in detonations and were able to measure the strength of transverse waves, determining that a study of wave interactions would be necessary to develop a working theory to the propagation of detonations in two or more dimensions. There has since been extensive research, both numerical and experimental, trying to determine the effects of triple shock reflection on detonation propagation [5,9,10], as it is largely agreed that shock reflections play an important role in the propagation of detonations.

The autoignition process described at the beginning of this chapter, where the high temperature of the shocked gas allows it to react quickly, becomes more complicated with triple shock structures along the front. The varying shock strength, caused by the decaying shock and triple points on the front, affects autoignition time exponentially. The strong Mach shocks increase gas temperature in excess of the incident and reflected shocks, creating a contrast in autoignition times. The presence of reflected shocks is believed to contribute to detonation propagation [2,11,12], and transverse waves can sometimes become detonations on their own right, travelling transverse to the main front [12,13].

Autoignition time differences along the detonation front can result with the burnt gas

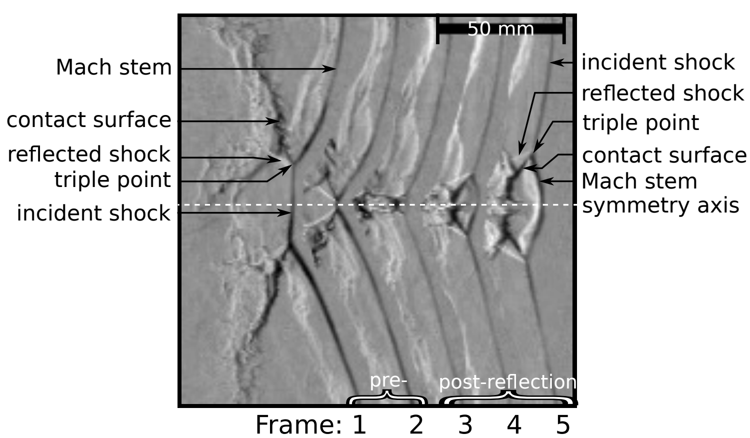

Figure 1.1: Superimposed schlieren photographs of a detonation travelling from left to right, with two triple points that reflect from each other between the second and third frames; dark features indicate expansion (left to right) and bright features show compression ($CH_4 + 2O_2$, $p_0 = 3.5$ kPa, $T_0 = 300$ K, $\Delta t = 11.53$ μs, adapted with permission from Bhattacharjee [5])

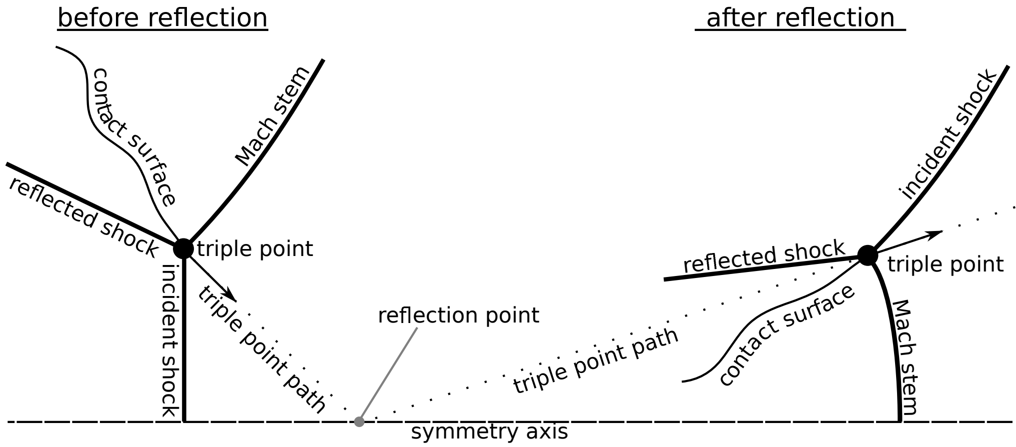

Figure 1.2: Sketch of triple point reflection from a symmetry axis surface, creating a new triple shock structure travelling away from the surface like shown in the top half of figure 1.1; arrows represent the triple point's direction of travel

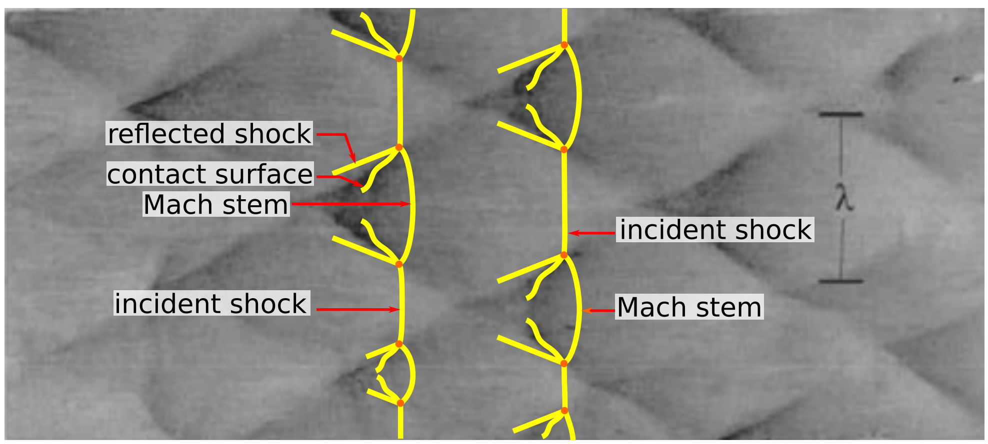

Figure 1.3: Example of a detonation soot foil showing the triple point paths as dark oblique lines [4] with triple shock configurations from the detonation front labelled and sketched in colour, before and after triple point reflections

---

along the contact surface, shocked by the Mach stem, to reside next to unburnt gas on the other side of the contact surface, shocked by the incident and reflected shocks. Mixing these hot burnt gases and their chemical radicals with unburnt gas could increase reaction rates. Mixing along the contact surface can be accelerated through Kelvin-Helmholtz and Richtmyer-Meshkov instabilities [9], the former visible in figure 1.1. In some cases, the contact surface turns and jets towards the shock front, seen in the last frame of figure 1.1 near the symmetry axis. This forward jet may be another source of mixing [11, 13–15], may cause the Mach stem to travel faster than it would otherwise, or even create new detonation cells [16, 17].

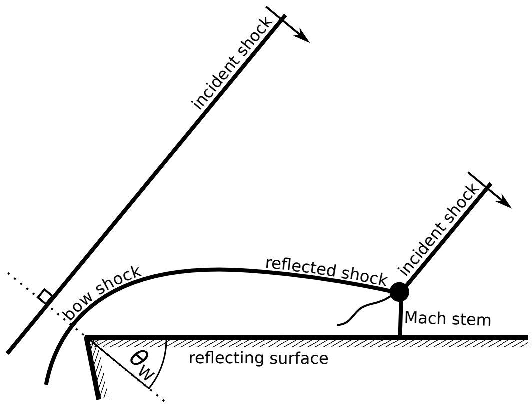

(a) Irregular reflection

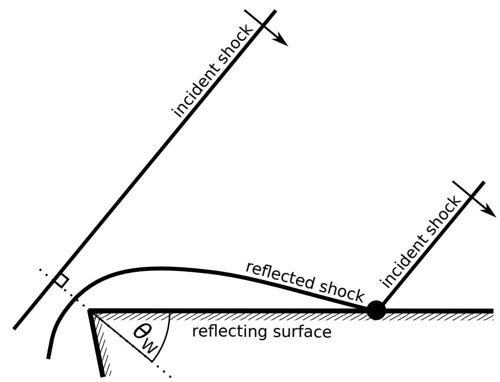

(b) Regular reflection

Figure 1.4: Sketch of a shock wave travelling towards the right, reflecting from a wedge and adopting one of two types of shock reflection; rotated by the wedge angle θ_w so that the reflecting surface is horizontal

The importance of these phenomena depend on the shock wave reflection conditions, some being more important than others in allowing detonations to propagate with large losses. Exactly how shock reflections contribute to driving detonations remains an open question and motivates this particular research into the reflection of triple shock structures. The shock reflection process from which these phenomena arise will be addressed in following chapters, with special interest paid to initially unsteady reflections, Kelvin-Helmholtz instabilities and forward jetting of the contact surface.

1.2 Review of shock reflections from wedges

While triple shock structures occur naturally in detonations, they also happen when a shock reflects from an oblique surface such as a wedge. Consider a shock wave travelling through a quiescent gas and colliding with an oblique wedge. When the supersonic flow driving the incident shock collides with the impermeable wedge (or a plane of symmetry), a shock wave is necessary to turn the flow parallel to the surface, giving rise to the shock reflection. The orientation of the problem has been rotated by the wedge angle θ_w in figure 1.4 so that the reflecting surface is horizontal, for convenience and to draw comparisons to shock reflections in detonations. There is a large body of work on shock wave reflections from wedges, and their similarities to those in detonations will be helpful in studying triple shock reflections. Reviews of the subject have been written by Hornung [18] and Ben-Dor [19].

The geometry of the reflected shock configuration is decided by three parameters: the Mach number of the incident shock, the angle of reflection, and the isentropic exponent of the gas. For lower Mach numbers, shallow wedges (larger angles between the incident shock and reflecting surface), and large isentropic exponents, an irregular reflection (Mach reflection) tends to occur (figure 1.4a) with a triple-shock structure similar to those in det-

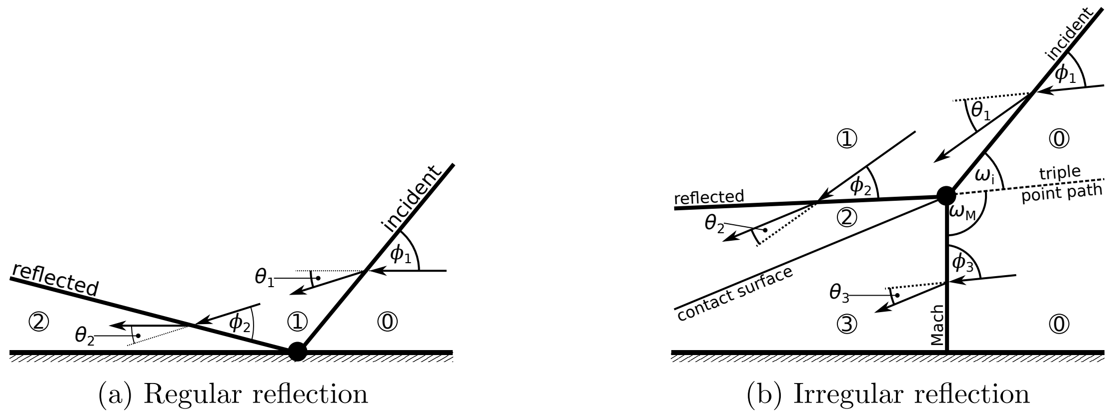

Figure 1.5: Diagrams for analysis of two common types of shock reflection; arrows denote the direction of the flow in the (a) reflection point frame of reference, and (b) triple point frame of reference; circled numbers designate the unshocked state (0), incident state (1), reflected state (2), and Mach shocked state (3)

onations. As the Mach number or wedge angle are increased, or as the isentropic exponent is decreased, the angle of the triple point trajectory above the reflecting surface decreases; in other words, the triple point approaches the wedge and the Mach stem becomes shorter. The Mach stem eventually disappears, leaving only the incident and reflected shocks in a configuration known as regular reflection (figure 1.4b).

The bases of analysing regular and irregular reflections are the two and three shock theories, first posed by von Neumann [20], and will be reviewed in the next two sections. The two shock theory of regular reflections will be covered first for its simplicity, then the more complicated three shock theory will be reviewed.

1.2.1 Two shock theory

The regular shock reflection is composed of the incident shock and a reflected shock, joined on the surface at the reflection point. The incident shock compels the quiescent gas onto the reflecting surface, and the reflected shock redirects the flow parallel to the surface. The regular reflection is analysed using two shock theory which assumes the flow is inviscid and both shocks are straight.

The frame of reference is taken about the reflection point, shown in figure 1.5a, making the flow pseudosteady. The speed of the incident shock S_i is typically known along with the wedge angle $\theta_\mathrm{w} = \pi/2 - \phi_1$, and quiescent gas state (subscripted with 0). The reflection point speed along the surface is calculated from the incident shock speed and angle it makes with the reflecting surface, thus the unshocked flow speed relative to the reflection point is

$$u_0 = S_\mathrm{i} / \sin(\phi_1). \tag{1.1}$$

The incident shock is oblique to the unshocked flow in this frame, and the state behind it can be calculated from the unshocked state using oblique shock relations [21]. The components normal and tangential to the incident shock are

$$u_{0\mathrm{n_i}} = u_0 \sin(\phi_1) \qquad \text{and} \qquad u_{0\mathrm{t_i}} = u_0 \cos(\phi_1) \tag{1.2}$$

for a shock angle ϕ_1 between the incident shock and incoming flow. For a perfect gas [21], the pressure jump from the unshocked state 0 to the incident shock state 1 is

$$\frac{p_1}{p_0} = \frac{2\gamma M_{0\mathrm{n}}^2 - (\gamma - 1)}{\gamma + 1}, \tag{1.3}$$

and the density jump is

$$\frac{\rho_1}{\rho_0} = \frac{(\gamma + 1) M_{0\mathrm{n}}^2}{(\gamma - 1) M_{0\mathrm{n}}^2 + 2}, \tag{1.4}$$

with γ as the isentropic exponent and $M_{0\mathrm{n}} = u_{0\mathrm{n}}/c_0$ as the shock Mach number (flow Mach number into and perpendicular to the incident shock) with unshocked sound speed c_0. The flow velocity normal to the incident shock is found from the conservation of mass

$$u_{1\mathrm{n_i}} = \frac{\rho_0}{\rho_1} u_{0\mathrm{n_i}} \tag{1.5}$$

while the tangential component remains unchanged

$$u_{1\mathrm{t_i}} = u_{0\mathrm{t_i}}, \tag{1.6}$$

allowing the flow deflection angle to be calculated

$$\theta_1 = \phi_1 - \arctan\left(\frac{u_{1\mathrm{n_i}}}{u_{1\mathrm{t_i}}}\right). \tag{1.7}$$

The incident state (1) is now completely known, leaving only the reflected state (2) to be calculated.

The reflected shock acts to deflect the flow parallel to the impermeable reflecting surface, necessitating that the boundary condition

$$\theta_2 = \theta_1 \tag{1.8}$$

be fulfilled, but the orientation of the reflected shock to the flow must be known to calculate the reflected state (2) and close the problem. The reflected shock angle ϕ_2 in a perfect gas can be found as a function of the deflection angle θ_2, imposed by the boundary condition equation 1.8, through the cubic equation [21]

$$A \sin^6(\phi_2) + B \sin^4(\phi_2) + C \sin^2(\phi_2) + D = 0 \tag{1.9}$$

with coefficients

$$A = 1, \qquad B = -\frac{M_1^2 + 2}{M_1^2} - \gamma \sin^2(\theta_2),$$

$$C = \frac{2M_1^2 + 1}{M_1^4} + \left(\frac{(\gamma + 1)^2}{4} + \frac{\gamma - 1}{M_1^2}\right) \sin^2(\theta_2), \quad \text{and} \quad D = -\frac{\cos^2(\theta_2)}{M_1^4}$$

where $M_1 = u_1/c_1$ is the incident shock flow Mach number with incident flow ($u_1 = \sqrt{u_{1n_i}^2 + u_{1t_i}^2}$) and sound ($c_1 = \sqrt{\gamma p_1/\rho_1}$) speeds. Of the three roots, the smallest root is unphysical (requires a decrease in entropy), the middle root is the weak shock solution, and the largest root is the strong shock solution. The strong shock solution is invalidated by the sonic criterion later described in section 1.2.3. In imperfect gases, the flow speed normal and tangent to the reflected shock

$$u_{1n_r} = u_1 \sin(\phi_2) \qquad \text{and} \qquad u_{1t_r} = u_1 \cos(\phi_2),$$

with unknown reflected shock angle ϕ_2, are used to find the reflected shock state (subscript 2) with flow speed

$$u_{2n_r} = \frac{\rho_1}{\rho_2} u_{1n_r} \qquad \text{and} \qquad u_{2t_r} = u_{1t_r},$$

and deflection angle

$$\theta_2 = \phi_2 - \arctan\left(\frac{u_{2n_r}}{u_{2t_r}}\right).$$

Numerical root finding can be used to find the values of ϕ_2 (and the corresponding reflected shock state) which satisfy the boundary condition equation 1.8. The perfect gas solution serves as a good initial guess.

1.2.2 Three shock theory

There is a point where the maximum turning angle of the reflected shock is reached, rendering it unable to divert flow parallel to the surface. A regular reflection becomes impossible and an irregular reflection is formed with a third shock, the Mach stem, between the reflected shock and the surface.

The three shock theory [20] used to describe irregular reflection is similar to the two shock theory of regular reflections. A pseudo-steady frame of reference attached to the triple point is used, making the flow self-similar as largely observed in experiments. This means distances scale linearly with time. Four straight discontinuities are considered: the incident, reflected (transverse), and Mach shocks, and a contact surface (or contact discontinuity, slip line) joined at the triple point some distance above the surface, illustrated in figure 1.5b.

The unshocked flow, in the triple point's frame of reference, crosses the oblique incident shock and is then redirected by the reflected shock, like in two shock theory, but the flow in the reflected shock region (2) is not parallel to the reflecting surface. Meanwhile, the unshocked flow is also being processed by the Mach stem and ends up next to the reflected shock state. A contact surface appears in order to separate the flow in state (2) shocked by the incident and reflected shocks from the flow in state (3) shocked by only the Mach stem. Two boundary conditions exist across the contact surface: flow on either side must be parallel

$$\theta_3 = \theta_1 \pm \theta_2 \tag{1.10}$$

and pressure across the contact surface is equal

$$p_3 = p_2 \tag{1.11}$$

otherwise it would accelerate. Requiring the unshocked gas pressure to increase in one jump across the Mach stem versus two steps by the incident and reflected shocks means the Mach shock is strongest shock. The entropy and temperature in the Mach shock state is therefore higher than in the reflected shock state, and the stagnation pressure and kinetic energy is lesser.

Typically the unshocked state (0) is known, the speed of the incident shock S_i (or as will be discussed later, as is the speed of the Mach stem S_M) in the lab frame of reference, and either the wedge angle or the angle between the incident and Mach shocks. However unlike in two shock theory, the incident shock angle in the triple point frame of reference is not easily found because the angle of the triple point path is unknown. The triple point path angle is often described as the angle χ between the reflecting surface and triple point path, but can also be written as the angle $\omega_\mathrm{i} = \phi_1$ between the triple point path and incident shock or Mach stem ($\omega_\mathrm{M} = \pi - \phi_3$). Additionally, a relation between the incident and Mach shocks is needed to account for the additional shock angle. This is often done by assuming the Mach stem at the triple point is perpendicular to the wedge (the Cabannes assumption [22])

$$\phi_1 = \pi/2 - \chi - \theta_\mathrm{w} \qquad \text{and} \qquad \phi_3 = \pi/2 - \chi$$

although it is not necessarily true, or by choosing the angle $\omega_0 = \omega_\mathrm{i} + \omega_\mathrm{M}$ between the incident and Mach shocks such that

$$\phi_1 = \omega_\mathrm{i} \qquad \text{and} \qquad \phi_3 = \pi - \omega_\mathrm{M}.$$

In either case the angle between the incident and Mach shocks can be found as a function of the unknown triple point path angle, represented by χ, ω_i or ω_M.

Assuming a value for the triple point path angle gives the incident and Mach shock angles ϕ_1 and ϕ_3, allowing the unshocked flow velocity relative to the triple point

$$u_0 = \frac{S_\mathrm{i}}{\sin(\phi_1)} \qquad \text{or} \qquad u_0 = \frac{S_\mathrm{M}}{\sin(\phi_3)}$$

to be calculated, depending whether the incident or Mach shock speed is known. The incident and Mach shock states (1) and (3) can be calculated like in the previous section, using the appropriate unshocked normal and tangential flow components (equation 1.2) to get the shocked pressures and densities (equations 1.3 and 1.4 for perfect gases), shocked flow velocities (equations 1.5 and 1.6), and deflection angles (equation 1.7).

Like in two shock theory, the reflected state remains to be defined and the reflected shock angle ϕ_2 is unknown. The reflected shock angle is found by satisfying one of the contact surface conditions (equation 1.10 or 1.11) instead of the impermeable wedge condition. For a perfect gas, the pressure jump equation 1.3 with $M_{1\mathrm{n_r}} = M_1 \sin(\phi_2)$ can be inverted

$$\phi_2 = \sin^{-1}\left(\pm\sqrt{\frac{(\gamma+1)\frac{p_2}{p_1} + (\gamma-1)}{2\gamma M_1^2}}\right) \tag{1.12}$$

with appropriate attention to subscripts, and solved for the reflected shock angle once the pressure condition 1.11 is substituted. The negative root is invalid, and the obtuse solution (unrestricted solution of arcsin in the second quadrant, $\phi_2 > \pi/2$) results in a von Neumann reflection. An interested reader may look to the literature referenced in section 1.2.3 for further information; only the $\phi_2 < \pi/2$ case, as drawn in figure 1.2 will be considered. At this point, the triple point path remains unknown but can be found by satisfying the remaining contact surface condition. This means finding two roots simultaneously in an imperfect gas.

1.2.3 Selection of a reflection configuration

Transition between regular and irregular reflection

The two and three shock theories discussed in the previous sections are used to calculate flow near the reflection and triple points during shock reflection, so predicting whether a regular or irregular reflection will occur is the next obvious step. Delimiting the regular to irregular transition has been the object of much interest, especially since there is a region of overlap where both two and three shock theories have valid solutions for a given set of parameters. Three major criteria have been proposed to describe the transition from regular to irregular reflection: the mechanical equilibrium, detachment, and sonic criteria, compared in Ben-Dor's monograph [19].

The mechanical equilibrium criterion [20, 23, 24] states that the transition from regular to irregular reflection occurs when pressure in the reflected state of a regular reflection is equal to pressure in the reflected and Mach states of an irregular reflection under the same parameters. This criteria arose from the study of steady shock reflection (*e.g.* at the intake of a supersonic engine), where upon continuously changing the wedge angle, transition to and from regular reflection occurred without the sudden appearance of a compression or expansion wave that would have been present if pressure at the reflecting surface between the two types of reflections differed. Henderson and Lozzi [23, 24] showed there was good agreement between this criterion and experimental transition in steady flows, barring weak shocks, but evidence for this transition boundary in pseudosteady reflections was weak, with regular reflections persisting below the transition limen. Furthermore, compression and rarefaction waves accompanied transition in unsteady shock reflections from curved surfaces. It has since been well established that the mechanical equilibrium criterion is not valid for pseudosteady reflections.

Oblique shocks, such as the reflected shock, have a maximum flow deflection angle beyond which an oblique shock is insufficient to turn the flow. This maximum deflection angle is obvious in plots of the shock wave angle versus flow deflection angle, a common chart in text books covering oblique shocks [21]. In two shock theory, the reflected shock is responsible for redirecting the incident flow parallel to the reflecting surface. When the turning angle set by the incident shock exceeds the maximum flow deflection angle, the reflected shock must detach from the surface and no two shock solution exists. This point defines the detachment criterion which states that regular reflections will exist until the maximum turning angle of the reflected shock is reached. The detachment criterion lies very close to the transition point found in experiments, however it slightly underpredicted the wedge angle at which irregular reflections transition to regular reflection.

Very close to the maximum turning angle (in parameter space) of an oblique shock lies the sonic limit, also commonly plotted on the aforementioned oblique shock charts. The sonic limit separates regions where flow behind an oblique shock is supersonic and subsonic, in the shock's frame of reference. Hornung *et al.* [18, 25, 26] proposed that a regular reflection will occur whenever the flow behind the reflected shock is supersonic, and an irregular reflection will occur when it is subsonic. This is known as the sonic (or information) criterion and can be justified by arguing that when the reflected flow is subsonic, signals from the wedge tip reach the reflection point, communicating and forcing a length scale on the reflection point, giving the Mach stem height. When the reflected flow becomes supersonic, information cannot be transmitted to the reflection point, so it remains free of length scale and a Mach stem cannot exist. The transition predicted by the detachment and sonic criteria are generally very close despite their differences in reasoning, owing to the slim difference between the maximum turning angle and sonic limit in oblique shocks. Although the sonic criterion is generally accepted as valid [19], other real gas phenomena such as relaxation [27, 28], reactions, and diffusion [29–31] make the detachment and sonic criteria difficult to test in practice. Efforts continue to try and determine the exact transition point [32, 33].

Subtypes of irregular reflection

Shock reflections configurations can be subdivided beyond regular and irregular reflections. The latter can be split into many subcategories. Much ongoing work has been put into determining the numerous sub-types of irregular reflection and the conditions under which they exist. Recent classifications have been written by Ben-Dor [19], Vasilev *et al.* [34], and Semenov *et al.* [35–37]. Again the type of shock reflection depends on three parameters: the isentropic exponent of the gas, the reflection angle, and Mach number of the incident shock. Low wedge angle and Mach number reflections will not be considered in this thesis because these parameters are not typical of shock reflections in detonations. Instead, the single, transitional, and double Mach reflections (and its sub-classifications used by some) are of most interest.

The single Mach reflection, simply composed of a triple point with a reflected shock that curves back to the wedge tip, is illustrated in figure 1.6a. The shape of the reflected shock comes from an interaction between the flow near the triple point with flow being deflected by an oblique or bow shock at the wedge tip, as is the case in all reflection types. The angle and curvature of the shocks may vary.

The double Mach reflection is similar to the single Mach reflection, but with a modification to the reflected (or transverse) shock. There is a second triple point along the transverse shock, as illustrated in figure 1.6c. Li and Ben-Dor [38] assumed that the flow behind the transverse shock (in region (2) of figure 1.5b) is supersonic with respect to the second triple point, requiring a new shock between it and the contact surface of the first

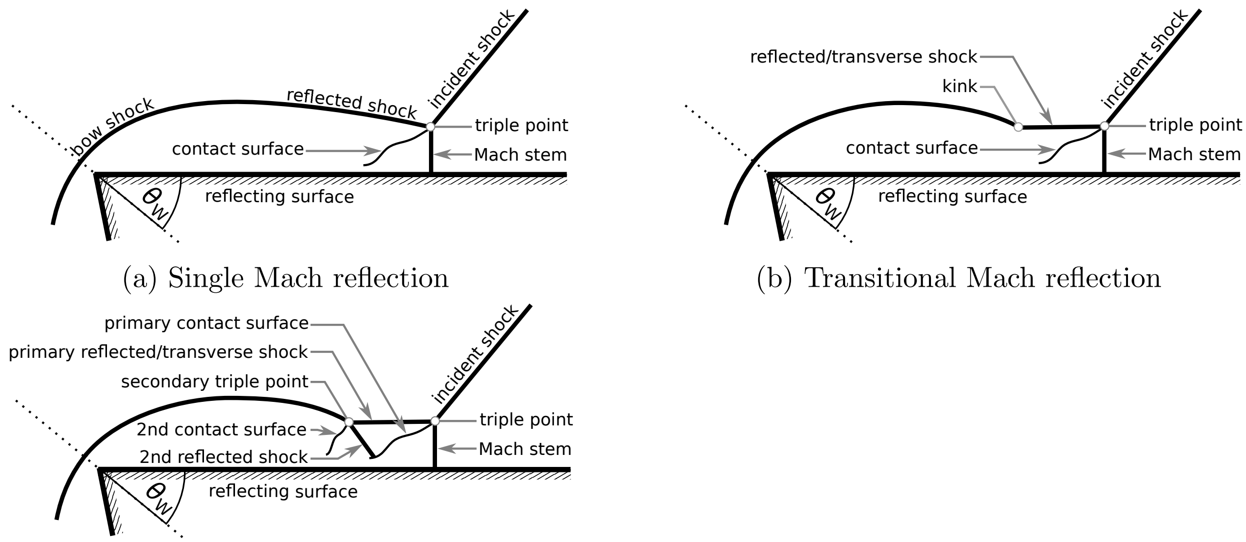

(a) Single Mach reflection

(b) Transitional Mach reflection

(c) Double Mach reflection

Figure 1.6: Illustrations of Mach reflections of interest; the bow shock may be replaced by an oblique shock attached to the wedge when appropriate

triple point. This shock is sometimes (misleadingly) called the second Mach stem [39], but will herein be referred to as the secondary reflected shock. The transverse shock between the two triple points is straight as a result of being shielded from corner signals by the new shock. The two cases of double Mach reflections they considered either had the secondary reflected shock perpendicular to the primary contact surface, or had the secondary reflected shock intersect the contact surface very close to the wall. These assumptions fix the angle of the secondary reflected shock (instead of fixing the Mach stem's angle) and allow the secondary triple point's trajectory to be calculated with three shock theory. A contact surface is also formed at the new triple point, however it is sometimes faint.

The transitional Mach reflection illustrated in figure 1.6b is a mixture of the single and double Mach reflection. A kink replaces the secondary triple point and a vanishingly weak shock is formed between the kink and contact surface. Flow behind the transverse shock is sonic with respect to the kink [38] so signals from the wedge tip cannot bend the straight portion of the transverse shock.

Single Mach reflections occur at smaller wedge angles and Mach numbers, and larger isentropic exponents than transitional and double Mach reflections, the latter presenting closest to the regular reflection limit. Ben-Dor [19] has a thorough review of analyses and transition criteria for these types of shock reflections.

Additional features of interest are found in Mach reflections, illustrated in figure 1.7. The contact surface can be smooth but sometimes takes on a wavy shape as Kelvin-Helmholtz instabilities grow in the shear layer, illustrated in figure 1.7a. Upon reaching the reflecting surface, flow on either side of the contact surface must turn to become parallel to the wedge. Under circumstances where the flow deflection pressure around the wedge tip is smaller than the reflected shock pressure, generally at low wedge angles and Mach

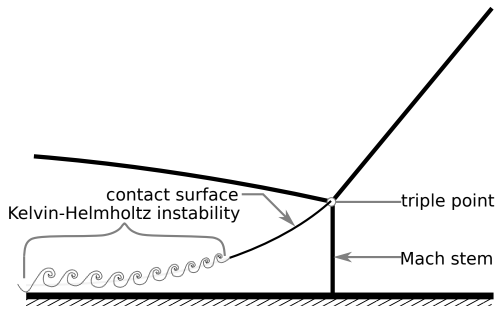

(a) Without forward jetting; Kelvin-Helmholtz instabilities may occur on the contact surface downstream of an undisturbed region

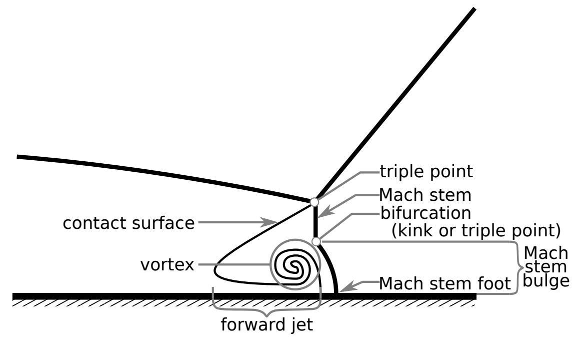

(b) With a forward jet; Kelvin-Helmholtz instability (not shown), vortex, and Mach stem bulging may occur independently of each other; Mach stem bifurcation may occur with bulging

Figure 1.7: Illustrations of a single Mach reflection near the triple point with additional features of interest (not exclusive to single Mach reflections)

numbers, the contact surface curves towards the wedge tip and away from the triple point (figure 1.7a). In other cases when the flow deflection pressure is high, the contact surface can curl along the reflecting surface towards the Mach stem, creating a jet along the wall (figure 1.7b). This forward jet can create a vortex in the region bounded by the wall, contact surface and Mach stem. The Mach stem may be straight and perpendicular to the wedge, but is sometimes slightly concave or convex. In some cases, the Mach stem bulges out near the wall to the point of kinking the Mach stem between the wall and original triple point. These different cases are classified as their own subtypes by some [35–37].

The contact surface and forward jet have been partially described in literature, with their existence or magnitude only partially mapped based on the three parameters important for determining the shock reflection configuration. There are indications these phenomena may play a role in near-limit detonation propagation and will be subjects of study in this thesis. The following two sections will cover them in more detail.

1.3 Contact surface

The contact surface (also called the contact discontinuity, shear layer, slip line, slip stream, or vortex sheet) separates the gas shocked by the Mach stem from gas shocked by the incident and reflected shocks. The pressures on either side are equal and the flow is parallel but of different speeds, densities, and temperature. The tangential velocity difference creates a shear flow from which a boundary layer can grow. Zaslavskii and Safaraov [40] suggested that the finite thickness of the slip line due to viscous boundary layer growth might change the reflection configuration (*i.e* shock angles and strengths) as flows on either side of the contact surface would no longer be parallel. Courant and Friedrichs [41] suggested using boundary layer development theory along the slip line to calculate its thickness. This was done by Ben-Dor [42] who modelled the effect of viscosity along the slip line as mass boundary layer displacement and was able to predict the experimental irregular-to-regular reflection transition more accurately than using inviscid three shock theory. Thickening of the slip line is important to the configuration of the three shock problem and detonations since changes in angles between shocks change their strengths, the jumps in temperature, and therefore reaction rates in the gas.

Turbulence can also cause the slip line to thicken; the tangential velocity difference between the two fluids can give rise to the Kelvin-Helmholtz instability [43, 44], like waves seen over a windswept lake and as illustrated in figure 1.7a. The growth of these instabilities was found by Rikanati *et al.* [45, 46] to account for the majority of the slip stream thickening when the Reynolds number exceeded a critical value, similar to that of other mixing phenomena. They attributed disagreements in slip line thickness below the critical value to viscous effects which were not accounted for in their model. When Rubidge and Skews [47,48] compared their simulations and experiments to the Rikanati's *et al.* [45], they found only half the expected spread. Recent larger scale experiments by Hall *et al.* [49] found the same discrepancy. They suggested the difference may be due to the measurement techniques (schlieren imagery versus interferometry) as they found little difference between their inviscid and viscous simulations.

In detonations, this instability is believed to increase turbulence and mixing along the contact surface [9]. As gas on the Mach stem side of the contact surface reacts [50], hot reaction radicals [1] may mix with unreacted gas across the slip line through the Kelvin-Helmholtz instabilities, increasing reaction rates [5, 14]. Alternatively, premature mixing could homogenize temperature and increase reaction times. A linear stability analysis and numerical study of the shear layer by Massa *et al.* [51] found that the Kelvin-Helmholtz instabilities could be attenuated by reactions and that diffusion was an important factor to the onset of reactions. This suggests instability growth could be delayed in reactive flows, if ignition occurs before the critical Reynolds number. It is therefore of interest to know when Kelvin-Helmholtz instabilities arise in detonations, before or after reactions.

The effect of viscosity on the contact surface appears to be important. Boundary layer thickening, through diffusion or turbulence, may affect the triple shock structure and strengths. The growth rate of Kelvin-Helmholtz instabilities, which thicken the contact surface and increase mixing, appears to be governed by the Reynolds number, where viscosity plays a stabilizing role. The effect of viscosity and Kelvin-Helmholtz instabilities in the contact surface can also be carried into the forward jet.

1.4 Forward jet

Under certain circumstances, the contact surface will curve towards the Mach stem, as sketched in figure 1.7b to form a forward jet (also called a wall jet, due to its proximity to the wedge wall). In some cases, a sufficiently strong forward jet can impinge on the Mach stem, causing it to bulge forward in the vicinity of the reflecting surface. The bulging (or toeing-out) can be so strong as to bifurcate the Mach stem with the creation of a kink or new triple point between the reflecting surface and original triple point.

The forward jet began receiving attention when advances in numerical and computational methods (*ca.* 1985) allowed Glaz *et al.* [52,53] to compare inviscid numerical simulations to experimental shock reflections. Their simulations showed forward jetting that was slightly more pronounced than in experiments. The discrepancy was attributed to viscous effects, believed to be important in the vortex roll-up. Their numerical simulations were improved by Colella and Glaz [54] with the addition of adaptive mesh refinement. They found that the extent of the Mach stem bugling and size of the jet vortex were exacerbated by decreasing the isentropic exponent, supported by many experimental and numerical studies [9, 10, 16, 55] since. The forward jet also increases in strength with Mach number and wedge angle [16,17,52–54] reaching a maximum shy of the regular reflection boundary, where it once again decreases.

A few attempts have been made to predict this jetting phenomenon analytically. Hornung [18] explained that the flow along the contact surface must eventually be redirected parallel to the reflecting surface. This causes stagnation of flow normal to the reflecting surface which could drive the forward jet, should the stagnation pressure be sufficient, but he postulated that viscosity would decrease the effect of the forward jet on the Mach stem. This idea was pursued by Li and Ben-Dor [56] to determine the conditions which would lead to the convex bulging of the Mach stem in double Mach reflection, under inviscid conditions. They postulated that the Mach stem would bulge if it was slower than the jet and further expanded their solution to determine the change to triple shock geometry caused by the bulging. Their theory was compared to experiments by Ando [39] but they noted more experiments were necessary.

Mach [17] followed an approach similar to Li and Ben-Dor [56] for single Mach reflections. Forward jetting was found to begin when pressure from flow deflection on the wedge exceeded the pressure behind the Mach stem from the shock reflection process (three shock theory). He then assumed Mach stem bifurcation would occur when the jet could catch up to the Mach stem, calculated by comparing the velocity across the contact surface to the flow velocity behind the Mach stem. This predicted Mach stem bifurcation at wedge angles below what he found with inviscid numerical simulations, which he attributed to vortex formation behind the Mach stem.

An inviscid analysis by Henderson, Vasilev, *et al.* [57] found that the size of the jet vortex depended on the angle of the Mach stem at the triple point (*i.e.* the reflection geometry). Their analysis depended on simulation results and provided a necessary but insufficient criterion for jetting. The simulations indicated jetting was not a function of reflection type, presenting in single, transitional and double Mach reflections. They found that jetting decreased in the double Mach reflection regime near transition to regular reflection, which Mach [17] would later credit to the secondary reflected shock becoming oblique near the wall. This decrease will be shown in Fig. 7 of the paper presented in section 1.8. The Navier-Stokes simulations in their follow-up study [58] showed oscillations in the forward jet with increasing Reynolds number with a no-slip wedge. The moving and self-similar grids used in their study allowed for large Reynolds numbers to be achieved at the expense of a deresolved grid. When Shi *et al.* [59] recently studied jetting near a no-slip wedge, they found Mach stem deformation was "insignificant" at small scales.

The forward jet is believed to play an important role in detonations by feeding combustion radicals from the rear into unreacted gas behind the Mach stem [13]. It can sometimes roll up into a large vortex, potentially accelerating mixing and reaction rates [5, 9, 10]. A strong jet and vortex have been correlated with bulging of the Mach stem which, in inviscid simulations, can become so extreme that a kink or triple point formed along the Mach stem, bifurcating it. Mach and Radulescu [16, 17] proposed this may be a possible mechanism for the creation of new detonation cells seen in some soot foils.

Most analyses of the forward jet have been performed using inviscid assumptions, and proper consideration of viscosity is still lacking. Two studies with viscosity [58,59] included a no-slip wall which is applicable to shock reflection from wedges, but not detonations. Inviscid numerical simulations appear to over predict the strength of the wall jet and its impact on the Mach stem in comparison to experiments, which has frustrated attempts to study and map the extents of forward jetting and Mach stem bifurcation. Viscous effects are likely to be important as they affect the velocity across the contact surface, the jet and vortex, implying the Reynolds number may be the fourth parameter important to shock reflection, along with Mach number, reflection angle, and isentropic exponent.

1.5 Summary

Triple shock structures composed of three shocks and a contact surface meeting at a point are found along detonation fronts and from shock reflection off oblique surfaces. They play an important role in detonation propagation, especially in near-limit cases, as some of their features are believed to increase reaction rates. Contact surfaces can become unstable and may increase turbulence and mixing. Radicals from the reacting gas on one side of the contact surface may mix with unreacted gas across the slip line through the Kelvin-Helmholtz instabilities, increasing reaction rates. The contact surface can be turned into a forward-travelling jet and vortex near the reflection surface. This forward jet and vortex may accelerate reactions in a similar way, and possibly lead to the creation of additional detonation cells. Viscosity is important to the slip line, instabilities, forward jet and vortex but has been seldom considered in previous studies.

These triple shock structures are difficult to study in detonations because they are stochastic, unsteady, and act on scales that make observation difficult. Shock reflections and triple point reflections will be studied in this thesis in order to gain insight on the stability of the contact surface, the appearance and strength of the forward jet and vortex, and how these effects may impact detonations. Making problems worse, often-used numerical simulations of the inviscid Euler equations do not converge and produce phenomena not seen in experiments.

In an attempt to address the importance of viscous triple shock reflections on detonation waves, this study will escalate from inviscid simulations of shock reflection to viscous simulations of triple shock reflection, and will conclude with new experiments of shock reflection. The next three sections will define the parameter range under which the studies will be performed, for shock reflections under detonation-like conditions, and briefly look into the numerical methods used for simulations.

The three papers will then be presented on the shock reflections and their relevance to detonation waves. The first part, presented in section 1.8, will be a numerical study of inviscid shock reflections from a ramp. It will address the importance of the initial shock reflection on longer length scales.

In the second part, presented in section 1.9, viscosity will be added to the numerical simulations in order to gauge the importance of Kelvin-Helmholtz instabilities on detonation propagation. The new simulation of triple shock reflection will replace the classic problem of shock reflection from a wedge.

Finally, the study of the relevance of shock reflections in detonations will end in section 1.10 where experiments of shock reflection from a new symmetric geometry will be performed. The free-slip condition provided by the symmetry of the problem will allow forward jetting to be assessed experimentally under detonation-like conditions. The experiments will also be compared to small scale simulations.

1.6 Parameter range

Triple shock structures depend on three parameters, the incident shock Mach number, the reflection angle (*e.g.* angle between the incident and Mach shocks, or wedge), and the isentropic exponent, and two more once viscosity and heat diffusion are considered, the Reynolds and Prandtl numbers. The parameter range is selected based on mixtures of stoichiometric hydrogen-, methane-, propane-, and ethyne-oxygen mixtures with nil to atmospheric nitrogen dilution.

To focus on detonations, the incident shock Mach number will match the detonation speed near the end of a detonation cell, where it can drop from 90% [51] to $> 70\%$ [1] of the steady detonation velocity. Similarly, the triple point path angle, immediately before reflection, tends to be $\sim 35° \pm 5°$ [7,60], measured between the triple point path and normal to the incident shock, which translates to a wedge angle of $\theta_\mathrm{w} \approx 30°$.

A uniform isentropic exponent will be assumed, despite being a function of both composition and temperature. The isentropic exponent has been calculated, using the chemical kinetics software Cantera [61], to vary from $\gamma > 1.0$ to ~ 1.4 over the temperature range expected in the triple shock region for the mixtures of interest, with differences between mixtures being more important than temperature. Chemistry will remain frozen in all cases, limiting the validity of simulations to early times but significantly reducing computational cost and complexity.

The next parameter that must be set is the Reynolds number. Rikinati *et al.* found Kelvin-Helmholtz instabilities become important at Reynolds numbers exceeding 2×10^4 [45,46], defined by the Mach stem height, the shear velocity and average kinematic viscosity across the contact surface. This critical Reynolds number allows the time required for Kelvin-Helmholtz instabilities to become important to be calculated and compared to other important time scales, such as the autoignition times on either side of the contact surface. Viscosity and heat conduction will depend on temperature by following a power law

$$\mu = \frac{\mu_{\text{ref}}}{\sqrt{T_{\text{ref}}}}\sqrt{T} \qquad \text{and} \qquad k = \frac{k_{\text{ref}}}{\sqrt{T_{\text{ref}}}}\sqrt{T},$$

a simplified version of Sutherland's viscosity law [62]. In inviscid simulations (Re $\rightarrow \infty$) viscous terms will be ignored.

The Prandtl numbers under the expected temperatures ($\sim$ 293 K) and pressures (atmospheric to $\sim$ 1 kPa) were calculated using Cantera [61] to range between 0.7 and 0.85 for the hydrocarbon mixtures, and 0.43 to 0.5 for the hydrogen-oxygen mixtures. A constant value of 0.75 will be used, valid for many gases. Some cases ignoring heat conduction (Pr $\rightarrow \infty$) were tried and resulted in heating along the contact surface [63].

1.7 Numerical methods

Difficulty exists in experimentally probing the triple shock structure of detonations due to their small characteristic sizes (on the order of millimetres) and their high velocity (on the order of kilometres per second). Popular measurement techniques include optical methods, point pressure measurements, and soot-foil records. These methods are unfortunately not yet able to resolve what happens in the vicinity of the triple point on the scales important to detonations. Numerical simulations can be a useful tool to overcome these obstacles but require their own special considerations if the flow is to be replicated with fidelity.

This section will briefly cover the numerical methods considered for the study. The AMRITA computational package developed by Quirk [64] is used in section 1.8, and the `mg` computational package developed by Falle [65] is used in sections 1.9 and 1.10. Details can be found in the individual papers.

1.7.1 Failure of inviscid simulations

The vast majority of detonation simulations have solved the Euler equations (inviscid Navier-Stokes) or under-resolved Navier-Stokes equations due to the large computational cost of properly accounting for viscosity. The inviscid assumption made by the Euler equations is generally acceptable when looking at gross properties of detonations, since the high speed (on the order of kilometres per second) of the detonation overwhelms diffusive effects. However, they do not converge in multiple dimensions, and do not account for the role of diffusive effects that may be important at small Reynolds numbers, on the small time scales leading up to exothermic reactions.

The lack of convergence seen in Mach's [17] resolution study serves to illustrate the problem of neglecting viscosity when simulating triple shock problems. High order numerical simulations [66] suffer from the same problems - the development of complex non-physical structures along slip lines. As accuracy increases and the solution tries to converge for the Euler equations, the Reynolds number tends to infinity, impacting the Kelvin-Helmholtz instabilities whose growth rates depend on Reynolds' number. The manifestation of these problems varies with numerical schemes and grid layouts, which artificially introduce diffusion differently, as seen in other self similar problems [67].

The diffraction of a shock over a rectangular step is a self-similar problem where the effects of the Euler, Navier-Stokes, and k-ϵ turbulence models were studied by Sun and Takayama [68]. They found that Navier-Stokes simulations showed some features which did not appear with the Euler model. Small vortices, absent in experiments, were seen in Euler and less so in Navier-Stokes simulations but disappeared with the use of the k-ϵ turbulence model, further highlighting that ignoring viscosity can create non-physical flows and obscure other features.

For invicid simulations of detonations and shock reflections, Kelvin-Helmholtz instabilities along the slip line become non-physical as the resolution is increased, to the point where they no longer resemble experiments. The extraneous vortices produced by the instability are carried into the wall jet and vortex. Many inviscid numerical studies have shown severe forward jetting leading to vortex roll up and Mach stem bulging or bifurcation [17, 69]. In some cases the slip line vortices can become so prolific that they appear to hamper the wall jet, compared to lower resolution simulations. Low resolutions and dissipative schemes create numerical viscosity which affect the physics of the problem. The forward jetting and vortex, however, have been more tame in experiments while Mach stem bifurcation has seldom [5, 9, 36] been captured.

Studies of viscously-resolved shock reflection are lacking from literature and inviscid simulations have failed to reproduce experiments in the aforementioned contexts. This causes a problem in understanding the contact surface, Kelvin-Helmholtz instabilities, and wall jetting and how they may affect detonation propagation. The following chapter will address the numerical methods that have been used to study shock reflection.

1.7.2 Equations

The equations to be solved numerically are the compressible Navier-Stokes equations in two dimensions which can be written as

$$\begin{aligned} \frac{\partial \rho}{\partial t} + \vec{\nabla}\cdot(\rho\vec{u}) &= 0 \\ \frac{\partial(\rho\vec{u})}{\partial t} + \vec{\nabla}\cdot(\rho\vec{u}\vec{u}) + \vec{\nabla}p - \vec{\nabla}\cdot\vec{\vec{\tau}} &= 0 \\ \frac{\partial(\rho E)}{\partial t} + \vec{\nabla}\cdot\left((\rho E + p)\vec{u} - \vec{u}\cdot\vec{\vec{\tau}} + \vec{q}\right) &= 0 \end{aligned} \tag{1.13}$$

for pressure p, density ρ, velocity u, time t, total energy

$$E = \frac{p}{\rho(\gamma-1)} + \frac{1}{2}\vec{u}\cdot\vec{u}$$

for a calorically perfect gas with (constant) isentropic exponent γ, a shear stress tensor

$$\vec{\vec{\tau}} = \tau_{ij}\vec{e}_i\vec{e}_j = 2\mu\left(\frac{1}{2}\left(\frac{\partial u_i}{\partial x_j} + \frac{\partial u_j}{\partial x_i}\right) - \frac{1}{3}\delta_{ij}\vec{\nabla}\cdot\vec{u}\right)\vec{e}_i\vec{e}_j$$

with viscosity μ, and heat conduction $\vec{q} = -k\vec{\nabla}T$, where k is the heat conductivity and T is the temperature. The symbols x, $\vec{e}$, and δ_{ij} represent the space variable, unit vector, and Kronecker's delta

$$\delta_{ij} = \begin{cases} 0 & \text{if } i \neq j \\ 1 & \text{if } i = j \end{cases}$$

respectively, written with Einsteinian notation in the i (horizontal) and j (vertical) directions. Although the second (bulk) viscosity might be very important [70, 71], it will be neglected for now due the lack of experimental data for many mixtures of interest. This will cause an underestimation of the viscous effects, especially where compressibility is important. The Euler equations are obtained when viscosity and thermal conduction are removed by setting $\mu = 0$ and $k = 0$.

The variables can be non-dimensionalized by their dimensional (represented with the circumflex accent ˆ) counterparts at a reference state (subscript ref)

$$\hat{\rho}_{\text{ref}}, \quad \hat{p}_{\text{ref}}, \quad \hat{T}_{\text{ref}}, \quad \hat{x}_{\text{ref}}, \quad \hat{u}_{\text{ref}} = \sqrt{\frac{\hat{p}_{\text{ref}}}{\hat{\rho}_{\text{ref}}}}, \quad \hat{t}_{\text{ref}} = \frac{\hat{x}_{\text{ref}}}{\hat{u}_{\text{ref}}}, \quad \hat{\mu}_{\text{ref}} = \hat{\rho}_{\text{ref}}\hat{u}_{\text{ref}}\hat{x}_{\text{ref}}, \quad \text{and} \quad \hat{k}_{\text{ref}} = \frac{\hat{\rho}_{\text{ref}}\hat{u}^3_{\text{ref}}\hat{x}_{\text{ref}}}{\hat{T}_{\text{ref}}}$$

where density, pressure, temperature, and time set all the reference states.

1.7.3 Initial conditions

The first study investigates shock reflection from a wedge where the initial conditions were simply unshocked quiescent gas around the wedge, and post-shock conditions a short distance from the wedge tip, prescribed by the incident shock speed and the isentropic exponent. The initial conditions are illustrated in figure 1.8a, but the orientation of the shock with respect to the domain will be discussed in section 1.8.

A novel initial condition is used in the second and third studies. An ideal triple shock calculated with three shock theory is imposed upon the domain for initial conditions, as illustrated in figure 1.8b. The triple point in this initial configuration travels towards the bottom wall from which it will reflect and provide the shock reflection to be studied. The pre-reflection Mach shock becomes the incident shock for the reflection and so its strength is chosen accordingly. The angle between the pre-reflection Mach stem normal and the bottom wall is equivalent to the wedge angle, and the pre-reflection incident shock (which disappears when the triple point reflects) is perpendicular to the bottom wall.

The triple point was initially positioned sufficiently high above the reflecting surface to allow the shocks to adopt their steady viscous profiles before reflecting. This distance was estimated with one-dimensional simulations of viscous shock waves initiated from discontinuities.

1.7.4 Frame of reference

The laboratory frame of reference was used for simulating shock reflections from a wedge in section 1.8, as done in previous works. Using a moving frame of reference requires

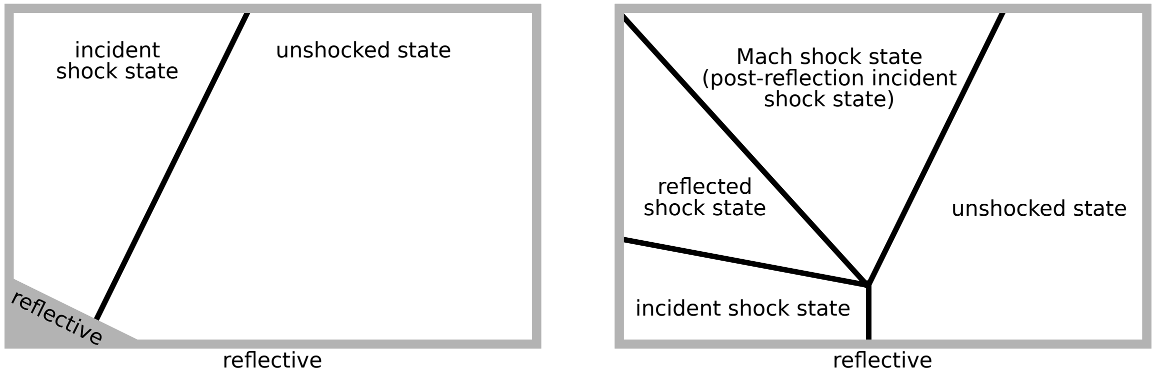

(a) Shock wave reflection

(b) Triple shock reflection

Figure 1.8: Initial conditions for shock wave reflection (a) and triple point reflection (b) from the bottom wall; the triple shock structure's Mach shock has the desired incident shock strength

implementing a moving boundary. However, triple shock reflections can easily be simulated in the laboratory frame of reference or a frame moving parallel to the reflecting surface. The pre-reflection triple point speed, parallel to the reflecting surface, is used in section 1.9 and the post-reflection triple point in section 1.10. These frames of reference reduce the maximum velocity relative to the grid, allowing greater inviscid time steps for a given Courant-Friedrichs-Lewy (CFL) number, and permit smaller domains than simulations performed purely in the laboratory frame of reference. The moving frame can even focus only the shock reflection process, allowing even smaller domains, at the expense of some boundary error from outflow. This will be used to achieve high Reynolds number flows.

1.7.5 Solver type

Finite volume methods are the state of the art for discretizing the Euler and Navier-Stokes equations [72]. The Riemann problem is solved at the volume interfaces using Godunov's method [73] or approximations thereof. While limited to first-order accuracy near discontinuities, solvers can reach second-order or higher accuracy in smooth regions.

A plethora of different solvers have been used to investigate the inviscid shock reflection problems. Takayama and Jiang [74], Mach [17], and Lau-Chapdelaine and Radulescu [75] (to be presented in section 1.8) have compared different solvers for shock reflections, using the inviscid Euler equations, and found many differences in the results. Quirk [76] also compared shortcomings of Riemann solvers and suggested selecting solvers adaptively depending on the circumstances in the flow.

Problems and differences between solvers stem from the use of the Euler equations. While the Euler equations are theoretically inviscid, solving them numerically introduces artificial diffusion, due to discretization of the domain, which depends strongly on the resolution and the type of solver. Past successes using inviscid equations for shock reflection can be attributed to qualitative comparisons of only some aspects of simulations to experiments, in part due to the difficulty in measuring the flow field, to the insensitivity of certain aspects of shock reflection to viscosity, and to artificial viscosity levels mimicking the physical viscosity of experiments. The artificial viscosity produced by discretization decreases with grid size as the discretized Euler equations converge to the inviscid case. The Navier-Stokes equations can be used to impart a physical viscosity which can render the numerical diffusion negligible if the problem is sufficiently resolved. This removes the dependence of the results on the solver selection.

1.7.6 Grid and boundary conditions

In order to study shock reflections, a reflecting surface must be implemented in the domain. Symmetry and free-slip reflective boundaries are of interest because of their relevance to shock reflections in detonations. Four typical ways of doing this are shown in figure 1.9. An easy implementation on a Cartesian grid is to use a staircase boundary, shown in figure 1.9a, where the reflecting surface is approximated by snapping it to the closest grid intersections and disallowing flux across the boundaries. While simple, it introduces roughness to the reflecting surface which has been shown in experiments [77–79] to affect the reflection differently than smooth surfaces.

Many numerical studies have used grid-aligned reflecting surfaces with Cartesian meshes [44, 52–54] by rotating the flow with respect to the grid, as illustrated in figure 1.9b. The reflecting boundary is easily treated this way by imposing a zero-flux rule across it, but difficulties arise where the shock discontinuity intersects the boundaries. A moving shock must be set as the top boundary condition [44, 54], taking care to consider errors that will arise as the flow negotiates between the ideal boundary condition by placing the top boundary far away to delay the arrival of errors at the region of interest, for example, but this can greatly increase the domain size. Another problem arises at the wedge tip: using a grid aligned wedge with post-shock conditions immediately before the wedge tip [52–54,57,58] becomes a problem when the maximum turning angle of an oblique shock is exceeded, often the case under detonation-like conditions. In these cases, a bow shock replaces the attached oblique shock wave at the wedge tip, causing leakage around the wedge tip in this implementation. This simulates an asymmetric wedge, often used in experiments, but the wedge tip conditions may affect the reflection configuration and does not accurately represent shock reflections in detonations.

The reflecting surfaces can be made to cut through cells, as shown in figure 1.9c, allowing the incident shock to be perpendicular to the domain boundaries and the wedge tip to behave (almost) symmetrically. The embedded boundary technique [80], and possibly other schemes, may not guarantee flow conservation (*i.e.* impermeability) as demonstrated in section 1.8 with the AMRITA [64] computational environment, where different results were obtained when comparing the embedded boundary technique [80] and a grid-aligned boundary.

The use of curvilinear grids or unstructured meshes which change orientation at the wedge tip, exemplified in figure 1.9d, is promising but unfortunately not implemented in AMRITA [64] computational package that will be used for section 1.8, nor the mg [81] package used in sections 1.9 and 1.10.

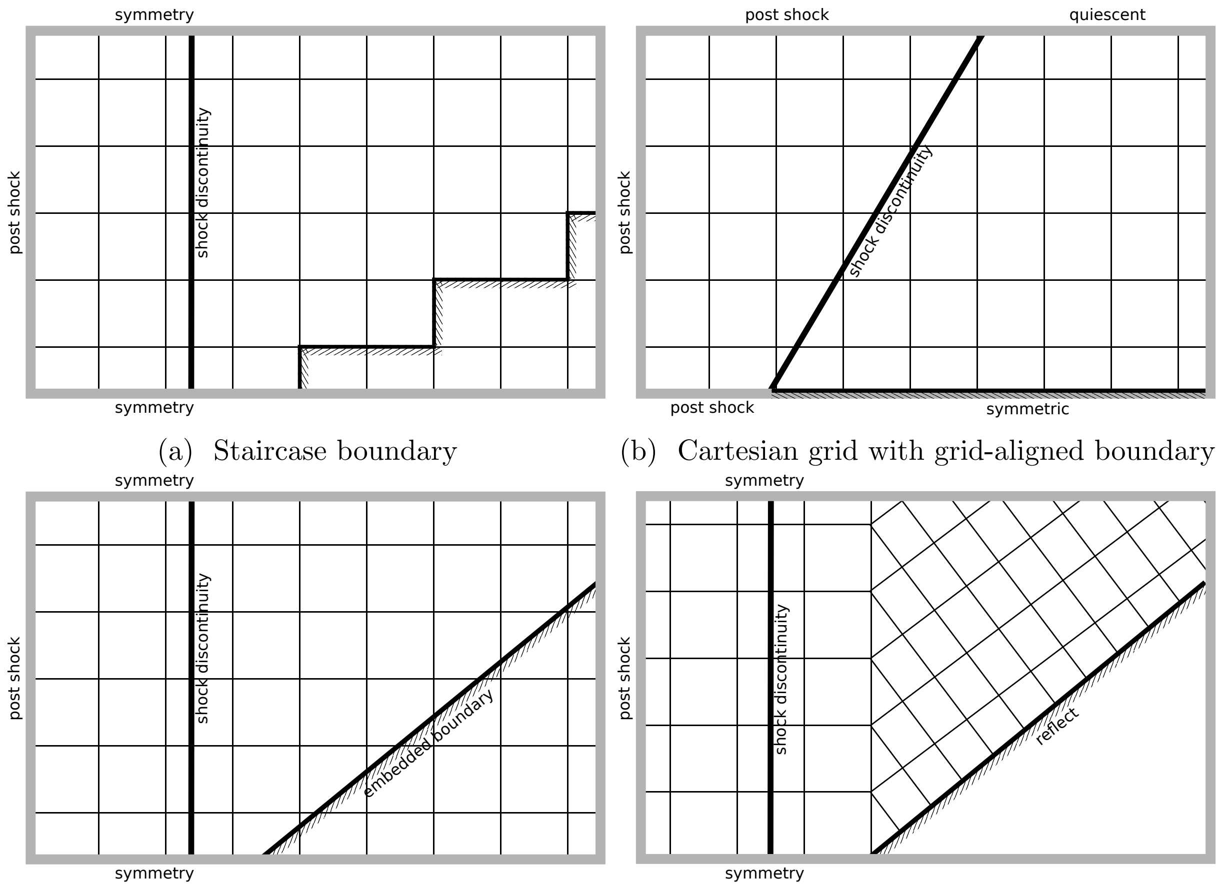

(a) Staircase boundary

(b) Cartesian grid with grid-aligned boundary

(c) Embedded boundary

(d) Curvilinear grid with grid-aligned boundary

Figure 1.9: Illustrations of possible boundary and conditions grids for shock reflection simulations

Finally, Henderson, Vasilev *et al.* [57, 58] numerically studied shock reflections using curvilinear unsteady, self-similar grids with shock tracking (not shown here). This method allows very resolved early time steps and efficient use of computational mesh, but suffers problems in defining initial conditions, lose resolution with time, and require special implementation. This method will not be used.

A grid-aligned reflecting surface on the domain boundary, is used in this study, illustrated in figure 1.9b, along with an embedded boundary in section 1.8, where grid-aligned and embedded boundaries are compared.

By reflecting the triple shock structure on the grid-aligned surface in sections 1.9 and 1.10, the need to implement a wedge tip or embedded boundaries is removed. It also better represents conditions of triple point reflection in detonations, and achieves a smooth, flow-conserving axis of symmetry on the bottom wall.

The remaining boundaries are fixed to the initial conditions (or sometimes extrapolating) in sections 1.8 and 1.9. For section 1.10, a moving contact surface and moving shocks have been implemented as boundary conditions using time-dependant functions (at all meshes levels). The boundaries move the original (ideal) discontinuities with time, since their positions can be calculated exactly.

1.8 Non-uniqueness of solutions in asymptotically self-similar shock reflections

Authors: S. SM. Lau-Chapdelaine and M. I. Radulescu.

Status: This paper was published in Shock Waves, Volume 23, Issue 6, Pages 595-602, 2013. It was presented in November 2013 at the 66th meeting of the American Physical Society Division of Fluid Dynamics in Pittsburgh, United States of America.

Although first submitted before starting the degree in January 2013, extensive revisions were necessary into the first year of the PhD. The work had to be carefully redone with a different orientation and boundary, and collaboration with the author of the numerical package was necessary to publish the numerical reproduction script online.

In a preliminary attempt to estimate the limits of these phenomena, the shock reflection over a circularly curved concave wedge was simulated. The pretence was that a curved surface would reduce the parameter space from three to two by allowing multiple (continuous) wedge angles to be tested for a given Mach number and isentropic exponent. However, the leading wedge conditions were found to affect the reflection configuration, changing the irregular to regular reflection transition to an angle drastically above that predicted by the sonic and detachment criteria. This paper shows that the initial reflection conditions can be important in selecting the reflection type.

Shock Waves, Volume 23, Issue 6, Pages 595-602, 2013.
DOI 10.1007/s00193-013-0469-0

Non-uniqueness of solutions in asymptotically self-similar shock reflections

S. She-Ming Lau-Chapdelaine · Matei I. Radulescu

Received: 29 June 2011 / Revised: 15 July 2013 / Accepted: 13 August 2013 / Published online: 24 September 2013

Abstract The present study addresses the self-similar problem of unsteady shock reflection on an inclined wedge. The start-up conditions are studied by modifying the wedge corner and allowing for a finite radius of curvature. It is found that the type of shock reflection observed far from the corner, namely regular or Mach reflection, depends intimately on the start-up condition, as the flow "remembers" how it was started. Substantial differences were found. For example, the type of shock reflection for an incident shock Mach number $M = 6.6$ and an isentropic exponent $\gamma = 1.2$ changes from regular to Mach reflection between 44° and 45° when a straight wedge tip is used, while the transition for an initially curved wedge occurs between 57° and 58°.

Keywords Shock wave · Reflection · Pseudosteady · Unsteady

1 Introduction

The reflection of a steadily moving shock wave on a straight inclined wall has attracted much attention in recent decades due to its fundamental importance in unsteady gas dynamics and in all compressible media (gases, liquids, solids, nuclear matter, interstellar medium, granular media and detonation waves). Consider a shock wave as it travels at a velocity D, in the inertial frame of reference, through a stationary medium with an isentropic exponent γ and speed of sound c_0. When the shock impinges upon a stationary wedge with an angle θ_w from the shock's normal, it will reflect from the wedge.

S. S.M. Lau-Chapdelaine
Université d'Ottawa University,
Department of Mechanical Engineering
161 Louis Pasteur
CBY A205
Ottawa, ON, Canada, K1N-6N5
e-mail: –

Originally published by Springer-Verlag Berlin Heidelberg. The final publication is available at `http://www.springerlink.com/openurl.asp?genre=article&id=doi:10.1007/s00193-013-0469-0` and through `link.springer.com`

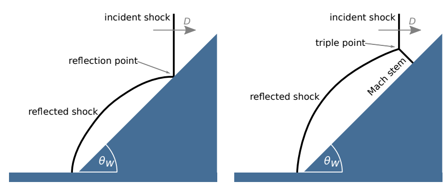

(a) Regular reflection (b) Mach reflection

Fig. 1 A moving shock, travelling at velocity D, strikes and reflects off of a stationary wedge of angle θ_w giving rise to a regular reflection (a) or a Mach reflection (b) depending on flow properties

The shock reflection will generally adopt one of two forms, either a regular or Mach reflection, exemplified by Fig. 1. The Mach reflection type can be further subdivided into different regimes of reflections which have been classified by Ben-Dor [1] and more recently by Semenov et al. [2,3] and Vasilev et al. [4]. The isentropic exponent, the geometry (angle of the wall), and the Mach number of the incident shock $M_i = D/c_0$ uniquely define the problem; the type of reflection is subject to change with any of those variables. Thorough reviews of the shock reflection problem have been provided by Hornung [5] and Ben-Dor [1].

Experiments will typically fix the shock strength and gas type (M_i and γ) and vary the wedge angle θ_w. Mach reflections will occur at smaller wedge angles than regular reflections; however, there is a range of angles where both Mach and regular reflections are possible. This overlap has been observed in both steady and pseudosteady flows. Much attention has been devoted to the many types of reflection configurations, the conditions under which they occur, and which factors favour the appearance of one type over another, especially under conditions where both regular and Mach reflections are possible solutions [6–9].

When a shock wave reflects over a sharp corner, the absence of a characteristic length scale renders the problem self-similar. In two-dimensions, the problem thus admits a similarity solution in terms of a combination of the space variables x and y and time t, in this case simply $x/(c_0t)$ and $y/(c_0t)$ [10]. Indeed, such self-similar flow-fields corresponding to impulsively started gas dynamic flow-fields abound in unsteady gas dynamics (e.g., shock diffraction [10], shock refraction [11], blast waves and implosion problems [12], etc.).

The self-similar configuration of the reflection emerges from a singularity at the sharp tip of the reflecting surface. When the mathematical formulation of the problem is described by the inviscid Euler equations, this does not pose any serious difficulty, as the problem is well-defined in similarity variables. However, numerical verification of postulated self-similar solutions becomes difficult because the computational grid cannot resolve any physical or temporal singularity. Likewise, if one considers the real physical solution near the corner of finite dimension, occurring at scales commensurate with the mean free path, the problem loses its self-similarity due to the presence of physical length and time scales associated with mass, momentum, and energy transfer by molecular diffusion and the dimension of the corner. Thus no real problem is strictly self-similar. It is only once that the evolution of the problem has evolved on length and time scales much larger than those associated with the start-up process that one may expect a weak, asymptotic form of self-similarity.

Shock reflections over obstacles with variable corner geometries (e.g., cylindrical, multiple cumulative wedges) have previously been studied [8,13–16] but these studies only explored flow fields in proximity of the corner. In order to study the evolution of a shock reflection towards self-similarity, the present work focused on the problem of shock reflection over a straight wedge with a finite radius of curvature R assigned to the initial corner as shown in Fig. 2. The evolution of the shock reflection was studied over the straight portion of the wedge over length scales much larger than R. The objective was to determine whether the solution of the asymptotically self-similar problem, in the limit that R, relative to the distance travelled, becomes infinitesimally small, agreed with the solution of the self-similar problem, particularly in the regime of shock reflections where both regular and Mach reflections are possible.

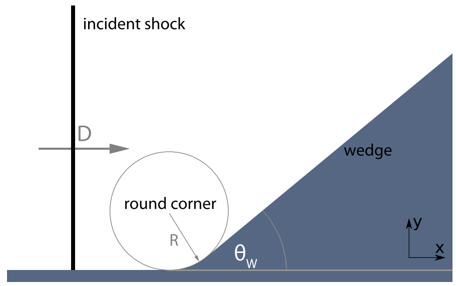

Fig. 2 Wedge geometry: wedge with rounded corner

2 Problem definition and methodology

2.1 Problem definition

The problem was addressed through numerical experiments. The reflection problem was modeled by the Euler equations for a calorically perfect gas

$$\frac{\partial W}{\partial t} + \frac{\partial F}{\partial x} + \frac{\partial G}{\partial y} = 0 \tag{1}$$

with

$$W = \begin{bmatrix} \rho \\ \rho u \\ \rho v \\ E \end{bmatrix}, \quad F = \begin{bmatrix} \rho u \\ \rho u^2 + p \\ \rho uv \\ (E+p)u \end{bmatrix}, \quad G = \begin{bmatrix} \rho v \\ \rho vu \\ \rho v^2 + p \\ (E+p)v \end{bmatrix} \tag{2}$$

where ρ is the density, u is the x-component of velocity, v is the y-component of velocity and E is the total energy, given by

$$E = \frac{p}{\gamma - 1} + \frac{1}{2}\rho u^2 + \frac{1}{2}\rho v^2. \tag{3}$$

Consistent with the absence of viscous terms in the Euler equations, the boundary conditions along the solid surfaces were reflective with vanishing normal velocity (no penetration) but allowed tangential velocities.

The initial conditions consisted of a planar shock wave propagating in the positive x-direction, see Fig. 2. Given the shock Mach number, the flow properties behind the shock are uniquely given by the Rankine-Hugoniot jump conditions.

The solution is reported in non-dimensional form. The initial density ρ_0 and the initial pressure p_0 were chosen as characteristic scales for pressure and density. The governing equations remain invariant under non-dimensionalization if the velocity is normalized by $\sqrt{p_0/\rho_0}$. In summary, the non-dimensional variables, denoted by a tilde, are:

$$\tilde{\rho} = \frac{\rho}{\rho_0}, \;\; \tilde{p} = \frac{p}{p_0}, \;\; \tilde{u} = \frac{u}{\sqrt{\frac{p_0}{\rho_0}}}, \;\; \tilde{v} = \frac{v}{\sqrt{\frac{p_0}{\rho_0}}}. \tag{4}$$

In the case of a sharp corner, the problem is self-similar and there is no characteristic length scale. Accordingly, to report the numerical results where the grid spacing provides a characteristic scale of the numerical approximation, the x and y variables are such that a value of unity corresponds (arbitrarily) to one base grid spacing. Likewise, the cases where a finite radius corner is included use the same non-dimensionalization for comparison purposes.

2.2 Numerical method

A numerical solution to the problem stated above was obtained by discretizing the governing equations with a finite volume scheme using Roe's linearised Riemann solver [17,18] to evaluate the fluxes. The solution was implemented in the AMRITA computational system developed by James Quirk [19], designed to facilitate the exchange of computational investigations among different users and adopting a philosophy where the source code is readily available for third-party scrutiny and packaged to allow verification of results obtained. The script used to run the numerical simulations is available as electronic supplementary material (Online Resource 1), and in the AMRITA newsgroup [20], where discussion about the computational system can also be found.

A base grid of 300 by 250 was used, aligned with the wedge wall (see Fig. 3). An adaptive mesh refinement technique was used to improve the accuracy of the solution near discontinuities as exemplified in Fig. 3. The mesh was refined around regions with density gradients, internal boundaries and behind the reflected and Mach shocks. Unless otherwise noted, four levels of mesh refinement were used, doubling the number of grid points in each direction at every level; the most refined grid spacing was thus 2^{-4}.

The curved corner and upstream boundary were implemented using the embedded boundary technique described by Xu et al. [21]. This permitted the use of a Cartesian computational grid. The grid is not fitted to the curved boundary. The boundary is defined as a user-selected function. The solution vector at the ghost cells situated across the boundary are specified to suppress flow normal to the boundary curve.

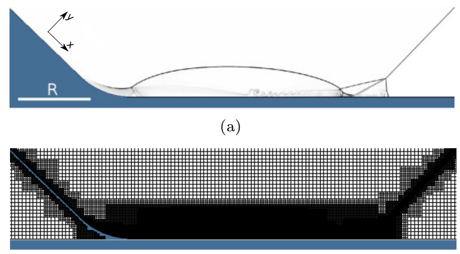

(a)

(b)

Fig. 3 Density gradient (a) and corresponding adaptive mesh (b) with four refinement levels ($M_i = 6.6$, $\gamma = 1.2$, ramp angle $\theta_w = 44°$, $R = 20$)

The computations were initialised using the Rankine-Hugoniot shock solutions behind a shock discontinuity positioned eight units upstream of the start of the wedge. However, the exact position of the shock did not influence the results.

The set of fixed parameters investigated were an isentropic exponent of $\gamma = 1.2$ and incident shock Mach number of $M_i = 6.6$. These values correspond to the typical conditions of shock reflections in cellular detonation waves [22] with a heat release of $Q/RT_0 \approx 50$. A vast amount of literature now exists on the detonation shock reflection dynamics with these parameters (see reference [22] and references therein). The angle of the ramp was varied to determine the transition point between regular reflection and Mach reflection. The curved corner had a radius of $R = 20$.

2.3 Numerical verification

To test the convergence of the results obtained with grid refinement, different resolutions were considered for the wedge with a sharp corner. For each resolution, the wedge angle was modified in increments of 1°. For a wedge angle of $\theta_w = 44°$, a Mach reflection was always observed with the different grid resolutions. For a wedge angle of $\theta_w = 45°$, a regular reflection was always observed. With increasing resolution, the reflection pattern remained invariant, as can be seen in Fig. 4.

A comparison of three solvers (Roe's [17,18], Eindfelt's Harten-Lax-van-Leer (HLLE) [23], and Godunov's [24] solvers) is shown in Fig. 5. The numerical experiments with the sharp-cornered wedge were also performed with different orientations of the base grid, and are superimposed on the same figure. When the base grid was aligned with the x-axis (normal to the inci-

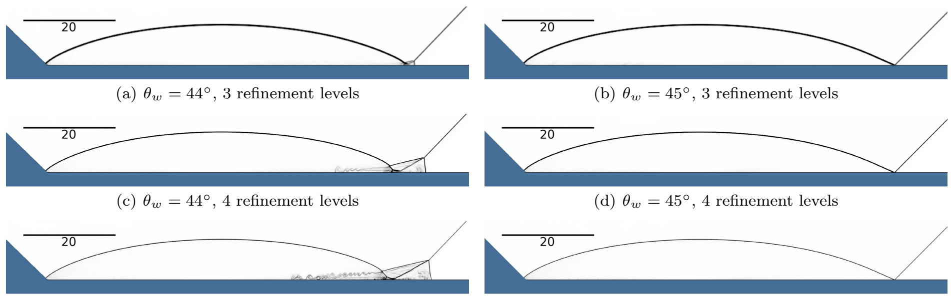

(a) $\theta_w = 44°$, 3 refinement levels

(b) $\theta_w = 45°$, 3 refinement levels

(c) $\theta_w = 44°$, 4 refinement levels

(d) $\theta_w = 45°$, 4 refinement levels

(e) $\theta_w = 44°$, 5 refinement levels

(f) $\theta_w = 45°$, 5 refinement levels

Fig. 4 Shock waves ($M_i = 6.6$, $\gamma = 1.2$) reflecting off wedges with angles at $\theta_w = 44°$ ((a), (c), (e), Mach reflection) and $\theta_w = 45°$ ((b), (d), (f), regular reflection) with sharp corners and a range of resolutions; the distance indicator refers to a distance measured in base grid spacings, as explained in the text

dent shock), the inclined wall was captured with the embedded boundary technique.

A range of Mach stem sizes can be seen in Fig. 5, depending on the orientation and solver used. Nevertheless, the differences between the results obtained with both grid orientations were relatively small for a wedge angle near the transition angle. The solution obtained with both grids show the same flow features. These errors are potentially due to approximations of the embedded boundary technique. For this reason, and to minimize such errors, the grid was oriented with the wedge wall. The Godunov and HLLE solvers used in conjunction with the embedded boundary wedge gave very similar results to the Roe solver used with the grid-oriented wedge. The results shown in this paper were achieved using Roe's solver with the grid-aligned wedge.

3 Results

The results of the numerical calculations are presented below as pseudo-schlieren records. The absolute value of the density gradients is shown according to the greyscale given in Fig. 6.

3.1 Reflection over a wedge with a sharp corner

Figure 4 illustrates the resulting flow-fields obtained for a shock reflecting off a ramp with an angle of $\theta_w = 44°$ and $\theta_w = 45°$ and a sharp corner. The domain has been cropped to show the area of interest. As discussed above, at $\theta_w = 45°$, a regular reflection is observed, while at $\theta_w = 44°$, the reflection takes the form of a Mach reflection, characterised by a Mach shock travelling nearly perpendicular to the wall. A second triple-shock configuration (triple-point), also with an associated slip line, which becomes unstable due to the Kelvin-Helmholtz instability, can be found along the reflected wave and corresponds to the sub-regime of double Mach reflection [5]. This double Mach reflection has a negative reflection angle (between the triple-point path and reflected wave) [25].

3.2 Reflection over a wedge with a rounded corner

Figure 7 shows the flow-fields of the shock reflection over a wedge with a rounded corner after the reflection point has travelled a distance approximately eight times the radius of the corner. Double Mach reflections are seen at ramp angles of $\theta_w = 44°$, $\theta_w = 51°$, and $\theta_w = 57°$. A regular reflection appears at a ramp angle of $\theta_w = 58°$. The transition from Mach to regular reflection now occurs at a significantly larger angle ($\theta_w = 57.5° \pm 0.5°$) as compared with the critical wedge angle for transition with a sharp corner ($\theta_w = 44.5° \pm 0.5°$).

The evolutions of reflections for wedge angles of $\theta_w = 57°$ and $\theta_w = 58°$ with curved corners are shown in Fig. 8. For the wedge angle $\theta_w = 57°$, the reflection process asymptotes to a new self-similar solution, a (double) Mach reflection, as the shock travels a large distance from the rounded corner. This differs from the one obtained over a sharp-cornered wedge at the same angle shown in Fig. 9, which was a regular reflection. The reflection over the $\theta_w = 58°$ wedge keeps the form of a Mach reflection for approximately two-and-a-half corner radii after tangency with the wedge. The triple point then collides with the wedge to become a reg-

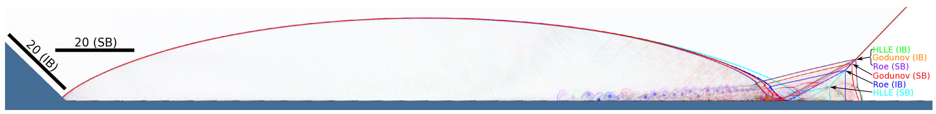

Fig. 5 Comparison of grid orientations and solvers ($M = 6.6$, $\gamma = 1.2$, $\theta_w = 44°$): grid aligned with wedge (SB); grid normal to incident shock / embedded-boundary wedge (IB)

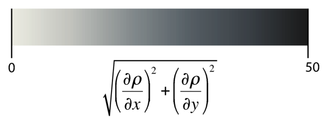

Fig. 6 Grayscale for rendering the numerical results of density gradients.

ular reflection. The trajectory of the triple-point for $\theta_w = 57°$ is shown in Fig. 8(g). The triple point moves away from the wedge and does not appear to collide with it at a distance of up to ten times that of the radius of curvature. It is evident that the new asymptotically self-similar solution consists of a Mach reflection which grows with time in a linear fashion.

Although the results reported were only for a distinct set of parameters in gases with high shock strength and low isentropic exponent typical of gaseous detonations, similar results and conclusions were also obtained for weaker shock reflections with an isentropic exponent corresponding to a diatomic gas like air. Numerical experiments with $\gamma = 1.4$ and $M_i = 3$, for example, revealed a transition angle from Mach to regular reflection at $\theta_w = 50.5° \pm 0.5°$. With an initially curved wedge, Mach reflections were maintained for larger wedge angles.

4 Discussion

For parameters $M_i = 6.6$ and $\gamma = 1.2$, the determined transition between regular and Mach reflection of $44.5° \pm 0.5°$ over the wedge with a sharp corner is in good agreement with the sonic criterion [9], modeled by the two-shock theory. This criterion predicts a transition at $\theta_w = 44.47° \pm 0.01°$, while the detachment criterion predicts a transition at $\theta_w = 44.42° \pm 0.01°$. The transition from Mach to regular reflection occurs when the flow behind the reflected shock becomes outside the range of influence of the corner (i.e., when the flow behind the reflection point is supersonic. Thus, it appears that the self-similar solution is indeed established such that the shock reflection retains its shape as it grows with time.

However, the numerical experiments conducted with the curved corner illustrate that the same self-similar solution is not recovered in the far field, when the corner is initially curved. A possible explanation for this is likely also related to the sonic criterion, see below. In a progressively curved ramp, the reflection starts out invariably as a Mach reflection due to the initial small angle. As the wedge angle increases continuously along the curved corner, the Mach stem likely remains strong enough to communicate a scale of length; the entire reflection configuration is subject to the changing angle [16]. The shock reflection is then likely able to maintain this subsonic pathway past the corner along the flat portion of the wedge. Future studies could address this mechanism by tracking the path of acoustic signals.

It is also instructive to consider the present results in view of previous studies performed with modifications to the straight wedge problem. The problem of unsteady shock reflection over curved surfaces has been addressed by a number of authors [8, 13–15]. These studies did not address the continuation of the curved surface into a straight surface; i.e., the asymptotically self-similar regime studied here. Instead, they were concerned with the transition of the Mach reflection to regular reflection over the curved wedge, which occurs when the triple-point trajectory eventually merges with the curved wall. Similar to the present study, it was found that the wedge angle at which the transition from Mach to regular reflection occurs is larger than the angle obtained for reflection on a straight wedge. It has also been shown that the transition angle decreases with radius of curvature [26], tending towards the transition angle of a reflection off a straight wedge. The transition angle for a reflection over a concave circle has been analytically predicted using the sonic criterion [9] by Ben-Dor and Takayama [13] but the proposed models are independent of the radius of curvature. A model incorporating the radius of curvature remains yet incomplete [27]. Their model "A" predicts a transition at $\theta_w \approx 63°$ for $M = 6.6$ and $\gamma = 1.2$ on the concave circle. The value derived from Ben-Dor and Takayama's model is higher than what was obtained for a curved wall followed by a straight wedge in this study, namely $\theta_w = 57.5° \pm 0.5$. This difference is an expected result

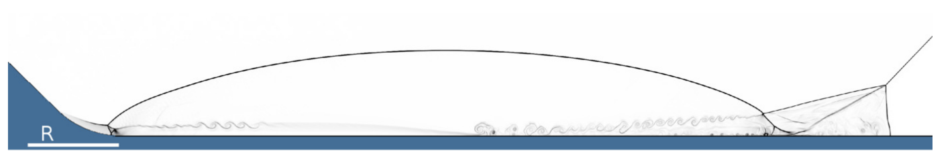

(a) $\theta_w = 44°$

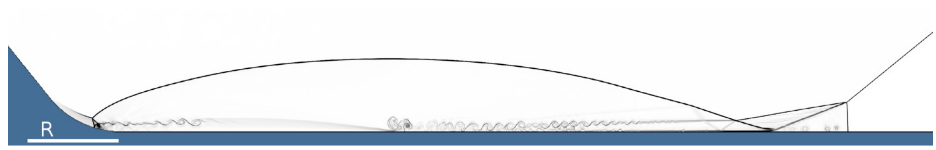

(b) $\theta_w = 51°$

(c) $\theta_w = 57°$

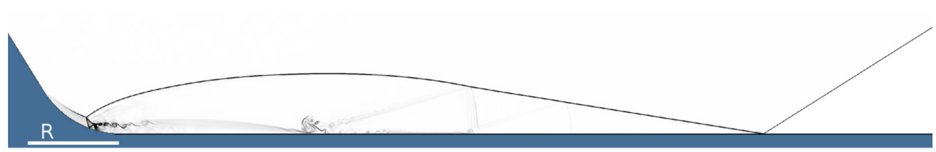

(d) $\theta_w = 58°$

Fig. 7 Shock waves ($M_i = 6.6$, $\gamma = 1.2$, $R = 20$) reflecting off wedges with angle (a) $\theta_w = 44°$, (b) $\theta_w = 51°$, (c) $\theta_w = 57°$, (d) $\theta_w = 58°$, and curved corners

due to slight difference between the two problems. For the initially curved wedge in this study, the Mach reflection vanishes when the trajectory of the triple point intersects the straight part of the wedge, as shown in Fig. 8. In the continuously curved wall, the Mach reflection vanishes when the trajectory of the triple intersects the curved part of the wedge, which, from simple geometric arguments occurs for larger angles than in the problem studied here. Nevertheless, the similarity in results suggests that the persistence of the subsonic pathway for the curved wall, used by Ben-Dor and Takayama to model their results, is the likely explanation for the delayed transition to regular reflection.

Another problem analogous to the present is the shock reflection over two sequential straight wedges, where the angle of the second wedge is greater than the first. This problem has been studied by Ben-Dor et al. [28,29]. However, it was found that the reflection pattern quickly recovered the configuration expected had the first wedge been absent.

5 Conclusion

The present study shows unambiguously that the details of the start-up of an asymptotically self-similar solution play a very important role in determining the final asymptotic self-similar solution. The shock reflection studied showed that the solution achieved from reflection past a straight wedge, which starts with a finite curvature, persists as a Mach reflection in the far-field through wedge angles far superior to those observed over sharp-cornered wedges. As the radius of the rounded corner becomes insignificant in comparison to the distance travelled by the incident shock, the solution of the asymptotically self-similar problem disagrees with the solution of the self-similar problem.

The curved wedge corner introduces a length scale to the problem in a similar way that viscous effects or shock relaxation phenomena would. While viscous effects [30,31] and the presence of relaxation reduce the transition wedge angle [9], these length scales van-

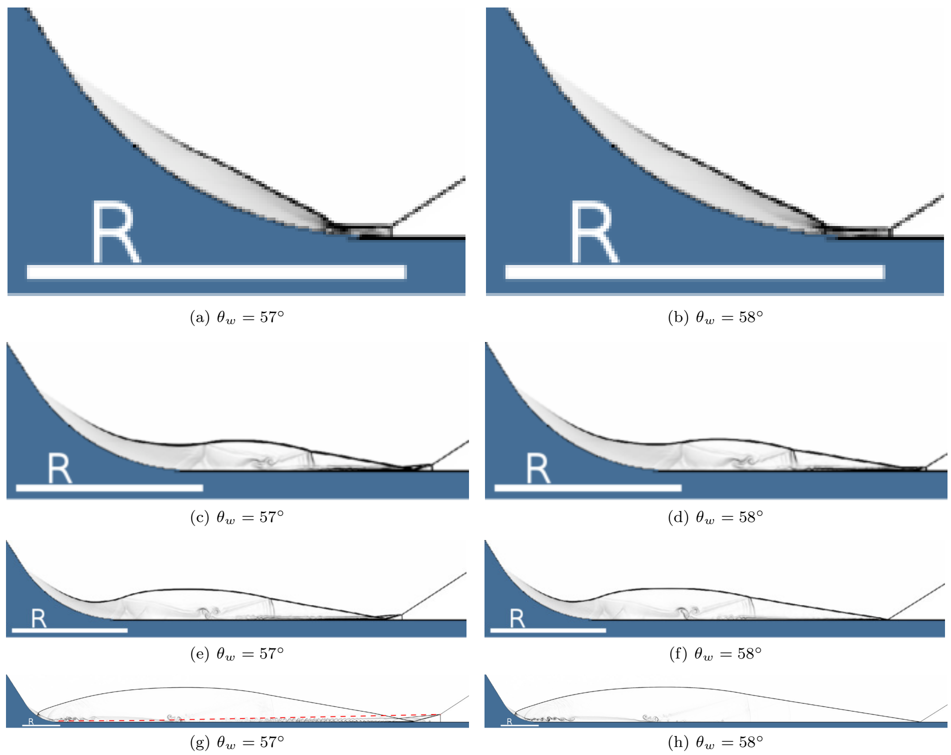

(a) $\theta_w = 57°$ (b) $\theta_w = 58°$

(c) $\theta_w = 57°$ (d) $\theta_w = 58°$

(e) $\theta_w = 57°$ (f) $\theta_w = 58°$

(g) $\theta_w = 57°$ (h) $\theta_w = 58°$

Fig. 8 Evolution of a shock wave ($M_i = 6.6$, $\gamma = 1.2$, $R = 20$) reflecting off a $\theta_w = 57°$ wedge ((a), (c), (e), (g)) and $\theta_w = 58°$ wedge ((b), (d), (f), (h)) with rounded corners; triple-point path has been superimposed (dashed-line) on sub-figure (g)

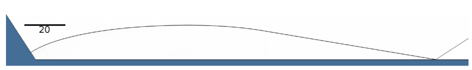

Fig. 9 Shock wave ($M_i = 6.6$, $\gamma = 1.2$) reflecting off a wedge $\theta_w = 57°$ with a sharp corner

ish asymptotically as the reflection grows. Their effects only dominate the solution at early times, while the later time solution may still be influenced by the start-up conditions, as illustrated in the present study. Indeed, the present study shows that the flow patterns obtained from the start-up conditions persist through to scales significantly larger than those at the corner, and play a dominant role determining what is obtained into the asymptotic pseudosteady configuration. Similar results have been reported by Henderson and Menikoff [6] with regards to shock reflections in steady-state flows.

In view of the present findings, it appears worthwhile to re-evaluate other self-similar problems of gas dynamics, such as Taylor-Sedov blast waves, or the problem of shock diffraction at a sudden area change, to determine the influence of the starting conditions on the solution obtained in the far field. This issue is particularly important in view of current numerical simulation techniques used to solve these problems, which attempt to regularize the start-up conditions to resolve them with a finite size computational grid.

Acknowledgements The authors wish to thank James Quirk for his support with the AMRITA system.

This work was sponsored by a Natural Sciences and Engineering Research Council of Canada (NSERC) Discovery grant to M. I. Radulescu, with further support from the NSERC H2CAN Strategic Network of Excellence, and a NSERC Alexander Graham Bell Canadian Graduate Scholarship to S. S.M. Lau-Chapdelaine.

References

1. Ben-Dor, G.: Shock wave reflection phenomena. Springer, (2007)
2. Semenov, A. N., Berezkina, M. K., Krasovskaya, I. V.: Classification of shock wave reflections from a wedge. Part 1 : Boundaries and domains of existence for different types of reflections. Tech. Phys., 54, 4, 491-496 (2009)
3. Semenov, A. N., Berezkina, M. K., Krasovskaya, I. V.: Classification of shock wave reflections from a wedge. Part 2 : Experimental and numerical simulations of different types of Mach reflections. Tech. Phys., 54, 4, 497-503 (2009)
4. Vasilev, E. I., Elperin, T., Ben-Dor, G.: Analytical reconsideration of the von Neumann paradox in the reflection of a shock wave over a wedge. Phys. Fluids, 20, 046101 (2008)
5. Hornung, H.: Regular and Mach reflection of shock waves. Annu. Rev. Fluid Mech., 18, 33-58 (1986)
6. Henderson, L. F., Menikoff, R.: Triple-shock entropy theorem and its consequences. J. Fluid Mech., 366, 179-210 (1998)
7. Henderson, L. F., Lozzi, A.: Experiments on transition of Mach reflexion. J. Fluid Mech., 68, 139-155 (1975)
8. Henderson, L. F., Lozzi, A.: Further experiments on transition to Mach reflexion. J. Fluid Mech., 94, 541-559 (1979)
9. Hornung, H. G., Oertel, H., Sandeman, R. J.: Transition to Mach reflexion of shock waves in steady and pseudosteady flow with and without relaxation. J. Fluid Mech., 90, 541-560 (1979)
10. Jones, D. M., Martin P., Thornhill C. K.: A note on the pseudo-stationary flow behind a strong shock diffracted or reflected at a corner. Proc. Roy. Soc. Lond. A, 209, 238-248 (1951)
11. Henderson, L. F.: Handbook of Shock Waves, vol. 2, Chapter 8.2, Two-Dimensional Interactions: The Refraction of Shock Waves. Academic Press, 181-203 (2001)
12. Landau, L. D., Lifshitz, E. M.: Course of Theoretical Physics, Volume 6: Fluid Mech., Second English Edition. Pergamon Press, 403-411 (1987)
13. Ben-Dor, G., Takayama, K.: Analytical prediction of the transition from Mach to regular reflection over cylindrical concave wedges. J. Fluid Mech., 158, 365-380 (1985)
14. Itoh, S. Okazaki, N., Itaya, M.: On the transition between regular and Mach reflection in truly non-stationary flows. J. Fluid Mech., 108, 383-400 (1981)
15. Ben-Dor, G., Takayama, K., Kawauchi, T.: The transition from regular to Mach reflexion and from Mach to regular reflexion in truly non-stationary Flows. J. Fluid Mech., 100, 147-160 (1980)
16. Krasovskaya, I. V., Berezkina, M. K.: On reflection of shock waves and shock-wave configurations. Tech. Phys. Lett., 34, 177-179, (2008)
17. Roe, P. L.: Approximate Riemann solvers, parameter vectors, and difference schemes. J. Comput. Phys., 43, 357-372 (1981)
18. Roe, P. L., Pike, J.: Efficient construction and utilisation of approximate Riemann solutions. In: Computer methods in application science and engineering VI. Proceedings 6th International Symposium, Versailles, France; Netherlands, pp. 499-518 (1984)
19. Quirk, J. J.: AMRITA. VKI 29th CFD lecture series, Febuary 1998
20. Quirk, J. J.: AMRITA ebook > shock/detonation interaction with a ramp. Google Groups. https://groups.google.com/d/msg/amrita-ebook/tKmkJyL4TC0/xn9vrnFcG-EJ (2013), available through http://amrita-ebook.org/. Accessed 25 April 2013
21. Xu, S., Aslam, T., Stewart, D. S.: High resolution numerical simulation of ideal and non-ideal compressible reacting flows with embedded internal boundaries. Combust. Theory Model., 1, 113-142 (1997)
22. Mach, P., Radulescu, M. I.: Mach reflection bifurcations as a mechanism of cell multiplication in gaseous detonations. Proc. Combust. Inst., 33, 2279-2285 (2011)
23. Einfeldt, B., Munz, C. D., Roe, P. L., Sjögreen, B.: On Godunov-type methods near low densities. J. Comput. Phys., 92, 273-295 (1991)
24. Godunov, S.K.: A difference method for numerical calculation of discontinuous solutions of the equations of hydrodynamics. Matematicheskii Sbornik, 89, 271-306 (1959)
25. Gvozdeva, G. L., Borsch, V. L., Gavrenkov, S. A.: Analytical and Numerical Study of Three Shock Configurations with Negative Reflection Angle. In: Kontis, K. (ed.), 28th International Symposium Shock Waves, pp. 587-592. Springer, Berlin Heidelberg (2012)
26. Takayama, K., Sasaki, M.: Effects of radius of curvature and initial angle on the shock transition over concave or convex walls: Memorial Institute of High Speed Mechanics, Tohoku University., 46: 1-30 (1983)
27. Takayama, K., Ben-Dor, G.: Reflection and diffraction of shock waves over circular concave wall. Reports of the Institute of High Speed Mechanics, Tohoku University, 51: 43-87 (1986)
28. Ben-Dor, G., Dewey, J. M., Takayama K.: The reflection of a plane shock over a double wedge: J. Fluid Mech., 176, 483-520 (1987)
29. Ben-Dor, G., Dewey, J. M., McMillin, D. J., Takayama, K.: Experimental investigation of the asymptotically approached Mach reflection over the second surface in a double wedge reflection: Exp. Fluids, 6, 429-434 (1988)
30. Hornung, H. G., Taylor, J. R.: Transition from regular to Mach reflection of shock waves Part 1. The effect of viscosity in the pseudosteady case. J. Fluid Mech., 123, 143-153 (1982)
31. Ben-Dor, G.: A reconsideration of the three-shock theory for a pseudo-steady Mach reflection. J. Fluid Mech., 181, 467-484 (1987)

1.9 Viscous solution of the triple-shock reflection problem

Authors: S. SM. Lau-Chapdelaine and M. I. Radulescu.

Status: This paper [82] was published in the Shock Waves, Volume 26, Issue 5, Pages 551-560, 2016. Its predecessor [63] was presented at the 25th International Colloquium on the Dynamics of Explosions and Reactive Systems in Leeds, United Kingdom in 2015.

This study uses a new type of initial condition, the reflection of a three shock configuration, to study the presence of Kelvin-Helmholtz instability in shock reflections under detonation-like parameters. In view of the previous study, in section 1.8, viscous simulations are performed to remove ambiguity during the initial reflection, to reduce problems with solver selection, and to give a finite and real Reynolds number. Boundary condition problems are solved using the new reflection configuration. The simulations are resolved to the shock thickness and show no Kelvin-Helmholtz instabilities by the time first ignition is expected under the selected conditions. Analysis shows, however, that these instabilities are likely to arise on the time scale of the detonation cell.

Shock Waves, Volume 26, Issue 5, Pages 551-560, 2016.
DOI 10.1007/s00193-016-0674-8

Viscous solution of the triple-shock reflection problem

S. She-Ming Lau-Chapdelaine · Matei I. Radulescu

Received: 19 May 2016 / Revised: 6 June 2016 / Accepted: 14 June 2016 / Published: 12 July 2016

Abstract The reflection of a triple-shock configuration was studied numerically in two dimensions using the Navier-Stokes equations. The flow field was initialized using three shock theory, and the reflection of the triple point on a plane of symmetry was studied. The conditions simulated a stoichiometric methane-oxygen detonation cell at low pressure on time scales preceding ignition, when the gas was assumed to be inert. Viscosity was found to play an important role on some shock reflection mechanisms believed to accelerate reaction rates in detonations when time scales are small. A small wall jet was present in the double Mach reflection and increased in size with Reynolds number, eventually forming a small vortex. Kelvin-Helmholtz instabilities were absent and there was no Mach stem bifurcation at Reynolds numbers corresponding to when the Mach stem had travelled distances on the scale of the induction length. Kelvin-Helmholtz instabilities are found to not likely be a source of rapid reactions in detonations at time scales commensurate with the ignition delay behind the Mach stem.

Keywords Viscosity · Shock wave · Reflection

S.SM. Lau-Chapdelaine
E-mail: –

M.I. Radulescu
E-mail: –

University of Ottawa,
Department of Mechanical Engineering,
161 Louis Pasteur, Ottawa, Canada, K1N 6N5

The final publication is available at Springer via `http://dx.doi.org/10.1007/s00193-016-0674-8` including electronic supplementary material.

1 Introduction

The problem of shock reflections is of importance to unsteady gas dynamics, including the study of detonation waves. When a shock wave reflects from a solid surface or a plane of symmetry, it usually adopts one of two forms: a regular reflection or a Mach reflection, illustrated in Fig. 1. Thorough reviews of shock reflection have been written by Hornung [1] and Ben-Dor [2].

The Mach reflection is generally comprised of three shocks: the Mach (Mach stem), incident, and reflected (transverse) shocks, illustrated in Fig. 1(b). The Mach stem and incident shock compose the leading shock front and are joined at a kink called the triple point. The reflected wave emanates from the triple point and travels transversely behind the incident shock. A contact surface (sometimes called a slip line, or shear layer) separates gas shocked by the Mach stem from the gas shocked by the incident and reflected shock waves. The configuration of these discontinuities is determined by the incident shock (or Mach stem) strength, the angle between the incident and Mach shocks, and the isentropic exponent of the gas.

Mach reflections are a natural part of the unstable (cellular) structure of detonations whose fronts have counter-travelling triple points, as seen experimentally in Fig. 2; five successive photos have been pasted in place, meaning some details of each frame are covered by the preceding one. A detonation wave is shown travelling from left to right. The first two frames show a pair of triple points and their transverse shocks travelling towards each other, one from the bottom and the other from the top. The shocks then reflect off each other, forming a pair of triple points which move apart as seen in the next three frames. The path of the triple points

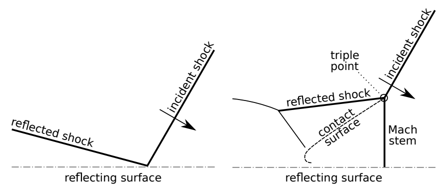

(a) Regular reflection (b) Mach reflection

Fig. 1 An incident shock that travels towards an oblique surface (direction of arrow) such as a wall or plane of symmetry, reflects and generally adopts one of two types of configuration: a regular reflection or a Mach (irregular) reflection

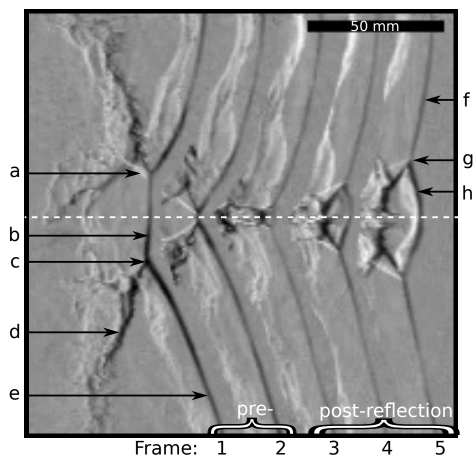

Fig. 2 Superimposed schlieren photographs (cropped, with grain extraction and stretched contrast) of two triple points colliding in a detonation, adapted from Bhattacharjee [8] (CH_4+$2O_2$, $\hat{p}_0 = 3.5$ kPa, $\hat{T}_0 = 300$ K, $\Delta\hat{t} = 11.53$ μs), dark features show a decrease in density and bright features show an increase from left to right, dotted line represents the axis of symmetry, a) reflected (transverse) shock, b) pre-reflection incident shock, c) triple point, d) contact surface, e) pre-reflection Mach stem, f) post-reflection incident shock, g) triple point, h) post-reflection Mach stem

over time form the cellular structure, whose dynamics have been well studied in the past [3–7].

Numerous studies have examined these shock reflections, seeking insight on the phenomena responsible for the creation of locally over-driven detonations, or re-initiation in cases of detonation failure. They have come upon a handful of candidates including: adiabatic shock compression, which heats the gas and exponentially reduces induction times [9–13]; jet formation, which may entrain combustion radicals from reacted zones in the rear to the zone behind the Mach stem [8, 12, 14–16], where subsequent mixing with unburnt gases may increase reaction rates; Richtmyer-Meshkov instabilities, which arise from the interaction between pressure waves and density gradients (from reactions), accelerating mixing [8]; and Kelvin-Helmholtz instabilities along shear layers, which may also accelerate mixing [8]. While these studies have been able to capture and study reactive shock reflections and have clarified the importance of certain phenomena over others, much still remains to be clarified.

Experiments have suffered from the disparity of scales associated with the problem. The cellular structure of detonations can measure hundreds of induction lengths, which can be a hundred times longer than the energy deposition zone. The difficulty this causes in measuring the flow field is aggravated by the stochastic nature of detonations. Numerical simulations have suffered from different issues. For example, inviscid numerical simulations of shock reflections have predicted bifurcation of the Mach stem under certain conditions [17, 18], caused by a strong jet and vortex, leading to an acceleration of the Mach stem and creation of new cells, however, this aspect of shock reflection has been absent in experiments. Simulations using the Euler equations do not converge and increasing resolution only causes a rise in non-physical phenomena [19]. The validity of the inviscid flow assumption has come into question recently [20] as mechanisms for turbulent mixing have been suggested to significantly increase reaction rates behind the detonation front.

This study will examine the importance of diffusion on the triple-shock reflection problem for conditions relevant to detonations. This will be done numerically by imposing the ideal three shock solution as the initial conditions of the domain, unique to this work. The triple-shock reflection process in hydrogen detonations have been described in detail [21, 22], but have not considered viscosity. In this case, the effects of viscosity will be resolved down to the shock thickness as done by Ziegler [15]. While the role of turbulence will not be addressed directly, the simulations will offer insight on some turbulence-generating mechanisms such as Kelvin-Helmholtz instabilities and the wall jetting effect. The window of interest will cover the initial shock reflection at the tip of a detonation cell and its subsequent growth before ignition of the gas behind the Mach stem. This study extends previously presented work [23] with the inclusion of heat diffusion and an improved viscous model.

2 Model

The flow is modelled using the compressible Navier-Stokes equations in two dimensions with momentum and heat diffusion

$$\begin{aligned}\frac{\partial\hat{\rho}}{\partial\hat{t}} + \boldsymbol{\nabla}\cdot(\hat{\rho}\hat{\mathbf{u}}) &= 0\\ \frac{\partial(\hat{\rho}\hat{\mathbf{u}})}{\partial\hat{t}} + \boldsymbol{\nabla}\cdot(\hat{\rho}\hat{\mathbf{u}}\hat{\mathbf{u}}) + \boldsymbol{\nabla}\hat{p} - \boldsymbol{\nabla}\cdot\hat{\boldsymbol{\tau}} &= 0\\ \frac{\partial(\hat{\rho}\hat{E})}{\partial\hat{t}} + \boldsymbol{\nabla}\cdot\left((\hat{\rho}\hat{E}+\hat{p})\hat{\mathbf{u}} - \hat{\mathbf{u}}\cdot\hat{\boldsymbol{\tau}} + \hat{\mathbf{q}}\right) &= 0\end{aligned} \qquad (1)$$

where ρ is the density, p is the pressure, u is the velocity, t is time, $\boldsymbol{\tau}$ is the shear stress tensor

$$\hat{\boldsymbol{\tau}} = 2\hat{\mu}\left(\frac{1}{2}\left(\frac{\partial\hat{u}_i}{\partial\hat{x}_j} + \frac{\partial\hat{u}_j}{\partial\hat{x}_i}\right) - \frac{1}{3}\delta_{ij}\boldsymbol{\nabla}\cdot\hat{\mathbf{u}}\right)\mathbf{e}_i\mathbf{e}_j,$$

in Einsteinian notation with viscosity μ. The circumflex accent represents dimensional values. The bulk (second) viscosity is neglected. The total energy E is

$$\hat{E} = \frac{\hat{p}}{\hat{\rho}(\gamma-1)} + \frac{1}{2}\hat{\mathbf{u}}\cdot\hat{\mathbf{u}},$$

with constant isentropic exponent γ for a calorically perfect gas, and $\mathbf{q}$ is the heat conduction

$$\hat{\mathbf{q}} = -\hat{k}\boldsymbol{\nabla}\hat{T}$$

with thermal conductivity k and temperature T. The perfect gas equation of state is

$$\hat{p} = \hat{\rho}\hat{R}\hat{T}$$

with specific gas constant R. Viscosity is modelled using Sutherland's law with a coefficient of zero, and the Prandtl number is held constant so that

$$\hat{\mu} = \frac{\mu_{\mathrm{ref}}}{\sqrt{T_{\mathrm{ref}}}}\sqrt{\hat{T}} \quad \text{and} \quad \hat{k} = \frac{k_{\mathrm{ref}}}{\sqrt{T_{\mathrm{ref}}}}\sqrt{\hat{T}}. \qquad (2)$$

The results will be compared to simulations of the Euler equations, which neglect the diffusive terms $\boldsymbol{\tau}$ and $\mathbf{q}$, but have the same maximal resolution. The solutions to the Euler equations are "inviscid", but are still subject to artificial diffusion from discretization of the equations.

The system of equations is non-dimensionalised by

$$\rho = \frac{\hat{\rho}}{\hat{\rho}_{\mathrm{ref}}},\ p = \frac{\hat{p}}{\hat{p}_{\mathrm{ref}}},\ T = \frac{\hat{T}}{\hat{T}_{\mathrm{ref}}},\ x_i = \frac{\hat{x}_i}{\hat{\lambda}_{\mathrm{ref}}},\ u_i = \frac{\hat{u}_i}{\sqrt{\frac{\hat{p}_{\mathrm{ref}}}{\hat{\rho}_{\mathrm{ref}}}}},$$

$$t = \frac{\hat{t}}{\hat{\lambda}_{\mathrm{ref}}\sqrt{\frac{\hat{\rho}_{\mathrm{ref}}}{\hat{p}_{\mathrm{ref}}}}},\ \mu = \frac{\hat{\mu}}{\sqrt{\hat{\rho}_{\mathrm{ref}}\hat{p}_{\mathrm{ref}}}\hat{\lambda}_{\mathrm{ref}}},\ k = \frac{\hat{k}}{\hat{\rho}_{\mathrm{ref}}\hat{p}_{\mathrm{ref}}^{\frac{3}{2}}\hat{T}_{\mathrm{ref}}^{-1}\hat{\lambda}_{\mathrm{ref}}}.$$

The reference state (subscript ref) is chosen to be the unshocked state with mean free path [24]

$$\hat{\lambda}_{\mathrm{ref}} = \frac{\hat{R}\hat{T}_{\mathrm{ref}}}{\sqrt{2}\pi\hat{d}^2\hat{N}_{\mathrm{A}}\hat{p}_{\mathrm{ref}}}$$

where $\hat{N}_{\mathrm{A}}$ is Avogadro's constant and $\hat{d}$ is the molecular size. The viscosity model (2) at this reference state, along with the omission of the bulk viscosity, which can be quite significant in some gasses [25, 26], underpredicts the viscosity in high temperature regions (*e.g.*, behind the Mach stem). This will likely have little qualitative impact on the results, even strengthening arguments made in the discussion.

The gas is considered chemically frozen since the shock reflection is being examined on time scales less than the induction time, prior to noticeable thermicity.

3 Numerical method

The compressible Navier-Stokes equations (1) in two dimensions were solved using `mg`, a computational package developed by Falle [27, 28]. This was done with a second-order accurate exact Godunov scheme for the convective terms, and diffusive terms were solved explicitly.

A resolution study was performed on an initially ideal one-dimensional shock with Mach number $M = 4.363$ through a quiescent gas with isentropic exponent $\gamma = 1.358$, relating to the experimental strength of the pre-reflection incident shock of Fig. 2 travelling through the unshocked gas. Fig. 3 compares results from the computational package `mg` at $t = 1$ to the steady-state Navier-Stokes shock profile, integrated using first order finite differences (converged at the given resolution). The integration began with a relative deviation of 10^{-9} from the ideal post-shock conditions and shot towards the pre-shock state. The figure shows that the shock thickness is converged at a maximum resolution of approximately 16 grids per mean free path and that $t = 1$ is sufficient for the ideal shock to reach its steady viscous form.

A rectangular domain of size 240 by 180 mean free paths was modelled, totalling in width about one hundredth of the scale bar of Fig. 2. The domain was covered by a Cartesian mesh with 60 by 45 grid points with six additional levels of adaptive mesh-refinement, each doubling the resolution when differences between flow properties exceeded a tolerance of 0.01 between levels. The bottom wall used a symmetry boundary condition while the remainder were set to have zero normal gradients; all were parallel to the mesh. The triple point was positioned at the origin, equidistant from the left

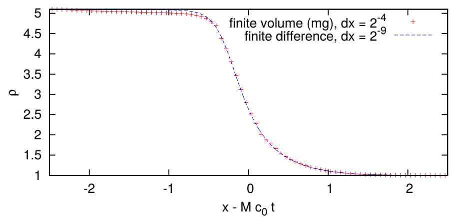

Fig. 3 One-dimensional Navier-Stokes shock profile of density shows that the shock thickness is nearly converged at $t = 1$ and a resolution of 16 grids per mean free path

Table 1 Initial conditions, zones refer to Fig. 4

	Unshocked (zone 0)	Incident (zone 1)	Reflected (zone 2)	Mach (zone 3)
p	1	21.7767	41.0169	41.0169
ρ	1	5.08848	8.05256	5.69144
u	-5.08513	-0.999342	-1.71771	-0.562407
v	0	0	-0.93582	-3.5399

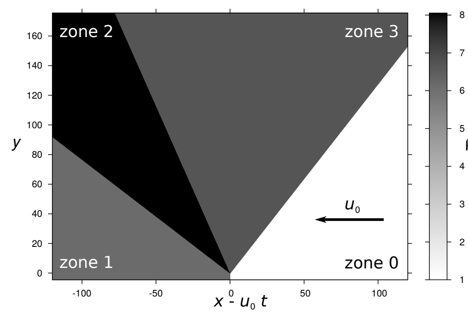

Fig. 4 Density plot of initial conditions

and right boundaries and 4.5 mean free paths above the reflecting surface (bottom wall) to let the viscous shock structure fully develop prior to reflection. This means the reflection occurs $t = 1.047$ after initiation. The domain was sized in the y-direction to allow enough room for the reflection to grow to the desired size before boundary error reached the reflected triple point. Results at larger times were obtained using a larger domain at the same resolution, with the right boundary extending further from the origin than the left boundary.

Past numerical shock reflection studies have usually considered the interaction of a single shock front with a reflecting wedge, however, the reflection of a triple point from a symmetry boundary has been modelled instead. This better reproduces the geometry of cell collision and removes certain numerical difficulties associated with the creation of reflection boundaries in Cartesian grids [29,30] and reduces early-reflection artifacts, which can affect the reflection at later times [30,31].

Conditions approximating the second frame of Fig. 2 (top triple point) were initially imposed onto the domain. These correspond to the experimental results of a detonation passing through stoichiometric methane-oxygen performed by Bhattacharjee [8]. The initial conditions were calculated using the ideal three-shock solution [1,2] with an incident shock of strength $M = 4.363$ normal to the reflecting boundary and an angle of 141.95° between the incident and Mach shocks. The triple point's frame of reference in the x-direction was used, with the unshocked gas travelling at a velocity $u_0 = 5.085$ to the left, reducing the required domain size. A constant isentropic exponent $\gamma = 1.358$ was assumed, corresponding to the unshocked conditions of stoichiometric methane-oxygen at 300 K and 3.5 kPa. The length scale under these conditions $\hat{\lambda}_{\text{ref}} \approx 2.02 \times 10^{-6}$ m is calculated using $\hat{d} = 3.63 \times 10^{-10}$ m as the mole-averaged molecular size for a stoichiometric mixture of methane [32] and oxygen [33]. The initial conditions are tabulated in table 1, and shown in Fig. 4.

The reflected triple shock can also be predicted using three shock theory, by keeping the isentropic exponent and angle between the incident and Mach shocks constant, but imposing the pre-reflection Mach stem strength as the post-reflection incident shock strength. The ideal triple shocks and their reflections referred to in this text are calculated assuming a constant isentropic exponent. The transport properties behind the various shocks are then estimated using a chemical kinetics code, Cantera [34] with the GRI-3.0 mechanism [35], assuming no change in chemical composition.

4 Results

The triple-shock reflection is illustrated and labelled in Fig. 5. The triple point initially travels along the trajectory denoted by the red dashed line until it reaches the reflection point. The shock wave known as the pre-reflection Mach stem then continues as the post-reflection incident shock on the right side and forms a new Mach stem as it interacts with the reflecting surface as a double Mach reflection. The pre-reflection transverse shock also interacts with the surface and forms a regular reflection on the left side. The prefixes "pre-reflection" and "post-reflection" when used will distinguish whether the features being referred to are those before or after, respectively, the triple point has reached the reflection point as they otherwise may share the same name (*e.g.*, the pre-reflection incident shock refers to the vertical feature in the "pre-reflection" box of figure 5).

This is observed in the simulation results of Fig. 6 and as electronic supplementary material (Online Resources 1 and 2 for the viscous and inviscid videos, respectively, with frame rate $\varDelta t = 1$). The density profile of the viscous reflection in Fig. 6(a) is shown at the approximate induction time of gas behind the post-reflection Mach stem ($t = 17$), approximated assuming a constant volume combustion with the ideal post-reflection Mach state as initial conditions, computed using Cantera [34] and the GRI 3.0 mechanism [35]. The double Mach reflection formed on the right is seen at $x - u_0 t \approx 75$, and the regular reflection formed on the left is seen at $x - u_0 t \approx -100$. The key features of the Mach reflection will be reviewed first, followed by those of the regular reflection.

4.1 Mach Reflection

A double Mach reflection propagating through the unshocked gas arises from the reflection of the pre-reflection Mach stem (now considered the incident shock) with the bottom wall. The triple point follows a trajectory of $5.92° \pm 0.10°$ above the horizontal in the lab frame of reference (calculated every $\varDelta t = 1$ in the range $8 \leq t \leq 17$), which is below the inviscid simulation's $6.32° \pm 0.04°$.

There is little evidence of Kelvin-Helmholtz instabilities along the contact surface behind the Mach stem in the inviscid case (Fig. 6(b)), and none in the viscous case (Fig. 6(a)). The contact surface jets towards the Mach stem along the reflecting wall, but this wall jet does not reach the Mach stem in the viscous simulation. A close-up of the Mach stem's temperature profiles in Fig. 6(c) and 6(d) shows that the removal of viscous terms has the wall jet curl into a vortex as the jet reaches the Mach stem, causing it to bulge, but remaining unbifurcated [17].

The temperature profiles near the Mach reflection show that the hottest regions are found behind the Mach stem, especially at its foot. The vortex behind the Mach stem, present only in the inviscid simulation, is composed mostly of cool gas near the temperature of the gas shocked by the reflected wave.

When the simulation time is extended to the ignition time behind the post-reflection transverse shock, shown in Fig. 6(e) at $t = 120$, a comparison of the viscous solution with the earlier time shows that temperature in the centre of the wall jet decreased, while the temperature behind the Mach stem slightly increased, and a vortex began to form at the end of the wall jet. The shock that joins the contact surface and transverse wave (making this a double Mach reflection) has become sharper and its triple point, the kink along the transverse wave, has become much more distinguished. The inviscid solution (Fig. 6(e)) develops Kelvin-Helmholtz instabilities along the contact surface which grow through to the wall jet. Mach stem bulging is reduced, relative to the Mach stem height.

4.2 Regular reflection

The regular reflection seen on the left of Fig. 6(a) is caused by the reflection of the pre-reflection transverse wave on the plane of symmetry into zone 1 (Fig. 4).

The regular and Mach reflections are joined at the pre-reflection contact surface where the reflected wave of the regular reflection curves across the contact surface and joins the oblique shock emanating from the Mach reflection's transverse wave. The contact surface is deflected after being shocked, curls along the wall, and jets backwards to the regular reflection.

Very prominent Kelvin-Helmholtz instabilities are present along the pre-reflection contact surface in the inviscid case (6(b)) and also manifest themselves in the wall jet, but they remain absent in the viscous case. The jet is also slightly longer in the inviscid case, with marginally higher pressures (not shown) at its head, but the viscous and inviscid cases are otherwise similar.

5 Discussion

While the regular reflection includes interesting features, such as the interaction between a contact surface and a shock, and its own wall jet, the discussion will focus on the Mach reflection where there are features believed to be of interest to detonation propagation.

One notable difference between the inviscid and viscous case is the curvature of the Mach stem, contact surface, and transverse shock in the vicinity of the triple point shown in Fig. 7 with a length scale greater than the shock thickness. A high pressure point is present behind the transverse shock in Fig. 7(a) but differences in density (Fig. 7(b)) and temperature are more subtle. Away from the triple point, the orientation of the reflected shock and contact surface differ from the inviscid case by a few degrees. The curvature and pressure concentration near the triple point persist later in time.

The angle of the viscous triple point trajectory lies above the three shock theory prediction of $5.36°$ and eventually increases to become larger than that of the

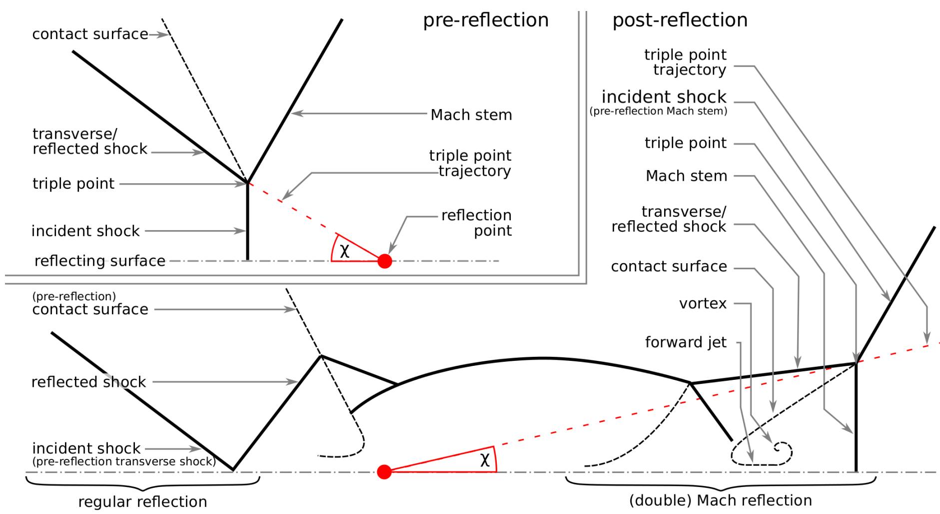

Fig. 5 Illustration of the three shock structure before and after reflection

inviscid simulation later in time. The trajectory measured from the experiment in the third frame of Fig. 2 is 7.85°, however the gas behind the Mach stem in the experiment is likely already reacted so it does not offer a good comparison.

Following the contact surface away from the triple point, the Kelvin-Helmholtz instabilities, postulated to increase reaction rates in detonations [8, 16], are absent at the induction time ($t \approx 17$). Traces of Kelvin-Helmholtz instabilities remain absent later into the simulation ($t \approx 120$), but appear in the inviscid simulation with regions of slightly increased temperature.

Rikanati *et al.* [36, 37] measured shear layer growth rates in shock reflection experiments and found that these growth rates agreed with previous measurements for turbulent shear layers only above a Reynolds number of Re $\gtrsim 2\times10^4$. They associated this critical Reynolds number with the transition to turbulence in Kelvin-Helmholtz instabilities, where the instabilities begin to play an important role in contact surface thickness. They defined the Reynolds number as

$$\mathrm{Re} = \frac{U_{\mathrm{shear}} h_{\mathrm{M}}}{\nu_{\mathrm{c.s.}}}$$

where U_{shear} is the velocity difference across the contact surface, $\nu_{\mathrm{c.s.}}$ is the average dynamic viscosity across the contact surface, and h_{M} is the height of the Mach stem. The ideal triple-point reflection can be used to approximate the values of Reynolds number, with the Mach stem height calculated as

$$h_{\mathrm{M}} = \tan(\chi) M_{\mathrm{M}} c_0 t_{\mathrm{post}}$$

where χ is the angle between the triple-point trajectory and the horizontal (in the lab frame of reference), M_{M} is the post-reflection Mach stem strength, and t_{post} is the time since reflection. This gives Reynolds numbers of Re ≈ 100 at $t = 17$, when ignition is expected behind the Mach stem, and Re ≈ 800 at $t = 120$ for ignition behind the transverse shock. This is two orders of magnitude smaller than the critical Reynolds number necessary for Kelvin-Helmholtz instabilities to contribute to contact surface thickness.

This estimation is extended to stoichiometric detonations under atmospheric conditions in table 2, which lists the Reynolds numbers when ignition occurs behind the Mach stem, when Kelvin-Helmholtz instabilities become important [36,37], and at the maximal cell width. The ignition Reynolds numbers were calculated for pre-reflection incident wave strengths of 70% [8] of the ideal one-dimensional steady state (Chapman-Jouguet) velocity at the end of the detonation cell, using the Shock & Detonation Toolbox [38] for Cantera [34] with the GRI 3.0 mechanism [35]. Angles between the incident and Mach shocks were implied by soot foil records of ethyne (acetylene) and hydrogen detonations at sub-atmospheric pressures [5,39], which showed triple-point trajectories of $\chi \approx 35° \pm 5°$ before reflection. This is comparable to the methane experiment presented in

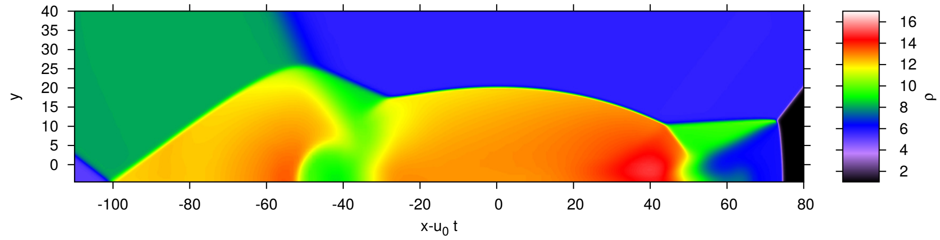

(a) Density, viscous, Re ≈ 100, $t = 17$

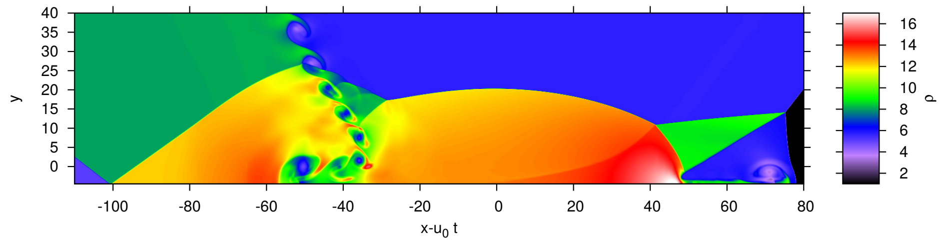

(b) Density, inviscid, $t = 17$

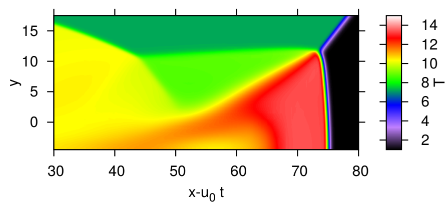

(c) Temperature, viscous, Re ≈ 100, $t = 17$

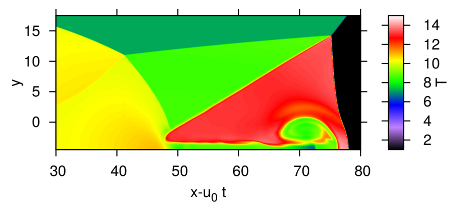

(d) Temperature, inviscid, $t = 17$

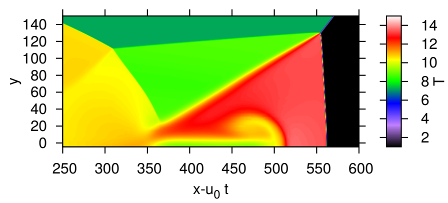

(e) Temperature, viscous, Re ≈ 800, $t = 120$

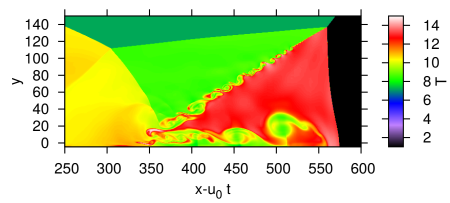

(f) Temperature, inviscid, $t = 120$

Fig. 6 Simulations results cropped to areas of interest for density ρ and temperature T; ranges kept consistent for comparison

Fig. 2 where $\chi \approx 43°$. The cellular Reynolds numbers were calculated using the half-cell size as the Mach stem height, approximated from Shepherd's detonation database [40–45].

The table suggests that Kelvin-Helmholtz instabilities will not appear before auto-ignition of the gas behind the Mach stem since $\mathrm{Re}_{\mathrm{KH}} \gg \mathrm{Re}_{\mathrm{ign}}$. Instabilities may arise before ignition of gas shocked by the transverse wave in methane or hydrogen reflections, as ignition there is an order of magnitude slower, and they will most likely appear within the life time of the cell because $\mathrm{Re}_{\mathrm{cell}} \gg \mathrm{Re}_{\mathrm{KH}}$.

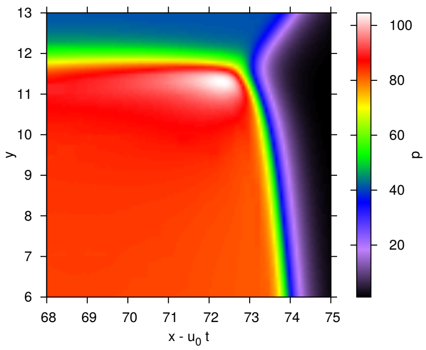

(a) Pressure

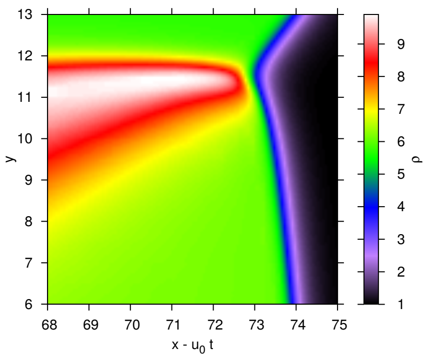

(b) Density

Fig. 7 Curvature of shocks in vicinity of triple point, viscous, Re ≈ 110, $t = 17$

Table 2 Reynolds numbers at ignition behind the Mach stem, at the critical value for Kelvin-Helmholtz instabilities, and for the cell size; stoichiometric atmospheric detonations ($\hat{T}_{\mathrm{ref}} = 300$ K, $\hat{p}_{\mathrm{ref}} = 100$ kPa, $3.72\ \frac{\mathrm{mol\ N_2}}{\mathrm{mol\ O_2}}$) of select fuels with pre-reflection incident shock Mach numbers $M_{\mathrm{I,pre}} = 70\% M_{\mathrm{CJ}}$ and pre-reflection triple-point trajectories χ

	$\mathrm{Re}_{\mathrm{ign}}$		$\mathrm{Re}_{\mathrm{KH}}$	$\mathrm{Re}_{\mathrm{cell}}$	
χ	40°	30°		40°	30°
CH_4	170	3700	2×10^4	1×10^7	6×10^6
C_2H_2	170	1300		5×10^5	3×10^5
C_3H_8	320	1200		4×10^6	2×10^6
H_2	350	3400		2×10^5	9×10^4

Massa *et al.* [46] performed simulations and a linear stability analysis of the contact surface and found that Kelvin-Helmholtz instabilities were attenuated by reactions (at low activation energy, not necessarily the case for stoichiometric methane-oxygen) and found diffusion to be important. This suggests instability growth will be delayed if ignition occurs before they become well established, but only momentarily until larger scales are reached as evidenced by the instabilities seen along the contact surfaces in frame 1 of Fig. 2.

It is therefore unlikely that Kelvin-Helmholtz instabilities play a role in the propagation of detonation waves at times commensurate with the ignition time of gas behind the Mach stem, however they are likely to appear at scales on the order of the cell size where they may accelerate reactions. These instabilities may also be important in problems such as detonation reinitiation where the shocks are much weaker and induction time is longer.

The contact surface curves towards the Mach stem as it approaches the wall, caused by flow stagnation perpendicular to the reflecting surface [29, 47, 48]. The stagnation pressure to the left of the jet (not shown) increases with the Reynolds number as viscous losses along the contact surface become less significant. This is accompanied by the development of a vortex, which may help with mixing, but the wall jet has grown little and not caused the Mach stem to bulge. The jet and vortex remain much weaker than their inviscid counterparts. Temperature in the wall jet drops along the contact surface, possibly reducing the effect of combustion radicals, while the temperature behind the Mach stem increases, decreasing ignition time late in the reflection process. Heating of the contact surface [23] does not occur due to the inclusion of heat diffusion in the model.

The use of a better model for viscosity, including the bulk viscosity for example, would lower the simulation's Reynolds number, despite the difference of Mach stem height with three shock theory, and amplify differences between the viscous and inviscid cases.

The Mach reflection begins to adopt the features of the inviscid case (of earlier times) as the Reynolds number increases, which highlights the importance of including viscosity in the simulation of time-limited processes such as detonation.

6 Conclusion

The reflection of the triple-shock configuration was studied numerically in two dimensions using the Navier-Stokes equations under conditions similar to those present in the creation of detonation cells. The reflection of a triple point on a plane of symmetry creates a double Mach reflection, from the reflection of the incident Mach stem, and a backwards-facing regular reflection occurs from the reflection of the transverse shock.

When viscosity was considered, no Kelvin-Helmholtz instabilities were seen and there was no bifurcation of the Mach stem for Reynolds numbers corresponding to the ignition time behind the Mach stem and transverse shock. However, a small wall jet was present, which increased with Reynolds number and eventually formed a small vortex. Kelvin-Helmholtz instabilities are unlikely to be a source of rapid reactions at early times in detonation propagation. Further study is required on longer time scales, including those associated with the cell size.

This study shows that viscosity has an important role on some shock reflection mechanisms believed to accelerate reaction rates in detonations. Diffusion must be considered when the time scales are small, and the Euler equations are inadequate in this regard.

Acknowledgements This work was sponsored by a Natural Sciences and Engineering Research Council of Canada (NSERC) Discovery grant to M. I. Radulescu and a NSERC Alexander Graham Bell Canadian Graduate Scholarship to S. S.M. Lau-Chapdelaine. The authors wish to acknowledge Gary Sharpe for useful discussions.

References

1. Hornung, H.: Regular and Mach reflection of shock waves. Ann. Rev. Fluid Mech. **18** (1986) 33–58
2. Ben-Dor, G.: Shock Wave Reflection Phenomena. Springer (2007)
3. Subbotin, V.: Collision of transverse detonation waves in gases. Combust. Explo. Shock+ **11**(3) (1975) 411–414
4. Gamezo, V.N., Desbordes, D., Oran, E.S.: Formation and evolution of two-dimensional cellular detonations. Combust. Flame **116**(1) (1999) 154–165
5. Austin, J.M.: The role of instability in gaseous detonation. Ph.D. thesis, California Institute of Technology (2003)
6. Strehlow, R.A.: Detonation structure and gross properties. Combust. Sci. Technol. **4**(1) (1971) 65–71
7. Radulescu, M., Sharpe, G., Lee, J., Kiyanda, C., Higgins, A., Hanson, R.: The ignition mechanism in irregular structure gaseous detonations. P. Combust. Inst. **30**(2) (2005) 1859–1867
8. Bhattacharjee, R.R.: Experimental Investigation of Detonation Re-initiation Mechanisms Following a Mach Reflection of a Quenched Detonation. Master's thesis, University of Ottawa (2013)
9. Teodorczyk, A.: Fast deflagrations and detonations in obstacle-filled channels. J. Power Technol. **79** (1995)
10. Ohyagi, S., Obara, T., Hoshi, S., Cai, P., Yoshihashi, T.: Diffraction and re-initiation of detonations behind a backward-facing step. Shock Waves **12**(3) (2002) 221–226
11. Obara, T., Sentanuhady, J., Tsukada, Y., Ohyagi, S.: Reinitiation process of detonation wave behind a slit-plate. Shock Waves **18**(2) (2008) 117–127
12. Lau-Chapdelaine, S.: Numerical Simulations of Detonation Re-initiation Behind an Obstacle. Master's thesis, University of Ottawa (2013)
13. Lv, Y., Ihme, M.: Computational analysis of re-ignition and re-initiation mechanisms of quenched detonation waves behind a backward facing step. P. Combust. Inst. **35**(2) (2015) 1963–1972
14. Sorin, R., Zitoun, R., Khasainov, B., Desbordes, D.: Detonation diffraction through different geometries. Shock Waves **19**(1) (2009) 11–23
15. Ziegler, J.L.: Simulations of compressible, diffusive, reactive flows with detailed chemistry using a high-order hybrid WENO-CD scheme. Ph.D. thesis, California Institute of Technology (2012)
16. Maley, L., Bhattacharjee, R., Lau-Chapdelaine, S.M., Radulescu, M.I.: Influence of hydrodynamic instabilities on the propagation mechanism of fast flames. P. Combust. Inst. **35**(2) (2015) 2117–2126
17. Mach, P., Radulescu, M.: Mach reflection bifurcations as a mechanism of cell multiplication in gaseous detonations. P. Combust. Inst. **33**(2) (2011) 2279–2285
18. Glaz, H., Colella, P., Glass, I., Deschambault, R.: A detailed numerical, graphical, and experimental study of oblique shock wave reflections. Technical Report LBL-20033, Lawrence Berkeley National Laboratory (1985)
19. Sun, M., Takayama, K.: A note on numerical simulation of vortical structures in shock diffraction. Shock Waves **13**(1) (2003) 25–32
20. Radulescu, M.I., Sharpe, G.J., Law, C.K., Lee, J.H.: The hydrodynamic structure of unstable cellular detonations. J. Fluid Mech. **580** (2007) 31–81
21. Sharpe, G.J.: Transverse waves in numerical simulations of cellular detonations. J. Fluid Mech. **447** (2001) 31–51
22. Hu, X., Zhang, D., Khoo, B., Jiang, Z.: The structure and evolution of a two-dimensional $H_2/O_2/Ar$ cellular detonation. Shock Waves **14**(1-2) (2005) 37–44
23. Lau-Chapdelaine, S.S.M., Sharpe, G., Radulescu, M.I.: Viscous Solutions of the Triple Shock Reflection Problem. In: 25th ICDERS, Leeds UK (2015)
24. Vincenti, W.G., Kruger, C.H.: Introduction to Physical Gas Dynamics. Krieger Publishing Company, Malabar, Florida (1965)
25. Thompson, P.: Compressible-Fluid Dynamics. 3 edn. Rensselaer Polytechnic Institute (1988)
26. Cramer, M.: Numerical estimates for the bulk viscosity of ideal gases. Phys. Fluids **24**(6) (2012)
27. Falle, S.: Self-similar jets. Mon. Not. R. Astron. Soc. **250**(3) (1991) 581–596
28. Falle, S., Komissarov, S.: An upwind numerical scheme for relativistic hydrodynamics with a general equation of state. Mon. Not. R. Astron. Soc. **278**(2) (1996) 586–602
29. Mach, P.: Bifurcating Mach Shock Reflections with Application to Detonation Structure. Master's thesis, University of Ottawa (2011)
30. Lau-Chapdelaine, S.M., Radulescu, M.I.: Non-uniqueness of solutions in asymptotically self-similar shock reflections. Shock Waves **23**(6) (2013) 595–602
31. Previtali, F.A., Timofeev, E., Kleine, H.: On unsteady shock wave reflections from wedges with straight and concave tips. In: 45th AIAA Fluid Dyn. Conf. (2015)
32. Flynn, L.W., Thodos, G.: Lennard-Jones force constants from viscosity data: Their relationship to critical properties. AIChE J. **8**(3) (1962) 362–365

33. Hirschfelder, J.O., Curtis, C.F., Bird, R.B.: Molecular Theory of Gases and Liquids. Wiley New York (1954)
34. Goodwin, D.G., Moffat, H.K., Speth, R.L.: Cantera: An Object-oriented Software Toolkit for Chemical Kinetics, Thermodynamics, and Transport Processes. (2016) Version 2.2.1.
35. Smith, G.P., Golden, D.M., Frenklach, M., Moriarty, N.W., Eiteneer, B., Goldenberg, M., Bowman, C.T., Hanson, R.K., Song, S., Gardiner, Jr., W.C., Lissianski, V.V., Qin, Z.: GRI 3.0 Mechanism. Gas Research Institute (1999)
36. Rikanati, A., Sadot, O., Ben-Dor, G., Shvarts, D., Kuribayashi, T., Takayama, K.: Shock-wave mach-reflection slip-stream instability: a secondary small-scale turbulent mixing phenomenon. Phys. Rev. Lett. **96**(17) (2006) 174503
37. Rikanati, A., Sadot, O., Ben-Dor, G., Shvarts, D., Kuribayashi, T., Takayama, K.: A secondary small-scale turbulent mixing phenomenon induced by shock-wave Mach-reflection slip-stream instability. In: Shock Waves. Volume 2 of 26th., Springer (2009) 1347–1352
38. Browne, S., Ziegler, J., Shepherd, J.: Numerical Solution Methods for Shock and Detonation Jump Conditions. GALCIT Report FM2006.006, California Institute of Technology (2015)
39. Strehlow, R.A., Biller, J.R.: On the strength of transverse waves in gaseous detonations. Combust. Flame **13**(6) (1969) 577–582
40. Kaneshige, M., Shepherd, J.: Detonation database. GALCIT Technical Report FM97-8 (July 1997)
41. Moen, I., Funk, J., Ward, S., Rude, G., Thibault, P.: Detonation length scales for fuel-air explosives. Prog. Astronaut. Aeronaut. **94** (1984) 55–79
42. Knystautas, R., Guirao, C., Lee, J., Sulmistras, A.: Measurement of cell size in hydrocarbon-air mixtures and predictions of critical tube diameter, critical initiation energy, and detonability limits. Prog. Astronaut. Aeronaut. **94** (1984) 23–37
43. Beeson, H., McClenagan, R., Bishop, C., Benz, F., Pitzl, W., Westbrook, C., Lee, J.: Detonability of hydrocarbon fuels in air. Prog. Astronaut. Aeronaut. **133** (1991) 19–36
44. Bull, D., Elsworth, J., Shuff, P., Metcalfe, E.: Detonation cell structures in fuel/air mixtures. Combust. Flame **45** (1982) 7–22
45. Stamps, D.W., Tieszen, S.R.: The influence of initial pressure and temperature on hydrogen-air-diluent detonations. Combust. Flame **83**(3) (1991) 353–364
46. Massa, L., Austin, J., Jackson, T.: Triple-point shear layers in gaseous detonation waves. J. Fluid Mech. **586** (2007) 205–248
47. Li, H., Ben-Dor, G.: Reconsideration of pseudo-steady shock wave reflections and the transition criteria between them. Shock Waves **5**(1-2) (1995) 59–73
48. Li, H., Ben-Dor, G.: Analysis of double-Mach-reflection wave configurations with convexly curved Mach stems. Shock Waves **9**(5) (1999) 319–326

1.10 Jetting and Mach stem bifurcation in shock reflections: experiments and Navier-Stokes simulations

Authors: S. SM. Lau-Chapdelaine, Q. Xiao, and M. I. Radulescu.

Status: This paper was submitted for peer-review on December 28, 2018. Reviews were received on 23 February, 2019. A revised version of the paper is presented below. The paper is under review as of the submission of this thesis.

This study extends the previous study of viscous triple shock reflections to investigate forward jetting. Viscous simulations on small scales are performed to see if the strong forward jets which lead to bifurcation in inviscid simulations are just an artefact of the Euler equations or a possible phenomenon. A new experiment has been devised to create a free-slip reflection boundary which can be compared with numerical simulations and detonations. It is a continuation of the work presented at the 31st International Symposium on Shock Waves in Nagoya, Japan in 2017.

Coauthor contributions: This paper was co-authored with PhD student Qiang Xiao whose help running the experiments in the lab was invaluable. Xiao was responsible for ensuring experiments were conducted efficiently, safely, and to a high standard.

Viscous jetting and Mach stem bifurcation in shock reflections: experiments and simulations

S. SM. Lau-Chapdelaine†, Q. Xiao and M. I. Radulescu

Department of Mechanical Engineering, University of Ottawa, 161 Louis Pasteur, Ottawa, Ontario, K1N 6N5, Canada

(Received xx; revised xx; accepted xx)

Shock reflection experiments are performed from a plane of symmetry to study the forward jetting and Mach stem bifurcation phenomena. Experiments are performed at a wedge angle of 30° with incident shock Mach numbers up to 4, in N_2, $0.8C_3H_8 + 0.2O_2$, and normal-C_6H_{14}, with isentropic exponents of 1.4, 1.15, and 1.06, respectively. The experiments are complimented by shock-resolved simulations of the Navier-Stokes equations and inviscid simulations. Mach stem bifurcations are found in experiments, viscous and inviscid simulations. Viscosity is found to have a retarding effect on Mach stem bifurcation and the viscous simulations converge to their inviscid counterparts qualitatively. The limits of Mach stem bifurcation are plotted in phase space of Mach number, reflection angle, and isentropic exponent. A maximum isentropic exponent is found beyond which bifurcation does not occur. This limit matches the boundary between irregular/regular detonation cellular structure very well. Experiments also reveal shock and flow field instability at high Mach number and low isentropic exponent.

Key words: Authors should not enter keywords on the manuscript, as these must be chosen by the author during the online submission process and will then be added during the typesetting process (see http://journals.cambridge.org/data/relatedlink/jfm-keywords.pdf for the full list)

1. Introduction

When a shock wave collides with a reflecting surface at a low angle, a Mach reflection occurs, as shown in figure 1. The type of shock reflection depends on three parameters: the Mach number M, angle of reflection (i.e. wedge angle θ_w), and the isentropic exponent (heat capacity ratio) γ. Classifications of shock reflection types are presented in the works of Ben-Dor (2007); Vasilev *et al.* (2008); Semenov *et al.* (2012) and thorough reviews on shock reflections have been written by Hornung (1986) and Ben-Dor (2007).

The forward jet illustrated in figure 1 is poorly understood and studied. As the isentropic exponent is lowered or the Mach number is increased (Mach (2011)), the forward jet approaches the Mach stem, eventually causing it to bulge, kink, or even bifurcate – meaning a new triple point is formed on the Mach stem. Behind the Mach stem, the jet can roll up into a large vortex.

The parameters that lead to the forward jet interacting with the shock front (low γ,

† Email address for correspondence: –

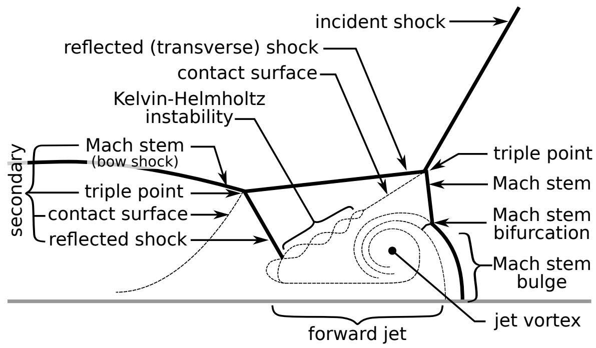

Figure 1: Illustration of a double Mach reflection with Mach stem bifurcation

high M) are relevant to hydrocarbon detonations. Understanding the effects of the forward jet on the flow field behind the Mach stem, and the shock front itself, is important to understanding the propagation and multidimensional instability of detonations. Forward jetting (Sorin *et al.* (2009)), the jet vortex, and Mach stem bifurcation (Radulescu *et al.* (2009)) are believed to accelerate reaction rates and create new detonation cells.

There is conflicting evidence on the prominence of the jet and vortex, or the conditions under which they affect the shape of the shock front. Comparisons of experiments and inviscid simulations (Glaz *et al.* (1985*a*,*b*)) have found that the Mach stem bulges more in simulations than experiments. Bulging of the Mach stem grows to be severe enough to cause Mach stem bifurcation in inviscid simulations (*e.g.* Mach (2011)) but have not been observed in experiments, with a few exceptions (Semenov *et al.* (2009); Maley *et al.* (2015); Mach & Radulescu (2011)). Kelvin-Helmholtz instabilities in shock reflection experiments (*e.g.* Rikanati *et al.* (2006)) are more tame than those found in inviscid simulations with fine resolutions or high-accuracy solvers (*e.g.* Shi *et al.* (2003)); these instabilities can feed into the forward jet and disrupt the flow field. There is a question to what extent viscosity controls the amount of jetting, the size of the vortex, and their effect on the shock front.

The Euler equations that are used to model shock reflections have problems reproducing the forward jet and vortex in shock reflections. The fundamental issue is that the Euler equations do not converge in multi-dimensional cases featuring contact surfaces (Samtaney & Pullin (1996)). The shock reflection and forward jet behave differently depending on the numerical scheme and grid layout (Quirk (1992); Lau-Chapdelaine & Radulescu (2013)), which differ in how artificial diffusion is introduced. The shortcomings of the Euler equations are overcome by use of the Navier-Stokes equations in this study. This will allow the importance of viscosity on the forward jet, the vortex, and Mach stem to be addressed.

Implementation of the reflecting surface also poses problems. In simulations with rectangular coordinates, solid surfaces oblique to the grid alter the reflection configuration depending on how they are implemented (Ben-Dor *et al.* (1987); Lau-Chapdelaine & Radulescu (2013)). This problem will be avoided by following the work of Lau-Chapdelaine & Radulescu (2016) who used the three shock solution as initial conditions and a grid-aligned reflecting surface.

Boundary layers on the reflecting surface change the effective wedge angle (Hornung (1985); Ben-Dor (2007)) and cause the forward jet to oscillate Vasilev *et al.* (2004); Shi *et al.* (2017). While most simulations use free-slip boundaries, the few experiments

(Smith (1959); Henderson & Lozzi (1975); Higashino *et al.* (1991); Barbosa & Skews (2002)) performed with free-slip surfaces, by using planes of symmetry, were focused on the transition from regular to irregular reflection. Shock reflections in detonations happen on a symmetry boundary, where boundary layers are absent, and there is a need for experiments to explore forward jetting and bifurcation under these conditions.

In this study, well posed experiments and simulations are used to explore the conditions under which the forward jet approaches and disturbs the shock front. The effects of viscosity, Mach number, and isentropic exponent on the forward jet and the front are scrutinized. Conditions where jet-shock interaction become important are determined and their boundaries are reported. This is done through experiments of shock reflection from a plane of symmetry, shock-resolved Navier-Stokes simulations, and inviscid simulations.

The experiments are addressed in section 2 followed by numerical simulations in section 3. The discussion is found in section 4 and the conclusion in section 5.

2. Experiments

2.1. *Experimental technique*

Experiments were carried out in a detonation-driven aluminum shock tube illustrated in figure 2 and described by Maley (2015). The shock tube measured 3.48 m in length and had a rectangular cross-section measuring 20.32 cm tall by 1.91 cm in depth. A diaphragm separated the driver and test sections, placed at the first third or second third of the tube.

The shock tube was evacuated to pressure $\lesssim 80$ Pa before gases were introduced. The driver section was filled with a stoichiometric ethylene-oxygen mixture ($C_2H_4 + 3O_2$). The test section was filled with a gas selected for its isentropic exponent, listed in table 1. Nitrogen was used for $\gamma_0 = 1.4$, an inert rich-propane-oxygen mixture ($0.8C_3H_8 + 0.2O_2$) for $\gamma_0 = 1.15$, and normal hexane for $\gamma_0 = 1.06$.

Experiments were initiated by a spark to ignite the driver gas. A mesh of obstacles in the first third of the shock tube promoted detonation initiation in the driver section. The detonation ruptured the diaphragm, transmitting a shock into the test section.

The diaphragm was composed of aluminum foil covered by aluminum tape on the test gas side. An '`I`' shaped slot matching the channel dimensions was cut through the tape. The foil separated the driver and test gases and opened along the slot in the tape when hit by the driving detonation. The tape kept the foil in place during opening, preventing diaphragm petals from polluting the test section with large fragments, though small fragments still form. Experiment 10 used a plastic sheet as a diaphragm (an exception, from the diaphragm selection process) and large pieces of diaphragm can be seen in the video included in the supplementary electronic material, unlike the other experiments which were conducted with aluminum diaphragms.

The transmitted shock travelled through the test gas to a chevron-shaped obstacle. The top and bottom portions of the shock diffracted past the chevron and reflected from each other at the trailing edge. The central part of the shock reflected from the chevron's inner surface, allowing the trailing edge reflection to occur undisturbed. The chevron tip was located in the last third of the shock tube at a distance $\hat{l}_{\mathrm{d}}$ from the diaphragm, listed in table 1. The chevron limbs measured 15 cm on the outside and had a 60° outer apex and 80° inner apex. This causes a trailing edge reflection with a wedge angle of $\theta_{\mathrm{w}} = 30°$. The geometry was chosen to approximate the angle between shocks at the end of a detonation cell (Strehlow & Biller (1969); Austin (2003); Radulescu *et al.* (2009); Bhattacharjee (2013)).

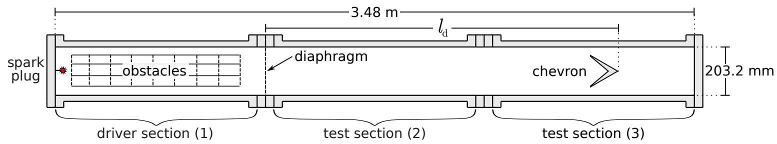

Figure 2: Diagram of the shock tube with a depth of 19.1 mm; optical access throughout the third section; the chevron has an 80° inner apex, a 60° outer apex, and 15 cm outside edges

Table 1: Experimental conditions

	Test mixture	$\hat{T}_0$ [°C]	$\hat{p}_0$ [kPa]	$\hat{l}_d$ [m]	$\hat{\lambda}_0$ [μm]	γ_0	M_c	Figures
1	N_2	20.5	3.7	1.85	1.78	1.40	2.4	3a to 3c
2	N_2	19.0	3.4	1.85	1.92	1.40	3.0	3d to 3f
3	N_2	20.5	3.8	1.85	1.73	1.40	3.5	3g to 3i
4	$0.8C_3H_8 + 0.2O_2$	21.0	6.96	1.85	0.408	1.15	2.4	4a to 4c
5	$0.8C_3H_8 + 0.2O_2$	22.0	3.5	1.85	0.816	1.15	2.9	4d to 4f
6	$0.8C_3H_8 + 0.2O_2$	21.5	3.9	1.85	0.730	1.15	3.5	4g to 4i
7	C_6H_{14}	20.0	2.6	1.85	0.500	1.06	2.5	5a to 5c
8	C_6H_{14}	22.5	2.6	1.85	0.500	1.06	2.7	5d to 5f
9	C_6H_{14}	23.0	2.3	1.85	0.574	1.06	3.4	5g to 5i
10	$0.8C_3H_8 + 0.2O_2$	23.0	14.3	0.32	0.201	1.15	4.0	6a to 6c
11	C_6H_{14}	23.5	~3.5	0.68	0.378	1.06	4.0	6d to 6f

Glass walls on the last third of the shock tube allowed optical access. A Z-type schlieren with a vertical knife edge was used to capture high-speed videos with a Phantom v1210 camera at 77481 frames per second with 0.468 μs exposures and a resolution of 384×288 pixels. The videos were centred downstream of the chevron with the trailing edge in view.

The strength of the shock interacting with the obstacle was controlled by the pressure ratio between driver and test gases. It was also affected by the distance between the chevron and diaphragm, and the diaphragm construction. High pressure ratios, short separation distances, and fewer layers of tape made for stronger shock waves.

2.2. *Experimental results*

Experimental results are shown in figures 3, 4, and 5 with decreasing isentropic exponent. They are a sample of the experiments performed. Each row of the figures shows three snapshots from one experiment. The first frame immediately before reflection, and two subsequent frames at later times. The Mach number M_c noted on the figures is the average shock strength prior to reflection, calculated using the shock spacing on the chevron surface, the inter-frame delay, and sound speed of the unshocked gas. The channel height of 0.2032 m is used to the scale the photographs. Following rows consist of different experiments at increased Mach number. Videos of the experiments can be found in the electronic supplementary material. The schlieren photographs show horizontal density gradients. Bright features indicate an increase of density from left to right, and vice versa. The experiments have been annotated, though the labels in figure 1 may aid the reader with terminology.

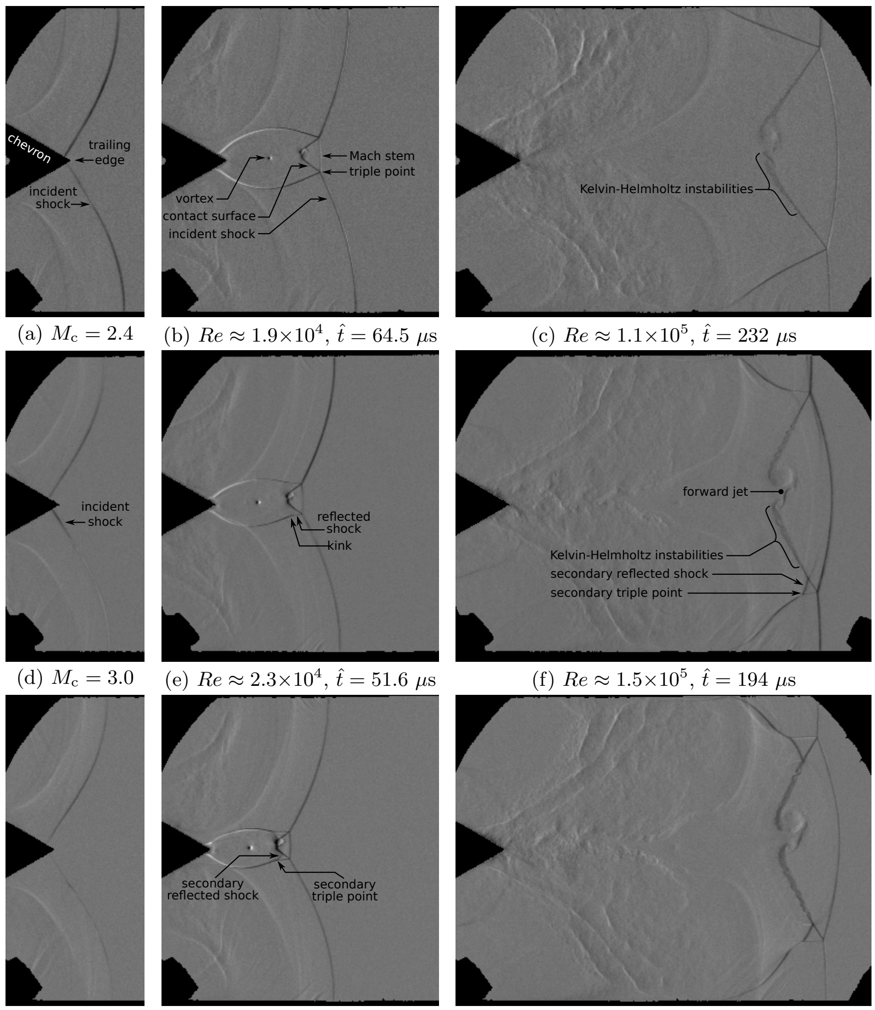

(a) $M_c = 2.4$ (b) $Re \approx 1.9\times10^4$, $\hat{t} = 64.5$ μs (c) $Re \approx 1.1\times10^5$, $\hat{t} = 232$ μs

(d) $M_c = 3.0$ (e) $Re \approx 2.3\times10^4$, $\hat{t} = 51.6$ μs (f) $Re \approx 1.5\times10^5$, $\hat{t} = 194$ μs

(g) $M_c = 3.5$ (h) $Re \approx 2.5\times10^4$, $\hat{t} = 38.7$ μs (i) $Re \approx 1.9\times10^5$, $\hat{t} = 168$ μs

Figure 3: Schlieren photographs of nitrogen experiments ($\gamma_0 = 1.4$, $\theta_w = 30°$)

2.2.1. *Experiments in nitrogen ($\gamma_0 = 1.4$)*

Figure 3a shows a schlieren photograph of an experiment in nitrogen gas, $\gamma_0 = 1.4$, immediately prior to shock reflection at the trailing edge of the chevron. The dark curves are two shocks that have diffracted over the obstacle, travelling to the right with a Mach number $M_c = 2.4$ at the chevron surface. These will form the incident shocks for the reflection in the following frames. The flow field 64.5 μs later is shown in figure 3b. Single Mach reflections are formed with a nearly straight Mach stem. The contact surfaces emanate from the triple points and curl towards the Mach stem near the centre line. The dimple to the left of the jet is a vortex created by the asymmetrical arrival of the incident shocks. The asymmetry in shock strengths prior to reflection was typically below $5\% M_c$ in all experiments and can be judged qualitatively from the first column (*e.g.* figure 3a). The flow field 232 μs after reflection is shown in figure 3c. The single Mach reflection has grown to occupy most of the channel height and the Mach stem has become curved due to unsteadiness. Whirls from Kelvin-Helmholtz instability have grown along the contact surfaces which curl towards the Mach stem near the reflecting surface.

The Mach number along the chevron is increased to $M_c = 3.0$ in the next experiment by increasing the pressure ratio between driver and test gas. A transitional Mach reflection is formed upon reflection (figure 3e) that transitions to a double Mach reflection by figure 3f, seen from the secondary triple point and reflected shock. Kelvin-Helmholtz instabilities along the contact surface appear closer to the triple point than in the previous case. The contact surface curls into a forward jet that is longer and closer to the Mach stem than the previous case.

A double Mach reflection is formed during reflection (figure 3h) when the Mach number is increased to $M_c = 3.5$. Kelvin-Helmholtz instabilities appear immediately behind the secondary reflected shock, and the contact surfaces jet towards the front.

2.2.2. *Experiments in propane with oxygen ($\gamma_0 = 1.15$)*

The set of experiments in figure 4 are performed for the same Mach numbers but at a lower isentropic exponent of $\gamma_0 = 1.15$, by changing the gas from nitrogen to rich-propane-oxygen. The contrast of the schlierens are enhanced by the increased compressibility of the gas. Reflection of the $M_c = 2.4$ shocks causes double Mach reflection, shown in figure 4b. The contact surfaces curl forward into a jet (figure 4c) that is more distinct and closer to the Mach stem than all the $\gamma_0 = 1.4$ cases, and terminates into a volute-shaped vortex that is separated from the contact surface. Kelvin-Helmholtz instabilities in the contact surface arise before the secondary shock and are carried into the forward jet.

A double Mach reflection is formed in experiments at a Mach number of $M_c = 2.9$ (4e). The vortex that forms at the head of the forward jet in figure 4f is corrugated, possibly due to the presence of Kelvin-Helmholtz instabilities in the vortex.

Increasing the Mach number to $M_c = 3.5$ causes triple points to form on the diffracting shocks, shown in figure 4g, with two short transverse shocks that span the thickness of gas shocked over the obstacle. These triple points are a result of the diffraction process (Skews (1967)). A double Mach reflection is formed and the forward jet impinges on the Mach stem, causing it to deform and bulge along the centre line (figure 4i), and possibly bifurcate.

2.2.3. *Experiments in hexane ($\gamma_0 = 1.06$)*

The isentropic exponent was lowered to $\gamma_0 = 1.06$ by employing n-hexane as test gas. A double Mach reflection forms at $M_c = 2.5$ (figure 5c) that is qualitatively similar to the $M_c = 2.9$, $\gamma_0 = 1.15$ case. The four triangular protrusions from the incident shocks seen in figure 5c are small diaphragm shards that have overtaken the slowing shock. This occurs because the layer of test gas between the shock and driver/test gas interface is thin, due to its high compressibility (low isentropic exponent), which allows spall from the diaphragm to reach the shock front.

The Mach number was increased to $M_c = 2.7$. Triple points appear on the diffracted shocks and the schlieren has a textured appearance behind the shocks (figure 5d). The shock reflection has a short Mach stem height, making it difficult to see the flow-field behind the shock front at early times (figure 5e). A double Mach reflection forms and the forward jet impinges on the Mach stem (figure 5f). The schlieren continues to have a textured appearance behind the Mach stem and reflected shocks unlike the comparably

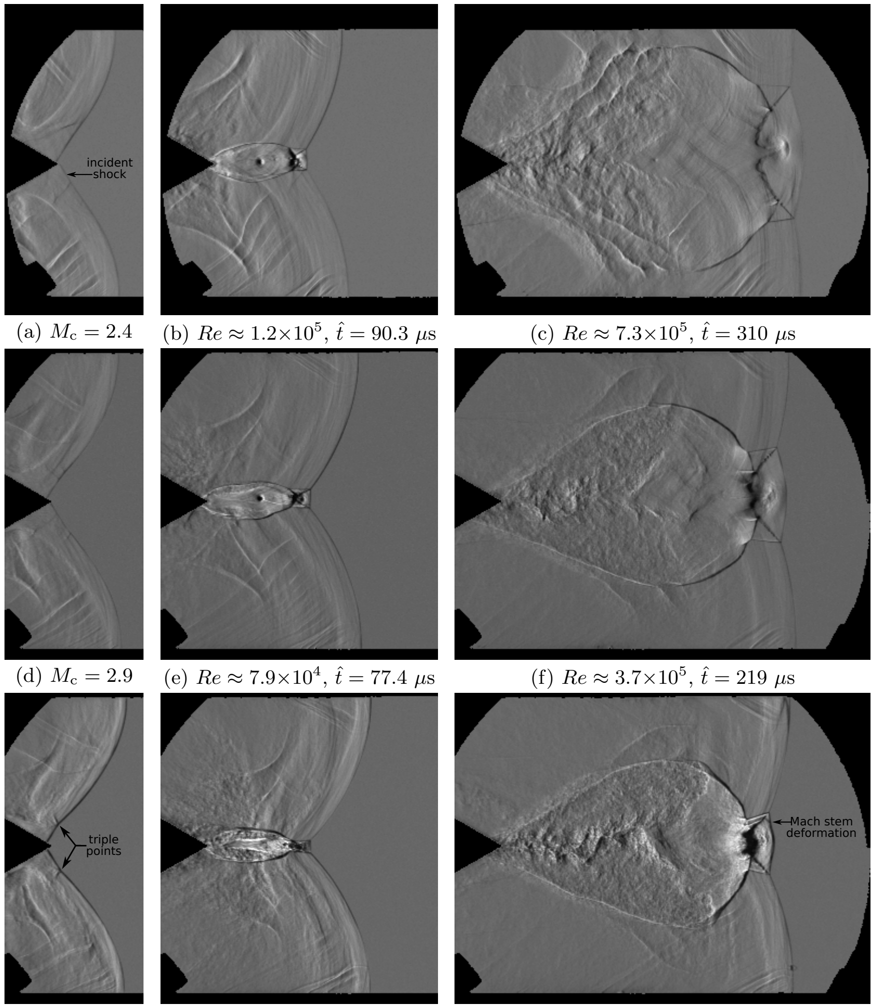

(a) $M_{\mathrm{c}} = 2.4$ (b) $Re \approx 1.2{\times}10^5$, $\hat{t} = 90.3$ μs (c) $Re \approx 7.3{\times}10^5$, $\hat{t} = 310$ μs

(d) $M_{\mathrm{c}} = 2.9$ (e) $Re \approx 7.9{\times}10^4$, $\hat{t} = 77.4$ μs (f) $Re \approx 3.7{\times}10^5$, $\hat{t} = 219$ μs

(g) $M_{\mathrm{c}} = 3.5$ (h) $Re \approx 7.9{\times}10^4$, $\hat{t} = 64.5$ μs (i) $Re \approx 3.8{\times}10^5$, $\hat{t} = 168$ μs

Figure 4: Schlieren photographs of propane-oxygen experiments ($\gamma_0 = 1.15$, $\theta_{\mathrm{w}} = 30°$)

smooth-looking flow fields seen all the previous cases, making it difficult to discern fine features. The textured appearance of the schlieren in figures 5d to 5i suggests there is some flow field instability, however it is not caused by the presence of driver gas. This will be discussed in section 4.3 and the appendix.

The textured appearance of the schlieren behind the shocks continues in the following experiment at $M_{\mathrm{c}} = 3.4$, shown in figure 5g. The forward jet reaches the Mach stem and causes it to bulge (figure 5i), and possibly bifurcate.

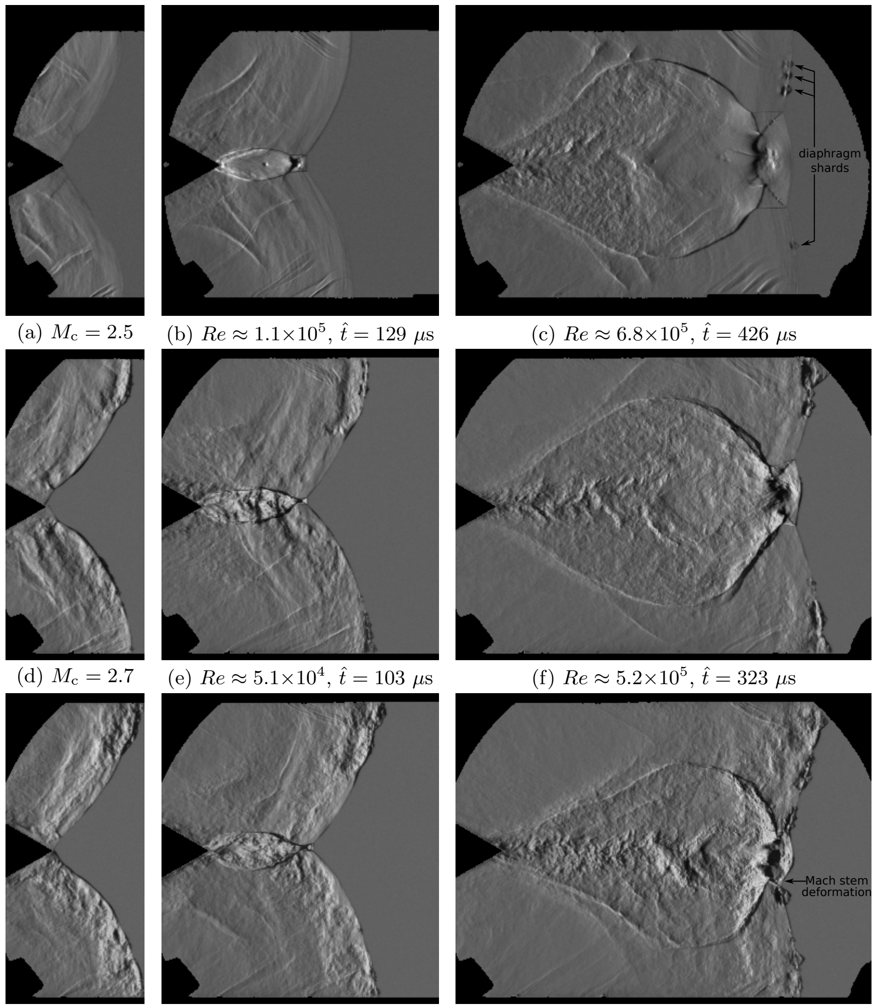

(a) $M_c = 2.5$ (b) $Re \approx 1.1{\times}10^5$, $\hat{t} = 129$ μs (c) $Re \approx 6.8{\times}10^5$, $\hat{t} = 426$ μs

(d) $M_c = 2.7$ (e) $Re \approx 5.1{\times}10^4$, $\hat{t} = 103$ μs (f) $Re \approx 5.2{\times}10^5$, $\hat{t} = 323$ μs

(g) $M_c = 3.4$ (h) $Re \approx 1.0{\times}10^5$, $\hat{t} = 90.3$ μs (i) $Re \approx 4.0{\times}10^5$, $\hat{t} = 258$ μs

Figure 5: Schlieren photographs of hexane experiments ($\gamma_0 = 1.06$, $\theta_w = 30°$)

2.2.4. *Experiments at higher Mach number*

In order to increase the Mach number further, the distance between the diaphragm and the chevron had to be reduced. The shorter stand-off distance reduces the losses faced by the shock wave before reflection, allowing for stronger shocks. A Mach number of $M_c = 4.0$ was achieved by reducing the stand-off distance to $\hat{l}_d = 0.32$ m in rich-propane-oxygen ($\gamma_0 = 1.15$), and to $\hat{l}_d = 0.68$ m in hexane ($\gamma_0 = 1.06$). The results are shown in figure 6.

Moving the diaphragm too close to the chevron, as is the case in these two experiments, causes the driver gas to interfere with the reflection, and allows mixing between driver

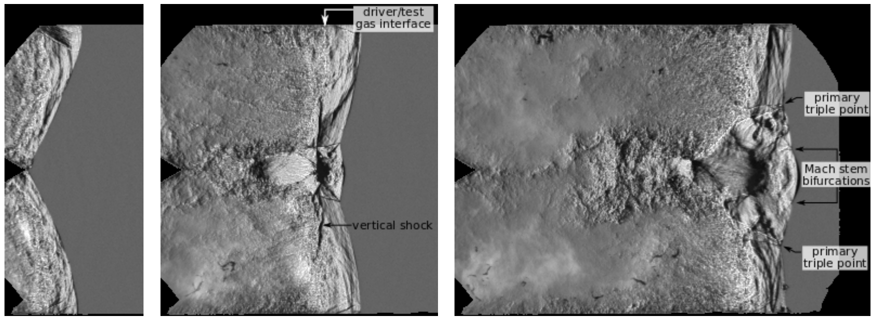

(a) $\gamma_0 = 1.15$ (b) $Re \approx 2.2{\times}10^6$, $\hat{t} = 103$ μs (c) $Re \approx 4.7{\times}10^6$, $\hat{t} = 219$ μs

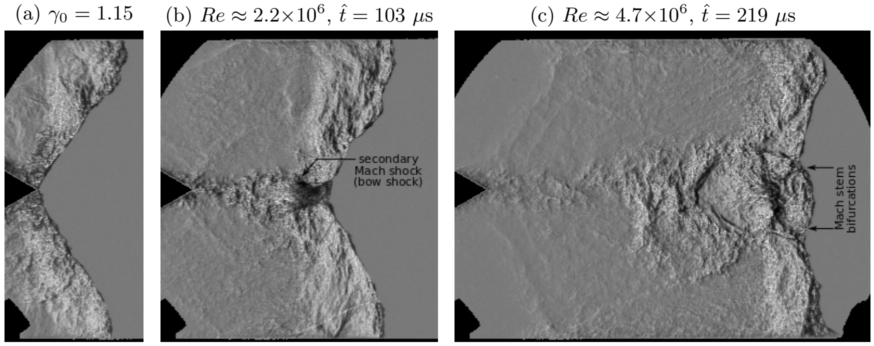

(d) $\gamma_0 = 1.06$ (e) $Re \approx 5.8{\times}10^5$, $\hat{t} = 103$ μs (f) $Re \approx 2.3{\times}10^6$, $\hat{t} = 258$ μs

Figure 6: Schlieren photographs of experiments at higher Mach number ($M_\mathrm{c} = 4.0$, $\theta_\mathrm{w} = 30°$; top row: propane–oxygen, bottom row: hexane)

and test gases near the shock front. All the previous experiments (figures 3 to 5) are not affected by the presence of the driver gas. This is evident by the fact that bow shocks remain intact and attached to the chevron in those experiments. When driver gas contamination is present, as is the case in figure 6, its high sound speed causes the bow shocks to disperse. Vertical shocks are formed in the case of figure 6b where the pressure waves meet the low sound speed test gas. Simulations in the appendix support that the driver/test gas interface is far from the leading shock in the previous experiments.

Double Mach reflections are formed with jets that reach all the way to the Mach stem, causing them to curve and bifurcate. The Mach stems are taller than the lower Mach number cases, counter to the trend seen in figures 4 and 5, due to the influence of the driver/test gas interface.

2.2.5. *Summary of experiments*

The experiments performed have shown that the propensity for strong forward jets, and their ability to reach the shock front, is favoured by decreasing the isentropic exponent and increasing the Mach number. A quantitative analysis of the experiments is presented in the following section (2.2.6) and will be compared to simulations in section 4.1. Mach stem bifurcation limits are addressed in section 4.2, and the textured appearance of the schlierens is discussed in section 4.3.

Table 2: Estimate of Reynolds number growth rates

γ_0	1.4			1.15				1.06			
M_c	2.4	3.0	3.5	2.4	2.9	3.5	4.0	2.5	2.7	3.4	4.0
$Re/\hat{h}$ [mm^{-1}]	1602	2138	2797	14490	11171	17635	79818	18523	22926	38219	78506

2.2.6. *Mach stem bulging*

The amount of Mach stem bulging is plotted against the Reynolds number in figure 7. Bulging is quantified by measuring the distance between the right-most point of the Mach stem (x_{stem}) and the horizontal position of the triple point (x_{tp}, averaged between the top and bottom triple points), and non-dimensionalized by the Mach stem height h. Each point corresponds to one frame from the experiment videos.

Definition of the Reynolds number follows that of Rikanati *et al.* (2006, 2009), who defined a shock reflection Reynolds number as

$$Re = \frac{u_{\text{shear}} h}{\nu_{\text{mean}}} \tag{2.1}$$

where u_{shear} is the velocity difference across the contact surface, ν_{mean} is the kinematic viscosity averaged across the contact surface, and h is the Mach stem height. Using this definition, they showed that Kelvin-Helmholtz instability became prominent along the contact surface in shock reflections over wedges at values of $Re > 2 \times 10^4$. This definition of the Reynolds number takes into account the velocity and viscosity across the contact surface (which forms the forward jet) where diffusion is expected to be important, while using a length scale that is characteristic to the problem and easy to measure.

The Reynolds number is estimated by using the analytic results from three shock theory to find the shear velocity and viscosity. Three shock theory is calculated using the wedge angle of $\theta_w = 30°$, the isentropic exponent γ_0 of the unshocked gas, the incident shock strength M_c along the wedge, and the unshocked temperature and pressure listed in table 1. The Mach stem height is measured directly from experiments as half the vertical distance between triple points. The Reynolds numbers for the experimental conditions are listed in table 2 as a function of Mach stem height. For example, the distance between triple points in figure 3b is $2h = 24$ mm, yielding a Reynolds number of $Re \approx 19000$.

In a self-similar pseudo-steady reflection, like the reflection of a straight shock from a wedge, the bulging plotted in figure 7 would be a horizontal line. The incident shock in these experiments is curved, causing the reflection angle and shock strength to change continuously, leading to more bulging as Reynolds number grows.

The amount of Mach stem bulging is independent of Mach number in the $\gamma_0 = 1.4$ case, where the jet does not reach the shock front, but increases with Mach number in the $\gamma_0 = 1.15$ and $\gamma_0 = 1.06$ cases, where the forward jet is closer to, or in contact with, the Mach stem. The textured appearance of the schlieren and small Mach stem heights make measurements difficult at low isentropic exponent or high Mach number, but figures 3 to 5 clearly show that the forward jet becomes increasingly important as isentropic exponent decreases, or as Mach number increases.

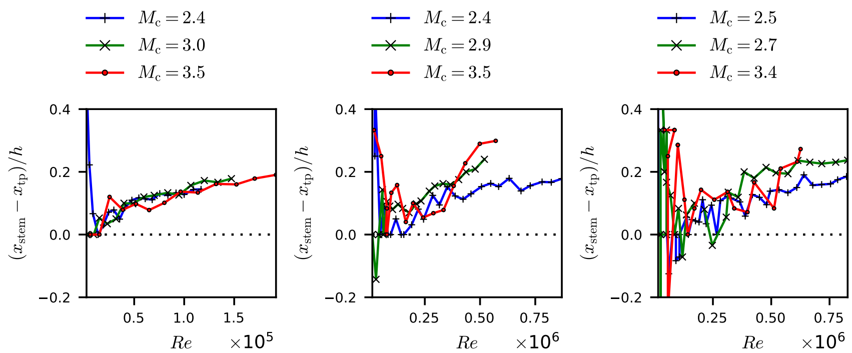

(a) $\gamma_0 = 1.4$ (b) $\gamma_0 = 1.15$ (c) $\gamma_0 = 1.06$

Figure 7: Evolution of the Mach stem bulging in experiments

3. Numerical prediction

The incident shock strength in experiments was limited to intermediate Mach numbers. Numerical simulations are used to clarify the flow field and explore higher Mach numbers. The numerical study is an extension of the work by Lau-Chapdelaine & Radulescu (2016).

3.1. *Numerical technique*

The two-dimensional Navier-Stokes equations for a calorically perfect were used. Bulk viscosity was neglected, and viscosity and heat conductivity were assumed to be power laws of temperature and a known reference state (subscript "ref")

$$\hat{\mu} = \hat{\mu}_{\mathrm{ref}}\sqrt{\frac{\hat{T}}{\hat{T}_{\mathrm{ref}}}} \quad \text{and} \quad \hat{k} = \hat{k}_{\mathrm{ref}}\sqrt{\frac{\hat{T}}{\hat{T}_{\mathrm{ref}}}}. \tag{3.1}$$

The equations were non-dimensionalized using the unshocked gas (subscript 0) as reference state

$$\hat{\rho}_{\mathrm{ref}} = \hat{\rho}_0, \quad \hat{p}_{\mathrm{ref}} = \hat{p}_0, \quad \hat{T}_{\mathrm{ref}} = \hat{T}_0, \quad \hat{x}_{\mathrm{ref}} = \hat{\lambda}_0 = \frac{\hat{\mu}_0}{\hat{p}_0}\sqrt{\frac{\pi \hat{R}_{\mathrm{s}} \hat{T}_0}{2}} \tag{3.2}$$

where ρ is density, p is pressure, T is temperature, x is the spatial dimension, R_{s} is the specific gas constant, and the circumflex (hat) indicates dimensional variables. The spatial dimension was non-dimensionalized by the mean free path in the unshocked gas $\hat{\lambda}_0$, listed in table 1 for experiments, and time was non-dimensionalized by $\hat{t}_{\mathrm{ref}} = \hat{x}_{\mathrm{ref}}\sqrt{\hat{\rho}_0/\hat{p}_0}$ for consistency. A Prandtl number of 3/4 was used for all the simulations and the isentropic exponent is uniform throughout the domain.

The equations were solved using the `mg` software package developed by Falle (Falle (1991); Falle & Komissarov (1996)). A second-order Godunov scheme using a monotonized central symmetric flux limiter (Van Leer (1977)) solved convective terms, and diffusion was solved explicitly in time and using second order central differences in space.

A Cartesian grid with adaptive mesh refinement was used. The mesh was refined by a factor of two in both directions whenever a relative tolerance of 1% was exceeded between existing mesh levels in the cell for mass, momentum, or energy. The refinement was extended five to ten existing cells from the cell needing refinement in all directions. Figure 8 shows the resulting adaptive mesh in viscous and inviscid simulations. A maximal

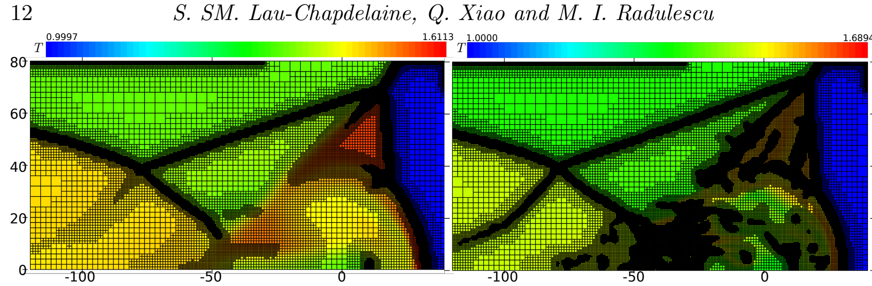
(a) Viscous (b) Inviscid

Figure 8: Adaptive computational mesh overlayed on a temperature plot ($M = 3.5$, $\gamma = 1.06$, $t = 132$)

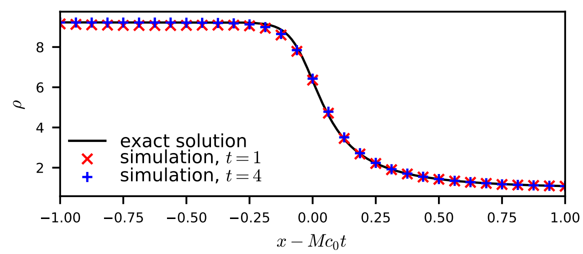

Figure 9: Comparison of the steady-state Navier-Stokes shock profile (exact solution) to a simulation evolved from a discontinuity, with a resolution of 16 grid points per mean free path ($M = 3.5$, $\gamma = 1.06$)

resolution of 16 points per unshocked mean free path was used. Under the conditions of experiment 9 (table 1), for example, the mean free path of the test gas is 0.574 μm (before being shocked). In a simulation of this experiment, each mean free path would be covered by up to 16 grid points, resulting in a maximum resolution of 16 grid points per 0.574 μm, or 0.036 μm between every grid point. Figure 9 shows the one-dimensional shock wave structure for this case ($M = 3.5$, $\gamma = 1.06$, evolved to $t = 4$ from a discontinuity). It shows that a resolution of 16 grid points/λ_0 accurately reproduces the steady-state Navier-Stokes shock profile.

The use of shock-resolved viscous simulations ensures the contact surface and forward jet are properly resolved and removes the solution's dependence on the type of solver that is chosen. The downside is that these simulations require large computational time due to the high resolution and viscous Courant-Friedrichs-Lewy (CFL) criterion. As a result, the viscous simulations were limited to the low isentropic exponent $\gamma = 1.06$. Reflections at this isentropic exponent have short Mach stems, which permits small domains, and their Reynolds numbers grow quickly thus necessitating fewer time steps. The maximum time step size was determined using the CFL condition with CFL = 0.4 on the refined meshes.

The initial conditions consisted of a triple-shock, calculated using the ideal three shock theory, whose triple point was imposed above a symmetry boundary as illustrated in figure 10. The arrows point from the post-shock state to the pre-shock state. Using a triple shock as initial condition does away with nonphysical leaky boundary conditions and provides an unambiguous way to pose the problem (Lau-Chapdelaine & Radulescu (2016)). The reflection also closely resembles triple shock reflections in detonations. The

Table 3: Initial conditions for triple shock simulations, see figure 10; pre-reflection shock Mach numbers are listed so $M_{\mathrm{i}} = M_{\mathrm{M,pre}}$; $\gamma = 1.06$, $v_0 = 0$, $p_0 = 1$, $\rho_0 = 1$, $w_0 = 150°$

$M_{\mathrm{M,pre}}$	$M_{\mathrm{i,pre}}$	$M_{\mathrm{r,pre}}$	u_0	w_1	w_2	w_3
2.5	2.03663	1.22304	-3.14027	104.462°	44.6553°	60.8829°
3	2.45729	1.21608	-3.74700	118.124°	36.2915°	55.585°
3.5	2.45762	1.21592	-3.74647	118.108°	36.2434°	55.6491°
4	3.30702	1.20460	-4.95286	140.018°	24.1620°	45.8199°
5	4.16138	1.19658	-6.15981	141.205°	23.5999°	45.1955°
6	5.01458	1.19159	-7.36482	145.904°	21.2707°	42.8248°

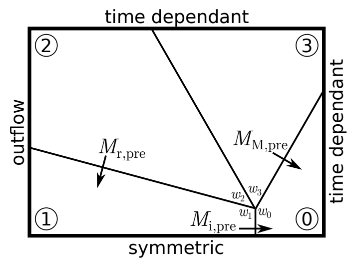

Figure 10: Initial and boundary conditions of triple shock reflection simulations; ⓪ unshocked state, ① pre-reflection incident shock state, ② pre-reflection transverse shock state, ③ pre-reflection Mach shock state and post-reflection incident shock state

initial conditions can be recreated using the data from table 3 by using the pre-reflection shock Mach numbers with the Rankine-Hugoniot equations, the frame speed u_0, and the angles w between states. The initial distance of the triple point above the symmetry boundary was chosen to allow the viscous shock structures to form for $t = 1$ before reflection. Figure 9 shows this is a sufficient amount of time for the discontinuities to adopt the correct shock profile. The frame of reference used was the ideal post-reflection triple-point speed parallel to the reflecting surface (i.e., the Mach stem speed from three shock theory). The geometry does not require the implementation of moving internal boundaries for a moving frame of reference.

In this configuration, the triple point initially moves downwards and to the left while the viscous shock structure develops (i.e., start-up error moves away from the triple point). The triple point then reflects from the origin on the symmetry boundary at $t = 0$. The pre-reflection Mach stem (the oblique shock between states ① and ③ of figure 10) becomes the post-reflection incident shock while the pre-reflection contact surface, incident and reflected shocks are washed out to the left because they travel slower than the frame.

The top and right boundaries were functions of time, moving the initial ideal shock and contact surface states along the boundaries to reduce error. An outflow condition with zero normal gradient was used on the left boundary. The domain was sized to fit the Mach stem and double Mach reflection structure at the target simulation time. The remaining parts of the reflection (*e.g.*, bow shock) were allowed to flow out of the domain. Comparison of different domain sizes showed the domains chosen were sufficiently large to have no qualitative nor quantitative effect on the phenomena being studied.

The target simulation time was found for a desired Reynolds number of $Re_{\mathrm{target}} = 1000$, defined in equation 2.1. The Mach stem height was estimated *a priori* as $h = \tan(\chi) M_{\mathrm{M}} c_0 t$, where the post-reflection triple point path angle χ and Mach stem's Mach number M_{M} were calculated from three shock theory, and c_0 is the unshocked sound speed. This yields an expression for the target time

$$t_{\mathrm{target}} = \frac{\nu_{\mathrm{mean}}}{u_{\mathrm{shear}} \tan(\chi) M_{\mathrm{M}} c_0} Re_{\mathrm{target}}. \tag{3.3}$$

The computational resources required scale with the cube of the target Reynolds number, limiting the scope of simulations to $Re \sim \times 10^3$, lower than the experiments by a factor of ~ 10 to 10^3. For example, computing the triple shock reflection with $M_{\mathrm{i}} = 2.5$ (shown in figure 11) in a domain measuring 352×192 mean free paths in the unshocked gas (coarse grid of 22×12 cells and 8 levels of refinement for a finest possible grid of 5632×3072 cells) took approximately 20 days on 60 AMD Opteron 6282 processor cores to reach the target time. The gap between resolved viscous simulations and experiments remains to be bridged, either with larger simulations or experiments at higher frame rate that focus on the early reflection.

The reflection angle was maintained at $\theta_{\mathrm{w}} = 30°$, like the experiments.

Inviscid simulations of triple shock reflection were performed under the same conditions, but without viscosity or heat conduction. The same resolution, number of refinement levels and refinement criteria were used, and they were marched to the same time as their viscous counterparts.

Full scale inviscid calculations of the experiments were also performed in order to assess the non-ideal effects present in the experiments. These simulations are provided in the appendix.

3.2. *Viscous simulation results*

Plots of temperature are presented in figures 11 to 14, cutoff at the incident shock temperature and maximal temperature in the simulation. Black is overlayed where $T \leqslant 1.01 T_0$. The temperature scales, located above the figures, apply to each sub-figure. The fraction of the domain displayed is cropped and increases linearly with time.

The triple shock reflection with an incident shock of $M_{\mathrm{i}} = 2.5$ is shown in figure 11. The Mach stem at $Re \approx 34$ after reflection is convexly curved from the reflecting surface to the triple point. The reflected shock is also convexly curved near the triple point and changes curvature to the left of the triple point, resembling a transitional Mach reflection. The contact surface and forward jet appear as Reynolds number increases to $Re \approx 76$. A double Mach reflection is formed by $Re \approx 253$, and the vortex begins to grow. Changes herein continue the same trend: the shocks and contact surface continue to become more distinct, the forward jet creeps towards the Mach shock, the jet vortex grows, and the Mach stem straightens between the triple point and Mach stem foot.

A Reynolds number of $Re \approx 1335 > Re_{\mathrm{target}}$ is reached when the target time is elapsed because the Mach stem grows taller than predicted by three shock theory. This will be discussed in section 4.1. The Reynolds number is determined the same way here as in experiments: equation 2.1 is used with the shear velocity and viscosity determined from three shock theory and the Mach stem height measured from the results.

The incident shock Mach number was increased to $M_{\mathrm{i}} = 3.0$ for figure 12. The reflection begins much the same way as before but with a Mach stem that is shorter and more rounded. The contact surface does not appear until $Re \approx 67$ when the secondary reflected shock begins to form. A double Mach reflection is clearly established by $Re \approx 282$ along with the forward jet and jet vortex. Features become more distinct as Reynolds number

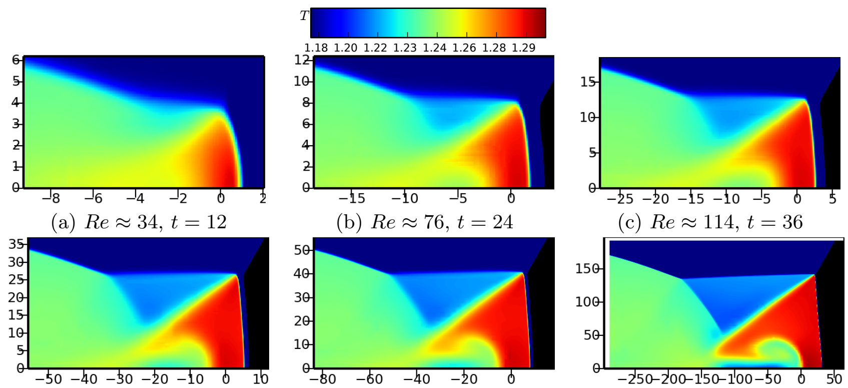

(a) $Re \approx 34$, $t = 12$ (b) $Re \approx 76$, $t = 24$ (c) $Re \approx 114$, $t = 36$

(d) $Re \approx 253$, $t = 72$ (e) $Re \approx 385$, $t = 108$ (f) $Re \approx 1335$, $t = 364$

Figure 11: Temperature plots of viscous simulations ($M_\mathrm{i} = 2.5$, $\gamma = 1.06$, $\theta_\mathrm{w} = 30°$)

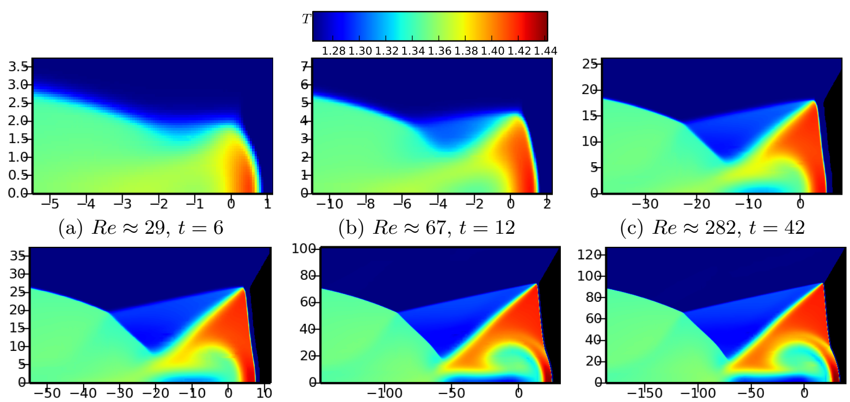

(a) $Re \approx 29$, $t = 6$ (b) $Re \approx 67$, $t = 12$ (c) $Re \approx 282$, $t = 42$

(d) $Re \approx 414$, $t = 60$ (e) $Re \approx 1174$, $t = 162$ (f) $Re \approx 1481$, $t = 203$

Figure 12: Temperature plots of viscous simulations ($M_\mathrm{i} = 3.0$, $\gamma = 1.06$, $\theta_\mathrm{w} = 30°$)

is increased. The vortex is larger than the previous case and disrupts the contact surface, causing it to deflect downwards. The vortex becomes separate from the contact surface by $Re \approx 414$. The jet moves closer to the Mach stem and causes it to bulge out ($Re \approx 1174$). The Mach stem then bifurcates through the creation of a kink on the stem ($Re \approx 1481$).

The incident shock Mach number was increased to $M_\mathrm{i} = 3.5$ for figure 13. The reflection forms a double Mach reflection similar to the previous case ($Re \approx 19$ to $Re \approx 295$). The Mach stem foot bulges ($Re \approx 295$). By $Re \approx 441$, the jet vortex occupies more than half of the Mach shocked region, disturbing the contact surface and causing a kink on the Mach stem. A triple point becomes visible at the Mach stem bifurcation ($Re \approx 914$) and a shock forms in the forward jet on the reflecting surface, located at $x - x_\mathrm{tp,ideal} \approx 10$ when $Re \approx 1593$.

Higher Mach number reflections are shown in figure 14. Their evolutions are generally the same. As Mach number increases, the jet vortex occupies a greater portion of the Mach shock area, the bifurcation point moves closer to the triple point, the shock wave in

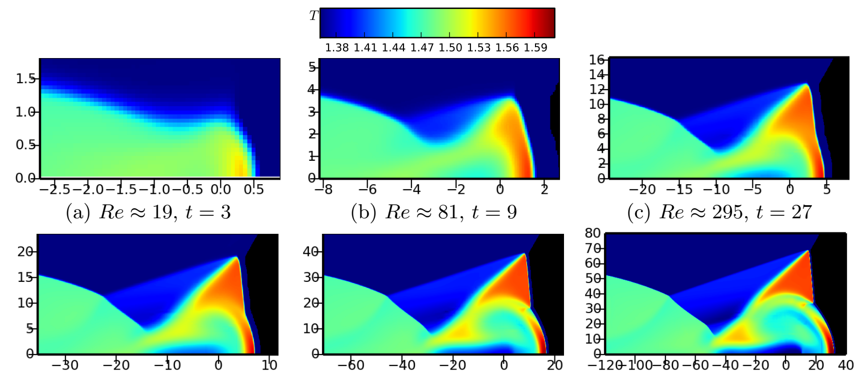

(a) $Re \approx 19$, $t = 3$ (b) $Re \approx 81$, $t = 9$ (c) $Re \approx 295$, $t = 27$

(d) $Re \approx 441$, $t = 39$ (e) $Re \approx 914$, $t = 78$ (f) $Re \approx 1593$, $t = 132$

Figure 13: Temperature plots of viscous simulations ($M_\mathrm{i} = 3.5$, $\gamma = 1.06$, $\theta_\mathrm{w} = 30°$)

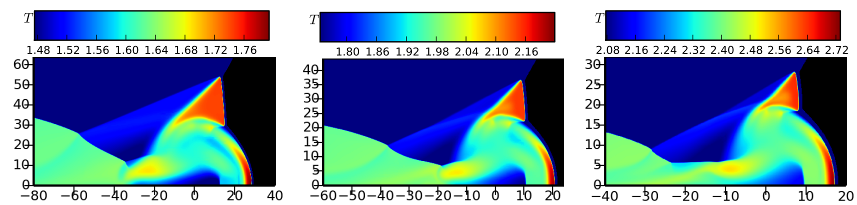

(a) $M_\mathrm{i} = 4$, $Re \approx 1672$, $t = 96$ (b) $M_\mathrm{i} = 5$, $Re \approx 1713$, $t = 58$ (c) $M_\mathrm{i} = 6$, $Re \approx 1748$, $t = 41$

Figure 14: Temperature plots of viscous simulations ($\gamma = 1.06$, $\theta_\mathrm{w} = 30°$)

the forward jet becomes taller, and the secondary reflected shock splits near the bottom wall. At $M_\mathrm{i} = 5$, the jet vortex deflects the contact surface enough to create a new shock in the reflected shock region that merges with the primary reflected shock.

3.3. *Inviscid simulation results*

The 'inviscid' simulations suffer from numerical dissipation that depends on grid and scheme, not a physical phenomenon. They do, however, offer insight on how the reflection will evolve as Reynolds number becomes large. Inviscid simulations are much faster to compute and may provide an estimation of forward jetting, Mach stem bulging, and bifurcation.

Inviscid triple shock reflection results for $M_\mathrm{i} = 2.5$ are shown in figure 15 and can be compared to the viscous case in figure 11. Large differences are present at early times. The inviscid case at $t = 12$ has a completely formed double Mach reflection with Kelvin-Helmholtz instabilities along the contact surface and a vortex that has completed more than one rotation. The Mach stem location fluctuates with time, temporarily bifurcating the Mach stem, as seen at $t = 48$. The bifurcation eventually disappears as the flow field evolves and contact surface instabilities are dragged into the forward jet where they wind up in the vortex ($t = 364$).

The inviscid simulation for $M_\mathrm{i} = 5.0$ is shown in figure 16 to illustrate how shear layer instabilities become a dominant flow feature. A double Mach reflection emerges early on at $t = 3$. By $t = 12$, the inviscid simulation has the same shape as the viscous case (figure 14b), but the temperature field in the vortex is heterogeneous. A shock starts to grow in

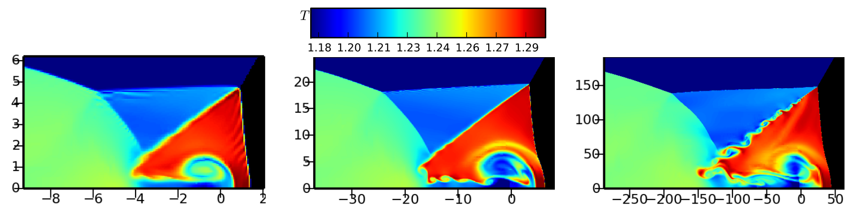

(a) $t = 12$ (b) $t = 48$ (c) $t = 364$

Figure 15: Temperature plots of inviscid simulations ($M_{\rm i} = 2.5$, $\gamma = 1.06$, $\theta_{\rm w} = 30°$)

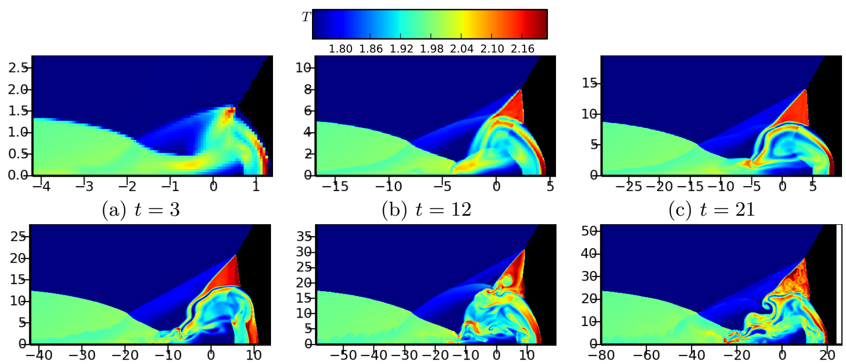

(a) $t = 3$ (b) $t = 12$ (c) $t = 21$

(d) $t = 30$ (e) $t = 42$ (f) $t = 58$

Figure 16: Temperature plots of inviscid simulations ($M_{\rm i} = 5.0$, $\gamma = 1.06$, $\theta_{\rm w} = 30°$)

the jet, perpendicular to the reflecting surface ($x - x_{\rm tp,ideal} = 5$ at $t = 21$). By $t = 30$, the foot of the Mach stem has stretched vertically and lifted the bifurcation point away from the reflecting surface. Flow near the bifurcation point interferes with the contact surface, causing the Mach stem foot to collapse back to its previous size ($t = 42$). The flow field in the vortex remains messy with sharp temperature gradients until the end of the simulation at $t = 58$. The swelling and collapse of the Mach stem foot occurs in inviscid simulations where $M_{\rm i} \geqslant 5$ and causes large fluctuations in Mach stem position. These instabilities, due to the use of the Euler equations, have marked effects on the reflection.

3.4. *Summary of simulations*

The shock-resolved viscous simulations show the importance of increasing Reynolds number and Mach number in the development of the forward jet, the jet vortex, Mach stem bulging, and bifurcation. The simulations show that growth of the forward jet leads to bulging and bifurcation. The forward jet approaches the shock front as the Reynolds number and Mach number are increased, eventually causing the Mach stem to bulge and bifurcate.

Reynolds number proves to be an important parameter in the shock reflection. The flow field changes continuously over the three orders of magnitude traversed by Reynolds number, especially behind the Mach stem. Inviscid simulations suggest continuing change as Reynolds number is further increased. Kelvin-Helmholtz instability in inviscid simulations, absent from the viscous cases, are entrained into the forward jet and vortex, resulting in a messy vortex that perturbs the Mach stem and contact surface.

Despite this, the inviscid results share some characteristics with their viscous counterparts when $Re \gtrsim 1000$, such as similar Mach stem heights, amount of bulging and bifurcation. Simulations will be compared quantitatively in section 4.1 and inviscid simulations are used to estimate the limits of Mach stem bifurcation over an extended parameter range in section 4.2.

4. Discussion

4.1. *Comparison of simulations*

The extents of forward jetting and Mach stem bulging in viscous simulations are presented in figure 17 as functions of the Reynolds and Mach numbers. Mach stem bulging is also compared to its average value in inviscid simulations. Jetting and bulging are measured as the horizontal distance between the triple point and the jet or Mach stem position on the reflecting surface, respectively, non-dimensionalized by the Mach stem height. Viscous evolutions are plotted on the left, and the average inviscid Mach stem position is plotted on the right, sharing its ordinate with the viscous graph.

Figure 17 shows that the Mach stem and jet move further ahead of the triple point as Mach number is increased. They are both affected by the Reynolds number, especially the jet. The growths of the forward jet and Mach stem bulge are not monotonic when $M_{\mathrm{i}} \geqslant 4.5$. The jet and Mach stem reach a maximum distance from the triple point before regressing. The maximum is reached first in the jet, then the Mach stem, showing that bulging is caused by the jet. This phenomenon may be affected by the development of a shock in the jet, or deflection of the contact surface by the jet's vortex. Bold points are plotted where Mach stem bifurcations were first observed. They show that bifurcations occur once the forward jet overtakes the triple point and approaches the Mach stem.

Comparing the Mach stem bulging between viscous simulations (figure 17) and experiments (figure 7c) shows more Mach stem bulging occurs in the simulations than experiments at $Re \lesssim 4{\times}10^5$, though the amounts ($(x_{\mathrm{stem}} - x_{\mathrm{tp}})/h \sim 0.15$) and trends are similar. Both show an increase of bulging with Reynolds and Mach numbers. The Mach stem becomes influenced by the forward jet at comparable Mach numbers in experiments, viscous and inviscid simulations. Bulging or bifurcation develop as Reynolds number is increased in viscous simulations and experiments. The bifurcation limits will be discussed in the following section. The viscous Mach stem position converges towards the inviscid results as Reynolds number increases. The agreement is further supported by the likeness of the triple point path angles between inviscid and viscous simulations.

The median instantaneous triple point path angles χ are plotted in figure 18 from simulations up to $Re \lesssim 2{\times}10^3$, and the same time for inviscid simulations. There is a difference of 2° to 3° between simulations and the ideal case calculated from three shock theory and may be explained by assumption in the ideal case that the Mach stem is perpendicular to the reflecting surface (Li & Ben-Dor (1999)). The difference between viscous and inviscid simulations is much smaller, but increases at high Mach number due to Mach stem swelling seen in figure 16.

Simulations and experiment are qualitatively compared in figure 19 and many characteristics. In this case ($\gamma = 1.06$, $M = 3.5$), the forward jet has caught up to the shock front and causes it to bulge in experiments, inviscid, and viscous simulations. A shock wave in the forward jet is seen in all three cases in approximately the same location on the reflecting surface. The Kelvin-Helmholtz instabilities that obscure features of the flow

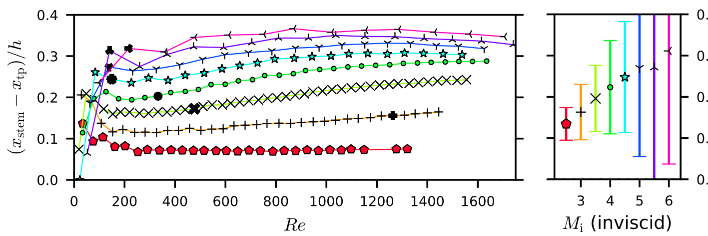

(a) Mach stem position; left: viscous, right: inviscid

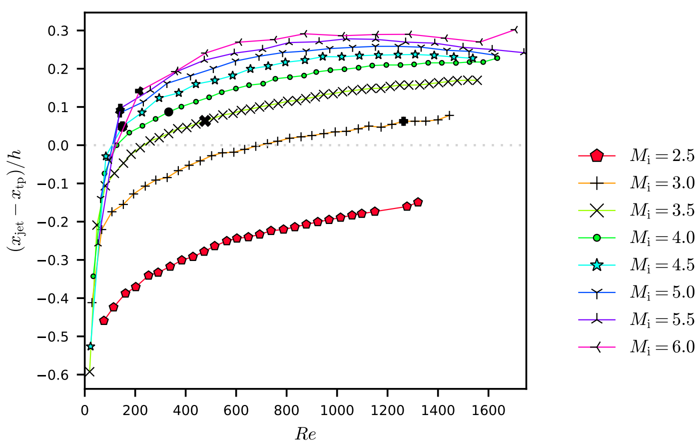

(b) Viscous jet position

Figure 17: Evolution of the Mach stem and jet at the reflecting surface from simulations ($\gamma = 1.06$, $\theta_{\rm w} = 30°$); bold points where bifurcation is first observed; error bars at 3 standard deviations

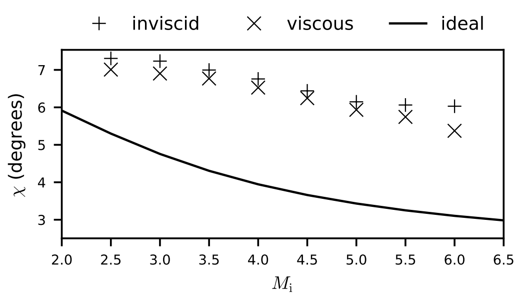

Figure 18: Angle of the triple point path with respect to the reflecting surface from three shock theory, viscous simulations up to $Re \lesssim 2{\times}10^3$, and equivalent inviscid simulations ($\gamma = 1.06$, $\theta_{\rm w} = 30°$)

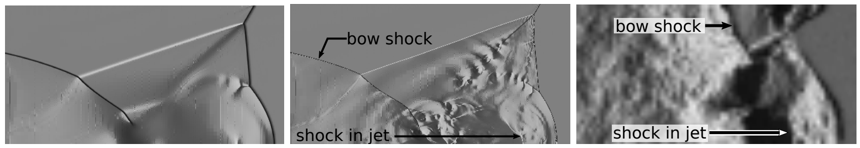

(a) Viscous simulation (b) Inviscid simulation (c) Experiment

Figure 19: Comparison of viscous ($M_\mathrm{i} = 3.5$, $Re = 1593$, $t = 132$) and inviscid ($M_\mathrm{i} = 3.5$, $t = 130$) simulations with experiment ($M_\mathrm{c} = 3.4$, $Re = 4.0{\times}10^5$, $\hat{t} = 258\mu$s, flipped vertically) at $\gamma = 1.06$

in the inviscid simulation and are likely present in the experiment. These instabilities are absent from viscous simulations at $Re \sim 10^3$, but typically become discernible in the experiments when $Re \sim 10^5$, showing the importance of Reynolds number on the flow field. Some differences exist between simulations and experiments. The bow shock and secondary triple point are closer to the front in experiments than in simulations due to unsteadiness in the experiment. Mach stem bifurcation is clear in many simulations but ambiguous in experiments. It should be noted that the bifurcation appears and disappears in the inviscid simulations at large times, suggesting that Kelvin-Helmholtz instability may damp this effect at large Reynolds number.

The quantitative comparisons between viscous and inviscid simulations (figures 17 and 18) and qualitative comparisons (*e.g.* figure 19, figures 12 and 15, figures 14b and 16) show there is agreement between inviscid and viscous simulations at $Re > 1000$ as far as the shape of the shock reflection is concerned, *i.e.* the positions of the shocks. The effect of Mach number on simulations and experiments is the same: the forward jet approaches the Mach stem as Mach number is increased, eventually disturbing the front and causing it to bulge out. However, viscosity plays an important role in the evolution of the flow field behind the Mach stem.

4.2. *Mach stem bifurcation limits*

The Reynolds number required for Mach stem bifurcation to occur in viscous simulations is plotted in figure 20 and has not been investigated previously, to the knowledge of the authors. The figure shows that Mach stem bifurcations at high incident shock Mach numbers occur early in the reflection and are largely independent of Reynolds number. The ability of the forward jet to reach and disturb the shock front appears to become sensitive to Reynolds number near the bifurcation limit, at low Mach numbers. Figure 21 shows pseudo-schlieren images (symmetric logarithmic horizontal density gradients) of inviscid simulations near the bifurcation limit at early times (top row, equal to when three shock theory predicts $Re_\mathrm{target} = 100$) and an order of magnitude later (bottom row). No bifurcation is present at $M_\mathrm{i} = 2.5$, and a bifurcation is present at $M_\mathrm{i} = 3$. The $M_\mathrm{i} = 2.75$ case is critical, with a bifurcation occurring at $Re_\mathrm{target} = 100$, but disappearing by $Re_\mathrm{target} = 1000$. Kelvin-Helmholtz instabilities are absent from the flow field at early times but appear at later times, accompanied by a reduction in bulging. This highlights the sensitivity of near-limit Mach stem bifurcation to the flow field behind the Mach stem, which is governed by Reynolds number.

In experiments, the forward jet reaches and disturbs the Mach stem at $3.4 \approx M_\mathrm{c}$ for $\gamma_0 = 1.15$, and $2.7 \approx M_\mathrm{c}$ for $\gamma_0 = 1.06$, but did not reach the front in the $\gamma_0 = 1.4$ reflections. Bifurcations appeared in viscous and inviscid simulations ($\gamma = 1.06$) at the same Mach numbers, between $2.5 < M_\mathrm{i} \leqslant 3.0$. The resolution of the experiments limits visualization of the reflection to Reynolds numbers $\gtrsim 10^5$, where instabilities may affect

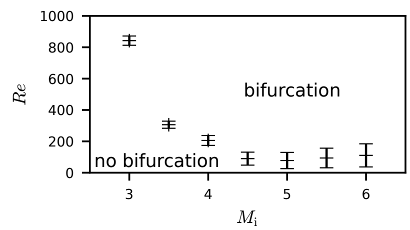

Figure 20: Onset of Mach stem bifurcation in viscous simulations ($\gamma = 1.06$, $\theta_\mathrm{w} = 30°$)

the shock front, especially since the Mach numbers lie near the bifurcation limit. Shock reflections in experiments are affected by bulk viscosity which is neglected in simulations, and they are subject to boundary layers that develop along the chevron and the walls of the thin channel. Between the shock and the rear of the jet, approximately 5 cm in figure 3c (the largest case), these boundary layers are expected to grow 0.9 mm (Fay (1959)). During the same time, the shock has travelled about 20 cm from the tip of the obstacle, and the unsteadiness of the experiments is expected to have a larger impact than the boundary layers.

The agreement of inviscid Mach stem bulging and bifurcation limits with viscous simulations encourages the use of inviscid simulations to explore the Mach stem bifurcation boundary over a wider parameter range. A number of inviscid simulations were performed, varying the incident shock Mach number, reflection angle, and isentropic exponent. It is ambiguous how long an inviscid simulation should be run, due to the lack of scale, so the time where the viscous case would reach $Re_\mathrm{target} = 100$ was chosen and calculated for each parameter set. The results were examined for a Mach stem bifurcation, as labelled in figure 21. If a bulge and transverse shock wave were seen together on the Mach stem, it was considered to have bifurcated. This is similar to the sorting between transitional and double Mach reflections that has been done in the past. The results are plotted in figures 22 and 23. Each square represents one simulation. Hollow squares indicate simulations without bifurcation, and filled squares show simulations with a bifurcated Mach stem. The actual Mach stem bifurcation limit lies somewhere near the interface of solid and hollow squares, as it is sensitive to Reynolds number.

The bifurcation limits of the inviscid simulations in figure 22 agree with the viscous simulations performed in this study. The $\gamma = 1.15$ limit is also close to the bifurcation boundary of $3.84 < M_\mathrm{i} \leqslant 4.09$ at $\gamma_0 = 1.13$ and $\theta_\mathrm{w} = 15°$ found by Semenov *et al.* (2009) for shock reflection from a wedge.

A number of curves are plotted along with the simulation results. They delimit some shock reflection behaviours. The sonic criterion of the regular reflection boundary (ir/rr) is plotted with a solid horizontal curve above which Mach reflections do not occur. The bottom solid curve connected to the vertical line represents the single/transitional Mach reflection boundary (sMr/tMr). Transitional and double Mach reflections occur above this curve. These boundaries are not crucial to this study, but help situate where Mach stem bifurcations occur relative to other reflection types.

Figure 22 shows that Mach stem bifurcations occur at high Mach numbers or wedge angles. The bifurcation limit is pushed to higher Mach numbers and wedge angles when the isentropic exponent is increased. A turning point occurs where the bifurcation limit crosses the dashed curve.

The dashed curve is the boundary between cases I and II of the double Mach reflection (dMr I/II), defined and analyzed by Li & Ben-Dor (1995). Case I lies below the curve,

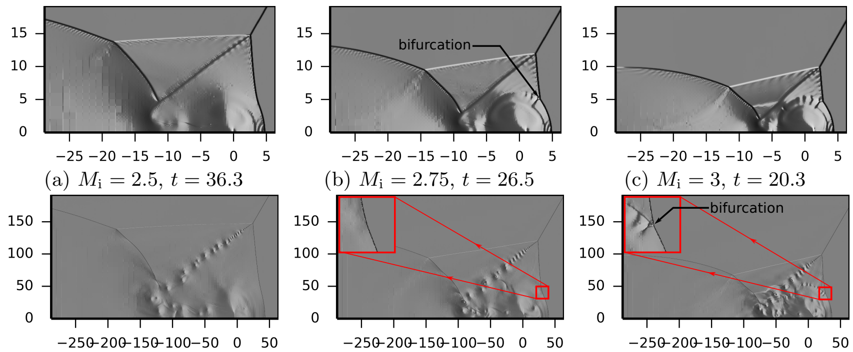

(a) $M_\mathrm{i} = 2.5$, $t = 36.3$ (b) $M_\mathrm{i} = 2.75$, $t = 26.5$ (c) $M_\mathrm{i} = 3$, $t = 20.3$

(d) $M_\mathrm{i} = 2.5$, $t = 363$ (e) $M_\mathrm{i} = 2.75$, $t = 265$ (f) $M_\mathrm{i} = 3$, $t = 203$

Figure 21: Comparison of inviscid simulations across the bifurcation boundary at times equal to viscous triple shock calculations with $Re_\mathrm{target} = 100$ (top) and 1000 (bottom), $\gamma = 1.06$, $\theta_\mathrm{w} = 30°$; insets at the top left of the subfigures are magnifications of the Mach stem

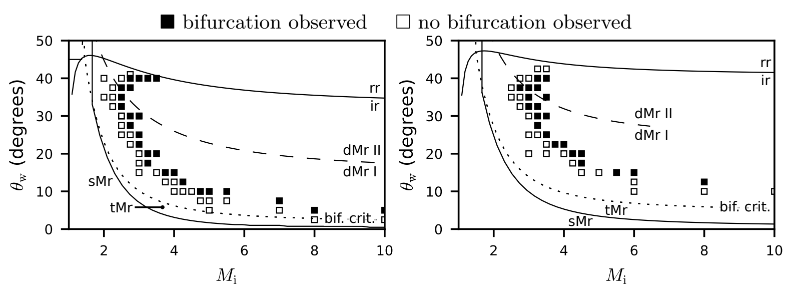

(a) $\gamma = 1.06$ (b) $\gamma = 1.15$

Figure 22: Mach stem bifurcation domain from inviscid simulations; rr: regular reflection; ir: irregular reflection; sMr: single Mach reflection; tMr: transitional Mach reflection; dMr: double Mach reflection, cases I and II; bif. crit.: analytic bifurcation criterion (bifurcations above, no bifurcations below)

and case II above. The flow around the secondary triple point in a double Mach reflection can be calculated using three shock theory, but an assumption about the angles between the shocks is needed. In a case I double Mach reflection, the secondary reflected shock is assumed to be straight and intersect the contact surface at a right angle, like in figures 11 and 12. A case II double Mach reflection occurs when the intersection would occur below the reflecting surface because the secondary triple point is too far to the left. In this case, the secondary reflected shock is assumed to form a straight line between the secondary triple point and the intersection of the contact surface with the reflecting surface.

The case I/II boundary fits well with the change of direction of the bifurcation limit. Mach (2011) postulated the secondary reflected shock of a case II double Mach reflection would turn the flow parallel to the wedge, away from the Mach stem. The transition from case I to II double reflections pushes the bifurcation limit to higher Mach numbers, but Mach stem bifurcation still occurs in the case II domain, as shown at $M = 6$ and $\gamma = 1.06$ in figure 14.

The dotted line in figure 22 (bif. crit.) is an analytic bifurcation criterion proposed by Mach (2011). It is based on the idea that the contact surface must eventually become parallel to the wall (Hornung (1986)). When pressure from the flow deflection process (flow passing the wedge tip) exceeds pressure from the shock reflection process, a stagnation point is created on the left side of the contact surface. Flow to the right of the stagnation streamline is driven into the forward jet. The flow speed of gas passed through the reflected shock, which is redirected into the jet, can be compared to the Mach stem speed (Li & Ben-Dor (1999); Mach (2011)). If the flow is faster than the Mach stem, bifurcation is assumed to occur.

This criterion underestimates the Mach number and wedge angle required for bifurcation, as seen in figure 22. Li & Ben-Dor (1999) performed a similar analysis on the jet, including the state change across the secondary reflected shock. They applied shock dynamics theory to account for bulging (not bifurcation) of the shock to estimate deflection of the Mach stem at the triple point. Shi *et al.* (2019) found this overestimates bulging and that the volumetric flux of the jet was a better estimate. Nevertheless, it is likely that deflection of the Mach stem delays bifurcation by accommodating an impinging forward jet through bulging. The secondary reflected shock, which is unaccounted for in Mach's bifurcation criterion also attenuates the forward jet, however, the secondary reflected shock is weak and is likely only a minor contribution to the underestimate. The jet vortex may also play a role, although it is unclear. The vortex disturbs the contact surface and Mach stem and is most severe when the Mach stem is short, at low isentropic exponents, and could contribute to the cutoff of bifurcations at high isentropic exponents.

The θ_w–M_i phase space diagrams of figure 22 show the bifurcation limit lies at lower Mach numbers and wedge angles at $\gamma = 1.06$ than $\gamma = 1.15$. The isentropic exponent dependence of the bifurcation boundary is plotted in figure 23 in M_i–γ phase space at a wedge angle of $\theta_\mathrm{w} = 30°$. Again, each square represents one inviscid simulation and is filled if Mach stem bifurcation was observed. The dotted curve represents Mach's bifurcation criterion, with bifurcations predicted above the curve. The Mach number required for bifurcation increases with isentropic exponent until $\gamma \approx 1.3$ is reached. Strong jets that bulge the Mach stem are still present at $\gamma = 1.4$, but bifurcation was not observed above $\gamma \approx 1.3$ despite Mach's bifurcation criterion predicting otherwise. This sort of limit is absent in Mach's bifurcation criterion, suggesting a missing link between jetting and bifurcation.

Thermochemical non-equilibrium effects are important for strong shocks and may affect the bifurcation cut-off seen at $\gamma \approx 1.3$ in figure 23. While no Mach stem bifurcation was shown in the thermochemically frozen simulations of Shi *et al.* (2019), their thermochemical non-equilibrium simulations showed a bifurcation limit between $7 < M \leqslant 8$ ($\gamma_0 = 1.4$, $\theta_\mathrm{w} = 35°$). This difference can be reconciled by considering the equilibrium post-shock state of a $M = 8$ shock through air, which has an isentropic exponent $\gamma_1 = 1.28$ and lies within the bifurcation limit presented here (for $\theta_\mathrm{w} = 30°$).

4.3. *Shock instability at high Mach number and low isentropic exponent*

The textured appearance of certain schlieren videos (*e.g.* experiments of figures 4g, 5d, and 5g) indicates a non-uniform density field. This non-uniformity worsens as the isentropic exponent is decreased from $\gamma_0 = 1.15$ to 1.06 and as the Mach number is increased, however, it is completely absent from the Navier-Stokes simulations presented in this work. The non-uniformity is not caused by contamination of the flow field by driver gas. This is evident by the fact the bow shocks remain intact and attached to the chevron, as discussed in section 2.2.4. Additionally, simulations of the experiment in the appendix show that the driver/test gas interface is far from the leading shock

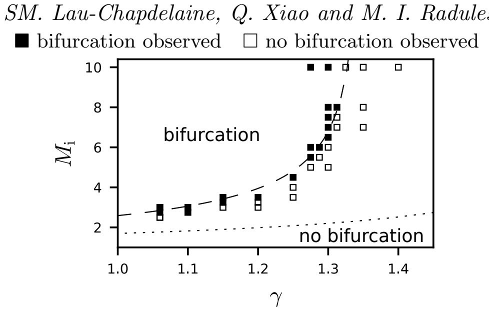

Figure 23: Mach stem bifurcation domain from inviscid simulations at a fixed angle ($\theta_w = 30°$); dotted: analytic bifurcation criterion; dashed: shock Mach number for a density ratio of 6.7

in all experiments with the full stand-off distance of $\hat{l}_d = 1.85$. Shadowgraphs of shock reflections in the low isentropic exponent experiments of Semenov *et al.* (2009) also have the same textured appearance. The cause of the phenomenon is not understood but may be linked to shock wave instability.

Shock wave instability has been ascribed to endothermic processes such as ionization (Grun *et al.* (1991); Glass & Liu (1978); Griffiths *et al.* (1976)), dissociation (Griffiths *et al.* (1976)), or to heavy gases (i.e. low isentropic exponent gases) where vibrational relaxation may occur behind the shock (Griffiths *et al.* (1976); Mishin *et al.* (1981); Hornung & Lemieux (2001); Semenov *et al.* (2009); Ohnishi *et al.* (2015)). Shock instability has been observed by Sirmas & Radulescu (2015, 2019) in molecular dynamic calculations of relaxing shock waves in gases with inelastic collisions, as would be the case with strong vibrational relaxation effects. Work from hypersonic projectiles have attributed similar shock instability to vibrating or unstable contact surfaces. Experiments and simulations of Hornung & Lemieux (2001) and Ohnishi *et al.* (2015) found instability when density ratios of $\gtrsim 14$ and $\gtrsim 10$ were reached across the shock. For comparison, the experiment of figure 5g ($\gamma = 1.06$, $M = 3.4$) has a density ratio of 8.8 across the incident shock, and higher across the Mach stem. Interestingly, the bifurcation boundary in M–γ space is well represented by a shock jump density ratio of $\rho_{\text{shock}}/\rho_0 = 6.7$, plotted with a dashed curve in figure 23. This suggests that similar phenomena may underpin Mach stem bifurcation, shock instability, and perhaps detonation regularity.

Despite similarities between the shock instability boundary and the bifurcation boundary, simulations of the Navier-Stokes equations in this study did not show instability. The stability of these low isentropic exponent gases is of interest and should be investigated in future work, for instance by introducing vibrational relaxation effects into simulations.

4.4. *Implication to detonation structure*

Shock reflections have been shown to contribute to the propagation of detonations (Lee (2008)). Detonations are supersonic combustion waves composed of a lead shock followed by an induction zone with little change in thermodynamic state, followed by a reaction zone where reactants are quickly consumed. Detonations suffer from a multi-dimensional instability that causes their shock front to be punctuated by triple points. Triple points periodically reflect from each other, creating new triple points that travel in opposite directions. A curved Mach stem is formed upon reflection, like the experiments, and the new triple points go on to collide with their other neighbours. The shared Mach stem becomes the incident shock for the next reflection and the process repeats. The experiments' curved shocks form a nice analogue to the unsteady shock reflection process in detonations.

The experiments and simulations show the forward jet and vortex introduce large scale turbulence that disturbs the structure of the flow behind the Mach stem. In detonations, the reaction rates of flow behind the Mach stem is likely increased by the instabilities and turbulence introduced at low isentropic exponents and high Mach numbers. However, the chemical time scales must be compared to the time scales required for the hydrodynamic features to develop as Reynolds number was found to be important.

Tracing the triple point paths of a detonation creates a pattern of interlocking diamond or fish-scale shapes called the cellular detonation structure. Detonations are often characterized by the size and regularity of their cellular structure. Detonations with irregular structures tend to be more resistant to quenching and their mixtures easier to detonate (Moen *et al.* (1986); Radulescu & Lee (2002)). The forward jet deforms the Mach stem and causes it to bifurcate under certain conditions. Radulescu *et al.* (2009); Mach & Radulescu (2011); Mach (2011) proposed that Mach stem bifurcation could be a source of new detonation cells that contribute to the irregularity of the cellular structure. Mach & Radulescu (2011); Mach (2011) compared shock reflection simulations to experimental results and found excellent agreement. The detonations had an irregular structure when bifurcation was observed in their inviscid simulations. They listed post-shock isentropic exponents of $\gamma_1 \leqslant 1.32$ and $\gamma_1 \geqslant 1.41$ for irregular and regular detonations, respectively, which closely matches the bifurcation limit found in this study, in figure 23. The influence of low isentropic exponents on detonation propagation is supported by Maley *et al.* (2015) who found that forward jets from shock reflections enhanced mixing, leading to Mach stem bifurcation when $Re \gtrsim 10^5$ and $\gamma_1 = 1.22$. Forward jets were absent from their experiments with $\gamma_1 = 1.36$. A parametric investigation of the effect of the isentropic exponent on detonation propagation and regularity would be of particular interest.

It is additionally possible that the proximity of detonation products to the shock front influences Mach stem bulging and bifurcations. Experiments and the simulation (in the appendix) performed with short stand-off distances had taller bifurcated Mach stems. Unsteadiness may also play an important role as it causes the shock reflection structure to change, possibly letting the jet penetrate to the front as the Mach stem slows down. The influence of these phenomena on detonation propagation or the cellular structure, if any, require more study.

5. Conclusion

Through experiments and simulations, the isentropic exponent and the Mach number were shown to be two governing parameters of the flow behind the Mach stem. As the isentropic exponent is decreased and the Mach number is increased, the forward jet approaches the Mach stem and develops a vortex. The jet and vortex can grow strong enough to completely disrupt the flow field behind the Mach shock. When the jet-shock interaction becomes important and the Mach stem bulges out.

Reynolds number proves to be another important parameter. The region behind the Mach stem is shown to continuously evolve over three orders of magnitude of Reynolds numbers. The effect of Reynolds number is most significant at low Mach numbers. Comparison of inviscid simulations and viscous simulations up to $Re \sim 1000$ have vastly different flow fields behind the Mach shock. This implies that Euler calculations must be used with care when the flow-field behind the Mach stem is important, such as in detonations. Conversely, the shape of the shock reflection is relatively indifferent to viscosity: the size of the Mach stem bulge and the triple point path angle of viscous simulations converge towards the inviscid results.

The limits of Mach stem bifurcation have been reported in θ_w–M_i–γ phase space. Bifurcations are found to be absent when $\gamma \gtrsim 1.3$ at $\theta_w = 30°$, a limit which corresponds closely to the regular/irregular cellular structure of detonations. This reinforces the idea (Radulescu *et al.* (2009); Mach & Radulescu (2011); Mach (2011)) that Mach stem bifurcation may be responsible for the generation of new detonation cells.

The authors thank Sam Falle from the University of Leeds for generously allowing the use of his computational code `mg` which made the numerical simulations possible.

The authors acknowledge financial support from the Natural Sciences and Engineering Research Council of Canada (NSERC) through the Discovery Grant "Predictability of detonation wave dynamics in gases: experiment and model development" (2017–2022).

REFERENCES

Austin, J. M. 2003 The role of instability in gaseous detonation. Ph.D. thesis, California Institute of Technology.

Barbosa, F. J. & Skews, B. W. 2002 Experimental confirmation of the von Neumann theory of shock wave reflection transition. *Journal of Fluid Mechanics* **472**, 263–282.

Ben-Dor, G. 2007 *Shock wave reflection phenomena*. Springer.

Ben-Dor, G., Mazor, G., Takayama, K. & Igra, O. 1987 Influence of surface roughness on the transition from regular to Mach reflection in pseudo-steady flows. *Journal of Fluid Mechanics* **176**, 333–356.

Bhattacharjee, R. R. 2013 Experimental Investigation of Detonation Re-initiation Mechanisms Following a Mach Reflection of a Quenched Detonation. mastersthesis, University of Ottawa.

Falle, S. A. E. G. 1991 Self-similar jets. *Monthly Notices of the Royal Astronomical Society* **250** (3), 581–596.

Falle, S. A. E. G. & Giddings, J. R. 1992 Body capturing using adaptive Cartesian grids. *Numerical methods for fluid dynamics* pp. 335–342.

Falle, S. A. E. G. & Komissarov, S. S. 1996 An upwind numerical scheme for relativistic hydrodynamics with a general equation of state. *Monthly Notices of the Royal Astronomical Society* **278** (2), 586–602.

Fay, James A 1959 Two-dimensional gaseous detonations: Velocity deficit. *The Physics of Fluids* **2** (3), 283–289.

Glass, I. I. & Liu, W. S. 1978 Effects of hydrogen impurities on shock structure and stability in ionizing monatomic gases. Part 1. Argon. *Journal of Fluid Mechanics* **84** (1), 55–77.

Glaz, H. M., Colella, P., Glass, I. I. & Deschambault, R. L. 1985*a* A detailed numerical, graphical, and experimental study of oblique shock wave reflections. *Tech. Rep.* LBL-20033. Lawrence Berkeley National Laboratory.

Glaz, H. M., Colella, P., Glass, I. I. & Deschambault, R. L. 1985*b* A numerical study of oblique shock-wave reflections with experimental comparisons. *Proceedings of the Royal Society of London. A. Mathematical and Physical Sciences* **398** (1814), 117–140.

Griffiths, R. W., Sandeman, R. J. & Hornung, H. G. 1976 The stability of shock waves in ionizing and dissociating gases. *Journal of Physics D: Applied Physics* **9** (12), 1681.

Grun, J., Stamper, J., Manka, C., Resnick, J., Burris, R., Crawford, J. & Ripin, B. H. 1991 Instability of Taylor-Sedov blast waves propagating through a uniform gas. *Physical review letters* **66** (21), 2738.

Henderson, L. F. & Lozzi, A. 1975 Experiments on transition of Mach reflexion. *Journal of Fluid Mechanics* **68** (01), 139–155.

Higashino, F., Henderson, L. F. & Shimizu, F. 1991 Experiments on the interaction of a pair of cylindrical weak blast waves in air. *Shock Waves* **1** (4), 275–284.

Hornung, H. 1985 The effect of viscosity on the Mach stem length in unsteady strong shock reflection. In *Flow of Real Fluids*, pp. 82–91. Springer.

Hornung, H. 1986 Regular and Mach reflection of shock waves. *Annual Review of Fluid Mechanics* **18**, 33–58.

Hornung, H. G. & Lemieux, P. 2001 Shock layer instability near the Newtonian limit of hypervelocity flows. *Physics of Fluids* **13** (8), 2394–2402.

Lau-Chapdelaine, S. SM. & Radulescu, M. I. 2013 Non-uniqueness of solutions in asymptotically self-similar shock reflections. *Shock Waves* **23** (6), 595–602.

Lau-Chapdelaine, S. SM. & Radulescu, M. I. 2016 Viscous solution of the triple-shock reflection problem. *Shock Waves* **26** (5), 551–560.

Lee, J. H. S. 2008 *The detonation phenomenon*. Cambridge: Cambridge University Press.

Li, H. & Ben-Dor, G. 1995 Reconsideration of pseudo-steady shock wave reflections and the transition criteria between them. *Shock waves* **5** (1-2), 59–73.

Li, H. & Ben-Dor, G. 1999 Analysis of double-Mach-reflection wave configurations with convexly curved Mach stems. *Shock Waves* **9** (5), 319–326.

Mach, P. 2011 Bifurcating Mach Shock Reflections with Application to Detonation Structure. mastersthesis, University of Ottawa.

Mach, P. & Radulescu, M. I. 2011 Mach reflection bifurcations as a mechanism of cell multiplication in gaseous detonations. *Proceedings of the Combustion Institute* **33** (2), 2279–2285.

Maley, L. 2015 On Shock Reflections in Fast Flames. Masters thesis, University of Ottawa.

Maley, L., Bhattacharjee, R., Lau-Chapdelaine, S. SM. & Radulescu, M. I. 2015 Influence of hydrodynamic instabilities on the propagation mechanism of fast flames. *Proceedings of the Combustion Institute* **35** (2), 2117–2126.

Mishin, G. I., Bedin, A. P., Iushchenkova, N. I., Skvortsov, G. E. & Riazin, A. P. 1981 Anomalous relaxation and instability of shock waves in gases. *Soviet Physics Technical Physics* **26**, 2315–2324.

Moen, I. O., Sulmistras, A., Thomas, G. O., Bjerketvedt, D. & Thibault, P. A. 1986 Influence of cellular regularity on the behavior of gaseous detonations. *Dynamics of explosions* pp. 220–243.

Ohnishi, N., Sato, Y., Kikuchi, Y., Ohtani, K. & Yasue, K. 2015 Bow-shock instability induced by Helmholtz resonator-like feedback in slipstream. *Physics of Fluids* **27** (6), 066103.

Quirk, J. J. 1992 A contribution to the great Riemann solver debate. ICASE 92-94. Springer.

Radulescu, M. I. & Lee, J. H.S. 2002 The failure mechanism of gaseous detonations: experiments in porous wall tubes. *Combustion and Flame* **131** (1), 29–46.

Radulescu, M. I., Papi, A., Quirk, J. J., Mach, P. & Maxwell, B. M. 2009 The origin of shock bifurcations in cellular detonations. *22nd ICDERS* .

Rikanati, A., Sadot, O., Ben-Dor, G., Shvarts, D., Kuribayashi, T. & Takayama, K. 2006 Shock-wave mach-reflection slip-stream instability: a secondary small-scale turbulent mixing phenomenon. *Physical Review Letters* **96** (17), 174503.

Rikanati, A., Sadot, O., Ben-Dor, G., Shvarts, D., Kuribayashi, T. & Takayama, K. 2009 A secondary small-scale turbulent mixing phenomenon induced by shock-wave Mach-reflection slip-stream instability. In *Shock Waves*, *26th*, vol. 2, pp. 1347–1352. Springer.

Samtaney, R. & Pullin, D. I. 1996 On initial-value and self-similar solutions of the compressible Euler equations. *Physics of Fluids* **8** (10), 2650–2655.

Semenov, A. N., Berezkina, M. K. & Krasovskaya, I. V. 2009 Classification of shock wave reflections from a wedge. Part 2: Experimental and numerical simulations of different types of Mach reflections. *Technical Physics* **54** (4), 497–503.

Semenov, A. N., Berezkina, M. K. & Krassovskaya, I. V. 2012 Classification of pseudo-steady shock wave reflection types. *Shock Waves* **22** (4), 307–316.

Shi, Jing, Zhang, Yong-Tao & Shu, Chi-Wang 2003 Resolution of high order WENO schemes for complicated flow structures. *Journal of Computational Physics* **186** (2), 690–696.

Shi, X., Zhu, Y., Luo, X. & Yang, J. 2017 Numerical Study on Double Mach reflection of Strong Moving Shock involving Laminar Transport. In *21st AIAA International Space Planes and Hypersonics Technologies Conference*. Xiamen, China.

Shi, X., Zhu, Y., Yang, J. & Luo, X. 2019 Mach stem deformation in pseudo-steady shock wave reflections. *Journal of Fluid Mechanics* **861**, 407–421.

Sirmas, N. & Radulescu, M. I. 2015 Evolution and stability of shock waves in dissipative gases characterized by activated inelastic collisions. *Physical Review E* **91** (2).

Sirmas, N. & Radulescu, M. I. 2019 Structure and stability of shock waves in granular gases. *Journal of Fluid Mechanics* Accepted.

Skews, B. W. 1967 The shape of a diffracting shock wave. *Journal of Fluid Mechanics* **29** (02), 297–304.

Smith, W. R. 1959 Mutual reflection of two shock waves of arbitrary strengths. *Physics of Fluids* **2** (5), 533–541.

Sorin, R., Zitoun, R., Khasainov, B. & Desbordes, D. 2009 Detonation diffraction through different geometries. *Shock Waves* **19** (1), 11–23.

Strehlow, R. A. & Biller, J. R. 1969 On the strength of transverse waves in gaseous detonations. *Combustion and Flame* **13** (6), 577–582.

Van Leer, B. 1977 Towards the ultimate conservative difference scheme. IV. A new approach to numerical convection. *Journal of computational physics* **23** (3), 276–299.

Vasilev, E. I., Ben-Dor, G., Elperin, T. & Henderson, L. F. 2004 The wall-jetting effect in Mach reflection: NavierStokes simulations. *Journal of Fluid Mechanics* **511**, 363–379.

Vasilev, E. I., Elperin, T. & Ben-Dor, G. 2008 Analytical reconsideration of the von Neumann paradox in the reflection of a shock wave over a wedge. *Physics of Fluids* **20** (4), 046101.

Appendix A. Simulations with varying diaphragm stand-off distances

Inviscid simulations of the shock tube and obstacle were performed to assess the diaphragm stand-off distance and to gauge the effect of the driver/test gas interface on the shock reflection.

The two-dimensional domain spanned half the shock tube height, from the centre-line to the shock tube wall, five half-heights upstream of the chevron tip, and three half-heights downstream. The domain was covered by a 40×5 coarse grid with six levels of refinement for a finest possible grid of 2560×320 and resolution of 3.15 grid points per millimetre. Symmetry boundary conditions were added to every cell within the chevron, creating a step-like boundary. Step boundaries have been shown to affect the shock reflection configuration (Ben-Dor *et al.* (1987)), but perform decently (Falle & Giddings (1992)) with sufficient dissipation (controlled here by low resolution). The top and bottom boundaries employed symmetry conditions, and the left and right boundary had zero normal gradients. The origin is located at the trailing edge of the chevron. The simulations were initiated with a shock strength of M_{t} located at $\hat{x}_{\mathrm{s},0} = -15.24$ cm. The driver gas was initiated at a distance $\hat{x}_{\mathrm{d},0} = \frac{u_{\mathrm{t}}}{D_{\mathrm{t}}}(\hat{x}_{\mathrm{s},0} - \hat{l}_{\mathrm{d}}) + \hat{x}_{\mathrm{s},0}$, where $D_{\mathrm{t}} = M_{\mathrm{t}} c_0$ is the transmitted shock speed and u_{t} is the shocked particle speed. The driver gas has the same pressure and velocity as the shocked gas, but with a density of $2\rho_0$.

Experiment 9 (see table 1, $M_{\mathrm{c}} = 3.4$ and $\gamma = 1.06$) is simulated because it is the most compressible (*i.e.* highest Mach number and lowest isentropic exponent) of all experiments with a stand-off of $\hat{l}_{\mathrm{d}} = 1.85$ m. If this experiment is unaffected by the driver/test gas interface, then so are all the other experiments where $1.06 \leqslant \gamma_0$, $M_{\mathrm{c}} \leqslant 3.4$, and $\hat{l}_{\mathrm{d}} = 1.85$ m. A shock strength of $M_{\mathrm{t}} = 4.2$ is required to generate a shock wave of $M_{\mathrm{c}} = 3.4$ on the chevron.

The simulation results are presented in figures 24. The figures show pseudo-schlieren images (symmetric logarithmic horizontal density gradients) on the top halves. Dark lines show decreases in density from left to right, while bright lines indicate the opposite. The bottom halves show temperature non-dimensionalized by the quiescent conditions and cutoff at $T = 1.6$ to emphasize details of the reflection. The x and y coordinates are scaled in metres.

Figure 24a shows the flow field after a shock has been transmitted through the diaphragm, before it interacts with the chevron obstacle. The driver/test gas interface is overlayed with a dotted red line. The shock diffracts over the chevron and reaches the trailing edge in figure 24b. The driver/test gas interface remains far behind the shock front, showing it does not cause of the textured appearance of the schlieren in figure 6d. The shock wave reflects from the axis of symmetry, forming a double Mach reflection with Mach stem bifurcation, as shown in figure 24c. The driver gas has diffracted over the obstacle, driving pressure a wave towards the front. The driver/test gas interface induces a complex flow field that is absent from the experiments (figure 6e, meaning the driver/test gas interface is even further removed. When there is no driver/test gas interface, as in figure 25a, the front of the shock reflection is identical that of figure 24c in so far as triple points, incident and reflected shocks, forward jet, Mach stem bulging, or bifurcation are concerned, further showing the driver/test gas interface does not interfere with the reflection front.

Figure 25 is a simulation of experiment 11 ($M_c = 4.0$ and $\gamma = 1.06$) where the stand-off distance was shortened to $\hat{l}_d = 0.68$. Reducing the stand-off accelerates the shock to $M_c = 4.0$ by the end of the chevron. The driver/test gas interface is closer to the shock front, the double Mach reflection has a prominent forward jet, and a Mach stem that is clearly bifurcated and taller than the previous case, despite the higher Mach number. The bow shock (secondary Mach shock) travels much faster through the hot driver gas than through the diffracted/shocked, forming a vertical shock.

These simulations demonstrate that the driver/test gas interface has no effect on the experiments with $\hat{l}_d = 1.85$, and that only experiments 10 and 11, where $\hat{l}_d < 1.85$, suffer from interference by the driver gas.

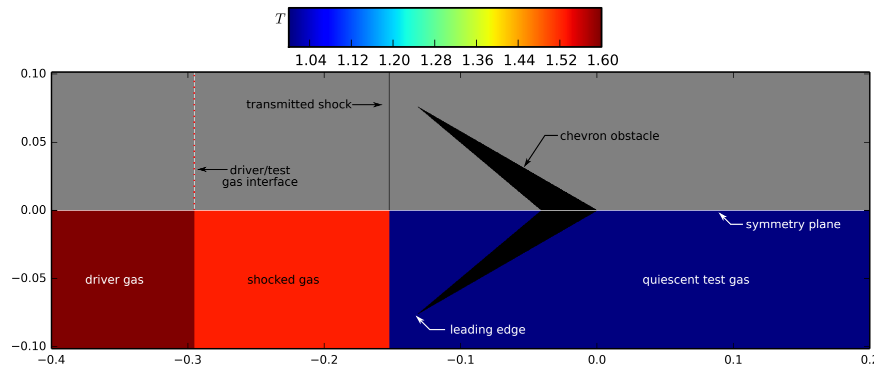

(a) Initial condition, before shock interaction with chevron

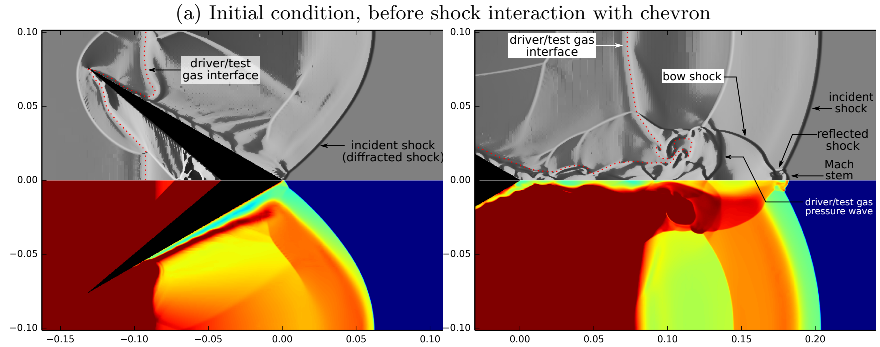

(b) Shock diffracting over chevron (c) Shock reflection from plane of symmetry

Figure 24: Inviscid simulation of shock reflection over a chevron ($\gamma = 1.06$, $M_c = 3.4$, $\hat{l}_d = 1.85$ m); top: pseudo-schlieren; dotted red line: driver/test gas interface; bottom: temperature; axes scaled in metres

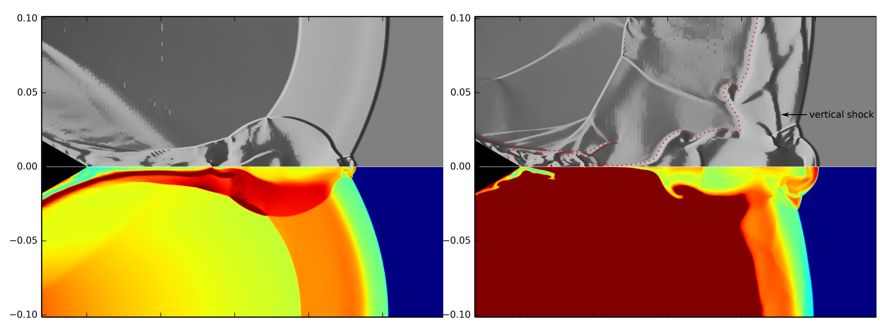

(a) $M_c = 3.4$, no driver/test gas interface (b) $M_c = 4.0$, $\hat{l}_d = 0.68$ m

Figure 25: Inviscid simulations of shock reflection over a chevron ($\gamma = 1.06$); top: pseudo-schlieren; dotted red line: driver/test gas interface; bottom: temperature; axes scaled in metres

Chapter 2

Detonation dynamics predicted by the Fickett-Majda model

2.1 Simplified detonation models

The Navier-Stokes equations 1.13 are often simplified by removing diffusion terms in the study of detonations, becoming the Euler equations

$$\begin{aligned}\frac{\partial\hat{\rho}}{\partial\hat{t}} + \vec{\nabla}\cdot(\hat{\rho}\hat{\vec{u}}) &= 0\\ \frac{\partial(\hat{\rho}\hat{\vec{u}})}{\partial\hat{t}} + \vec{\nabla}\cdot(\hat{\rho}\hat{\vec{u}}\hat{\vec{u}}) + \vec{\nabla}\hat{p} &= 0\\ \frac{\partial(\hat{\rho}\hat{E})}{\partial\hat{t}} + \vec{\nabla}\cdot\left((\hat{\rho}\hat{E}+\hat{p})\hat{\vec{u}}\right) &= 0\end{aligned} \tag{2.1}$$

with density ρ, time t, velocity $\vec{u}$, pressure p, and total energy

$$\hat{E} = \frac{\hat{p}}{\hat{\rho}(\gamma-1)} + \frac{1}{2}\hat{\vec{u}}\cdot\hat{\vec{u}} + \hat{Q}\Lambda \qquad \text{with ideal gas law} \qquad \hat{p} = \hat{\rho}\hat{R}_{\mathrm{s}}\hat{T}. \tag{2.2}$$

for a calorically perfect gas with constant isentropic exponent γ, specific gas constant R_{s}, and temperature T. The circumflex accent represents dimensional values. The inclusion of specific heat release Q with a reaction progress variable Λ, increasing from $\Lambda = 0$ in reactants to $\Lambda = 1$ in products, adds chemical heat release to the system, making the reactive Euler equations. The way it is included above hints at the possible simplification of reaction rates. Detailed chemistry require complex chemical mechanisms which can be expensive to include in calculations, so the heat release is often reduced to a simpler form which mimics the global behaviour of heat release by reactions. A popular chemistry simplification is the one step Arrhenius model with a reaction rate

$$\hat{r} = \frac{\mathrm{D}\Lambda}{\mathrm{D}\hat{t}} = \hat{k}\Lambda\exp\left(\frac{-\hat{E}_{\mathrm{a}}}{\hat{R}_{\mathrm{s}}\hat{T}}\right)$$

where $\frac{\mathrm{D}\square}{\mathrm{D}t} = \frac{\partial \square}{\partial t} + \vec{u} \cdot \vec{\nabla} \square$ is the material derivative of a variable $\square$ (square), $\hat{E}_\mathrm{a}$ is the activation energy and k is a pre-exponential factor used for scaling. Another simplified chemical model is the two step induction-reaction model [83]. It begins with a thermally neutral induction period during which no heat is released and whose rate often has Arrhenius sensitivity, and is followed by a heat releasing reaction period. More complicated models exist, including the three step chain-branching model [84,85], reduced and full chemistry models. Analysis of the reactive Euler quickly becomes unwieldy as the chemistry models become complicated. However, the Euler equations themselves can be difficult to work with, so a model which can recreate the complex behaviour of detonations, while being simpler, may help illuminate open questions regarding detonation initiation and propagation.

The reactive Euler equations can be simplified using asymptotic expansions, done by Clavin and Williams [86] and Faria *et al.* [87] for detonations, along with similar work by others [88]. The following expansion will parallel the work of Faria *et al.* [87], but start from the reactive Euler equations instead of the Navier-Stokes equations and in only one dimension.

The space and time variables are first put into a moving frame of reference and non-dimensionalized by

$$x = \frac{\hat{x} - \hat{D}_0 \hat{t}}{\hat{x}_0} \qquad \text{and} \qquad \tau = \frac{\hat{t}}{\hat{t}_0}$$

where $\hat{D}_0$ is some typical wave speed, the state variables are non-dimensionalized by the ambient state (subscript 'a'), and velocity by $\sqrt{\hat{p}_\mathrm{a}/\hat{\rho}_\mathrm{a}}$. With the small parameter $\epsilon = \hat{x}_0/(\hat{t}_0\sqrt{\hat{p}_\mathrm{a}/\hat{\rho}_\mathrm{a}})$ introduced and after non-dimensionalization, the one-dimensional reactive Euler equations become

$$\begin{aligned} \rho_\tau + \frac{1}{\epsilon}\left(\rho(u - D_0)\right)_x =& 0, \\ (\rho u)_\tau + \frac{1}{\epsilon}\left(\rho u(u - D_0) + p\right)_x =& 0, \\ (\rho e)_\tau + \frac{1}{\epsilon}\left(\rho e(u - D_0) + pu\right)_x =& 0, \\ \Lambda_\tau + \frac{1}{\epsilon}(u - D_0)\left(\Lambda\right)_x =& r \end{aligned} \tag{2.3}$$

for some appropriate reaction rate r, and subscripts x and τ representing their corresponding partial derivatives. The non-dimensionalized state variables are then expanded as

$$\begin{aligned} \rho =& 1 + \rho_1\epsilon + \rho_2\epsilon^2 + \mathcal{O}(\epsilon^3) \\ T =& 1 + T_1\epsilon + T_2\epsilon^2 + \mathcal{O}(\epsilon^3) \\ p =& 1 + p_1\epsilon + p_2\epsilon^2 + \mathcal{O}(\epsilon^3) \\ u =& u_1\epsilon + u_2\epsilon^2 + \mathcal{O}(\epsilon^3) \\ \Lambda =& \lambda + \mathcal{O}(\epsilon) \end{aligned}$$

and assumptions [86, 87] are made on the relative size of the following terms:

1. The Newtonian limit $\gamma \to 1$ is taken and the substitution $\gamma - 1 = \gamma_1 \epsilon$ is made (with $\gamma_1 = \mathcal{O}(1)$);

2. Heat release Q is assumed to be weak and the substitution $(\gamma - 1)Q/\gamma = q\epsilon^2$ is made, taking the Newtonian limit into consideration; and

3. The reaction rate is assumed to be $r = \omega/\epsilon$ (with $\omega = \mathcal{O}(1)$) so it may affect the flow at leading order.

Note that the reaction progress variable is expanded only to leading order because the weak heat release assumption is made. Substituting the expansions and assumptions into the non-dimensionalized one-dimensional reactive Euler equations, eliminating pressure using the ideal gas law, and collecting terms of like size of order ϵ and larger ($\mathcal{O}(1)$ for the reaction progress) yields

$$
\begin{aligned}
(-D_0\rho_{1x} + u_{1x}) + \epsilon(\rho_{1\tau} - D_0\rho_{2x} + u_1\rho_{1x} + u_{2x} + \rho_1 u_{1x}) &= \mathcal{O}(\epsilon^2),\\
(-u_{1x}D_0 + \rho_{1x} + T_{1x}) + \epsilon(u_{1\tau} + u_{1x}u_1 - u_{2x}D_0 - \rho_1 u_{1x} D_0 + \rho_{2x} + (\rho_1 T_1)_x + T_{2x}) &= \mathcal{O}(\epsilon^2),\\
(-D_0 T_{1x}) + \epsilon\left(T_{1\tau} - D_0 T_{2x} + u_1 T_{1x} - D_0\rho_1 T_{1x} + \frac{\gamma_1}{\gamma}D_0(\rho_{1x} + T_{1x}) + qD_0\lambda_x\right) &= \mathcal{O}(\epsilon^2),\\
(-D_0\lambda_x - \omega(\lambda, T)) &= \mathcal{O}(\epsilon),
\end{aligned}
$$

for the conservation of mass, momentum, and energy, and the reaction progress equation. Balancing the leading-order terms of the first three equations shows

$$
\begin{bmatrix} -D_0 & 1 & 0 \\ 1 & -D_0 & 1 \\ 0 & 0 & -D_0 \end{bmatrix}
\begin{bmatrix} \rho \\ u \\ T \end{bmatrix}_{1x} = \begin{bmatrix} 0 \\ 0 \\ 0 \end{bmatrix}
$$

which necessitates $D_0 = \pm 1$. Assuming $D_0 = 1$ for a right-travelling wave, the first equation can be integrated $\rho_1 = u_1 + C(\tau)$. The asymptotic expansion must be valid in the quiescent state, where the flow is assumed uniform and without perturbations ($\rho_1 = 0$ and $u_1 = 0$), meaning the integration constant is $C(\tau) = 0$, thus

$$
u_1 = \rho_1. \tag{2.4}
$$

The same argument follows for the third equation

$$
T_1 = 0.
$$

The reaction progress equation simply gives

$$
\lambda_x = -\omega.
$$

Balancing terms at order ϵ

$$
\begin{aligned}
\begin{bmatrix} -D_0 & 1 & 0 \\ 1 & -D_0 & 1 \\ 0 & 0 & -D_0 \end{bmatrix}
\begin{bmatrix} \rho \\ u \\ T \end{bmatrix}_{2x} &= \begin{bmatrix} -\rho_{1\tau} - u_1\rho_{1x} - \rho_1 u_{1x} \\ -u_{1\tau} - u_{1x}u_1 + \rho_1 u_{1x} D_0 - (\rho_1 T_1)_x \\ -T_{1\tau} - u_1 T_{1x} + D_0 \rho_1 T_{1x} - \frac{\gamma_1}{\gamma} D_0(\rho_{1x} + T_{1x}) - qD_0\lambda_x \end{bmatrix} \\
&= \begin{bmatrix} -u_{1\tau} - 2u_1 u_{1x} \\ -u_{1\tau} \\ -q\lambda_x - \frac{\gamma_1}{\gamma} u_{1x} \end{bmatrix}
\end{aligned}
$$

by simplification with leading order results and with $D_0 = 1$. Adding the first two equations and equating the result with the third equation yields

$$2u_{1\tau} + 2u_1 u_{1x} = -\,q\lambda_x - \frac{\gamma_1}{\gamma} u_{1x}.$$

Rescaling this equation by letting

$$x_{\text{rescaled}} = x - \frac{1}{2}\frac{\gamma_1}{\gamma}\tau, \qquad t_{\text{rescaled}} = \tau, \qquad \text{and} \qquad u_{\text{rescaled}} = u_1,$$

transforms the equation to (dropping the "rescaled" subscript)

$$u_t + \left(\frac{1}{2}u^2 + \frac{1}{2}\lambda q\right)_x = 0 \qquad \text{with reaction rate} \qquad \lambda_x = -\omega. \tag{2.5}$$

The nomenclature may seem confusing since the simplified model uses the same symbols as the Euler equations, despite having suffered two rescalings and a change of reference. This has been done to facilitate analogies between the simplified model and the Euler equations, and in an attempt to be consistent with literature in both fields. The remaining work will be qualitative in nature so the meaning of variables will be important but the exact scaling will not.

This single hydrodynamic equation above has been used as a simplified model for detonations, originally by Fickett [89,90] and Majda [91]. It is essentially Burgers' equation [92] with an added source term λq that takes care of energy release, but the rate equation ω remains to be defined. The task of choosing an appropriate reaction model that allows the desired behaviour without being too complex remains.

Burgers-type equations are present in many other hyperbolic systems, and variations of this simplified model differ in how the reaction rate equations are chosen. Fickett [89] has written an intuitive description of the system. The local state variable u may be interpreted as density or sound speed, and u and ρ are interchangeable, owing to equation 2.4, with Fickett [89] having used ρ and others choosing u instead. The analogue of pressure is $p = u^2/2 + \lambda Q$. The system allows waves to steepen into shock waves due to wave speed dependence on the local state, and expansion waves are also possible.

The simplified models differ from the Euler equations in the number of characteristic waves they have. The Euler equations have three families of characteristic waves: forward- and backward-travelling characteristics (along $\frac{\mathrm{d}x}{\mathrm{d}t} = u \pm c$, where u is the local particle velocity and c is the sound speed), and one on the particle path (the entropy wave, along $\frac{\mathrm{d}x}{\mathrm{d}t} = u$). The simplified models have only two families of waves: there is one forward-running characteristic along $\frac{\mathrm{d}x}{\mathrm{d}t} = u$, and a particle path. The reaction rate varies in space (λ_x), yielding particle characteristics which are horizontal in the x-t plane and travel infinitely fast to the rear. The removal of one characteristic makes the simplified models much simpler to analyse than the Euler equations. In Fickett's detonation analogue [89], the reaction rate is chosen to vary with time, λ_t being the reaction rate, resulting in a particle path along $\frac{\mathrm{d}x}{\mathrm{d}t} = 0$ which is a vertical line in the x-t plane. Although not asymptotically correct, it is an analogue that behaves the same way in many respects.

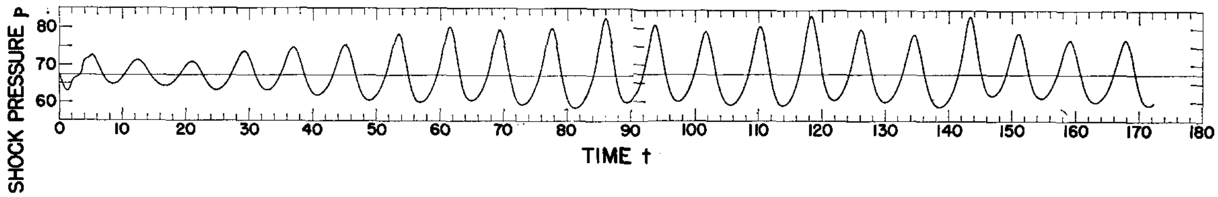

Figure 2.1: Shock pressure history of a one-dimensional pulsating detonation (numerical simulations of the Euler equations) [94]

The asymptotic models and analogues are able to recover many aspects of detonations, such as the speed and structure of detonations found with the Euler equations. In both systems, over- and under-driven detonations relax to a steady profile due to attenuation or amplification waves reaching the front from the rear. Once steady state is reached, the detonation becomes immune to perturbations from the back, and travels at a speed controlled by the net amount of heat released before the flow reaches a critical sonic point, explained further in the next section. In addition to similar steady state behaviour, more complicated non-linear behaviour of the reactive compressible Euler equations can also be reproduced by simplified models. Analysis [93] and numerical simulations [94] of the reactive Euler equations have shown that one-dimensional detonations can become unstable with generally three types of pulsating instabilities: periodic, chaotic and galloping. Periodic oscillations in detonation speed and thus the shocked state shown in figure 2.1 may manifest for gases with large activation energy [93]. As activation energy is increased, the regular oscillations in speed undergo a period-doubling bifurcation cascade [95] to chaos [96, 97]. When the propagation limits are approached, galloping detonations are observed, with a lead shock that travels near quenching velocities for long periods, punctuated by rapid accelerations of the detonation front above the Chapman-Jouguet speed, followed by a slower deceleration back to nearly quenched velocities. Numerical simulations of the simplified models have revealed a similar sensitivity to activation energy [98], path to chaos [99, 100], and galloping-like behaviour [101]. Even the multidimensional cellular instability of detonations [87] can be recovered. Asymptotic modelling of Fickett's analogue [102, 103] has also shown period doubling bifurcations, chaotic oscillations, and galloping detonations [104], while the complexity of the Euler equations limited equivalent asymptotic modelling [105] to low order solutions which only yielded single-period oscillations.

Simplified models of detonations have proven to be a useful tool for gleaming information about the complicated dynamics of detonations, and they will be used here to explore the detonation dynamics of hybrid detonations using Fickett's detonation analogue, where the presence of multiple reactions obscures the detonation dynamics.

2.2 Hybrid detonations

Aspects of steady-state detonations in the Euler equations will now be reviewed to highlight complications that arise from the presence of multiple disparate energy sources present in hybrid detonations, in comparison to more traditional single-phase gas detonations. The ability of simplified models to qualitatively reproduce the steady speed and profiles of detonations will then be leveraged to study hybrid detonations in section 2.3.

The Chapman-Jouguet (steady-state) detonation speed can be found analytically in some cases of the Euler equations, such as perfect gases with simple chemistry models, by investigating the Rayleigh line and Hugoniot curves of the system. This paradigmatic analysis is found in many detonation textbooks [1, 106]. The Chapman-Jouguet Mach number M_{CJ} is found approximately by considering the detonation to be a discontinuity that brings the gas to an equilibrium with products that are sonic with respect to the front. For an ideal detonation through a calorically perfect gas, the Mach number becomes a function [1] of heat release q, the isentropic exponent γ, and initial conditions. The sonic condition in the products of the Chapman-Jouguet solution prevents acoustic signals originating behind it from disturbing the shock front.

The Chapman-Jouguet approximation performs well in many cases, but deviates in non-ideal ones where the mole number varies or losses are present, for example. Improvement on the Chapman-Jouguet condition requires looking at the internal structure of a steady state detonation, lying between the sonic plane and shock front. The one-dimensional detonation structure is found by integrating the one-dimensional reactive Euler equations in the detonation's frame of reference, known as the Zel'dovich-von Neumann-Döring (ZND) equations [1, 106]

$$\begin{aligned} \frac{\mathrm{d}\rho}{\mathrm{d}x} &= -\frac{\rho}{u}\frac{\mathrm{d}u}{\mathrm{d}x} \\ \frac{\mathrm{d}p}{\mathrm{d}x} &= -\rho u\frac{\mathrm{d}u}{\mathrm{d}x} \\ \frac{\mathrm{d}u}{\mathrm{d}x} &= u\frac{\dot{\sigma}}{1-M^2} \end{aligned} \tag{2.6}$$

where ρ is density, p is pressure, u is the flow velocity, M is the local Mach number, x is position, and $\dot{\sigma}$ is the effective rate of heat release known as thermicity

$$\dot{\sigma} = \sum_i^{\text{species}} \left(\frac{W}{W_i} - \frac{h_i}{c_p T}\frac{\mathrm{d}Y_i}{\mathrm{d}t} \right)$$

for an ideal gas (shown here without losses), with W as the molecular weight, h as enthaply, c_p as the specific heat at constant pressure, T as temperature, Y_i as the mass fraction of the i^{th} specie, and t as time. Reaction rates $\frac{\mathrm{d}Y_i}{\mathrm{d}t}$ are required to complete the system. The equations are integrated from the post-shock conditions, along with the chemical kinetic equations, to reveal the detonation profile. The Zel'dovich-von Neumann-Döring equations 2.6 become singular when the sonicity $1-M^2$ reaches zero, where flow becomes sonic with respect to the lead shock, unless the thermicity reaches zero simultaneously. This is known as the generalized Chapman-Jouguet condition. It suggests that in the presence of losses which reduce the effective rate of heat release, the net thermicity (*i.e.* with the inclusion of losses) may reach zero before the completion of chemical reactions, so a valid solution may exhibit a sonic plane before all the chemical energy has been released. The sonic plane prevents heat released or lost behind the sonic plane from affecting the detonation front. The detonation speed becomes dependant on the energy released between the shock and sonic point. This is known as an eigenvalue detonation and its structure and behaviour are reproduced by simplified models [90, 107].

An example of a perfect gas detonation with losses [1] is shown in figure 2.2. The profiles are non-dimensionalized by their unshocked values and the half-reaction length. An irreversible Arrhenius reaction is chosen for the heat release rate, losses are modelled by a friction body force $c_f \rho u|u|$, and the detonation is marginally over-driven to avoid a singularity at the sonic plane. The plot in figure 2.2a shows how flow properties immediately behind the shock, on the right, change as reactions proceed towards the left, and as losses become more important. Figure 2.2b shows how the exothermic reactions compete with friction losses, reaching a point near $x \approx -1.3$ where the losses perfectly balance heat release, before reactions finish. This point coincides with (nearly) vanishing sonicity and corresponds to the generalized Chapman-Jouguet condition. Only the net energy release between the shock and the sonic plane contribute to the detonation speed.

If thermicity is allowed to reach zero multiple times, due to the presence of multiple separated reactions, as is the case in hybrid detonations for instance, it is plausible that the generalized Chapman-Jouguet condition also be satisfied multiple times and it becomes unclear which instance controls the detonation speed.

Hybrid detonations travel through mixtures of reactive gases with suspended reactive particles. An illustration of a hybrid detonation is shown in figure 2.3. A shock wave passes through a reactive dusty gas, suddenly compressing, heating, and imparting flow to the gas. Momentum and heat are transferred to the particles due to the velocity and temperature difference between the shocked gas and particles, increasing the gas pressure and sapping energy from the gas phase. The gas quickly reacts and expands, following a short induction time, while the particles continue to equilibrate with the gas. Once the particles reach an ignition threshold, they begin reacting and releasing energy back into the flow, resulting in two sequential reaction zones [108–110].

Experiments and numerical studies using continuum models, constituted of mass, momentum, and energy equations for each phase linked by sources, have revealed multiple quasi-steady velocities for hybrid detonations, and even the existence of internal shocks [108, 109, 111–113] which were transient in some cases and steady in others. The selection rules for the velocity have remained uncertain. Experiments and simulations in hybrid systems have suggested that a double reaction zone structure is possible, with an embedded shock located between two sonic planes. It is presently unclear if such a shock is stable.

The problem is essentially one of modelling reactive multiphase flows. Many methods have been used [114, 115], with interest ranging from spray combustion, reactive granular materials, to reactive dusty gases. This proposed research will focus on hybrid detonations where much work has been done using a continuum type of model, similar to that in

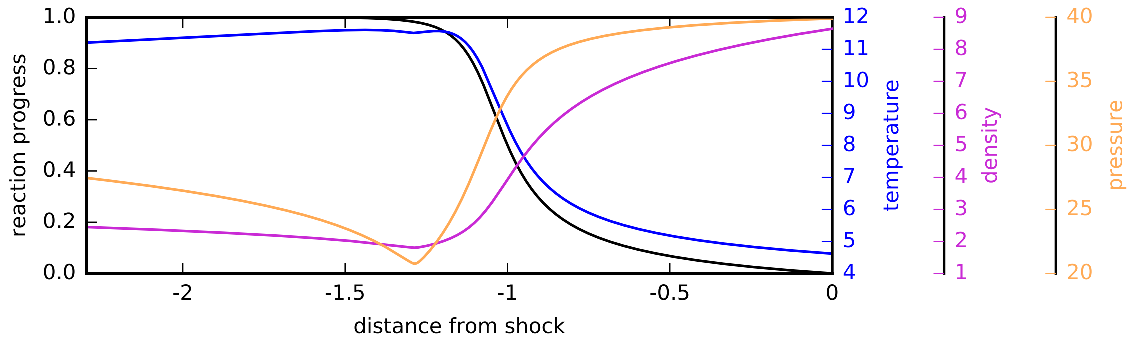

(a) State properties

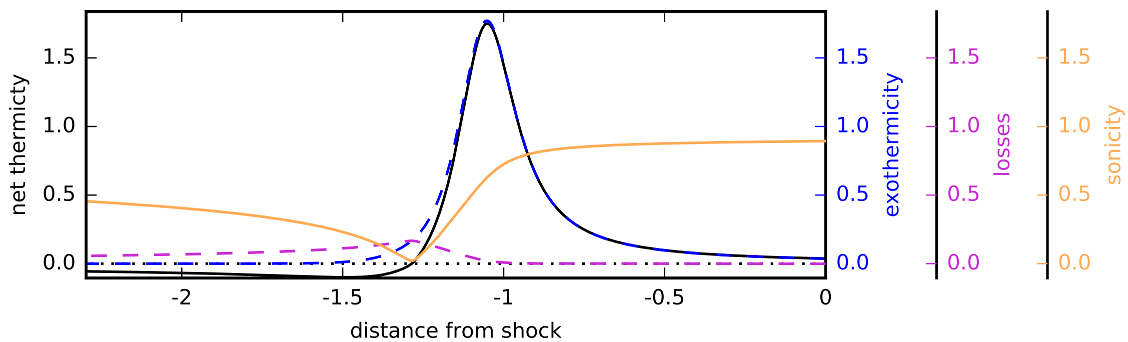

(b) Competing factors

Figure 2.2: Zeldovich-von-Neumann-Döring detonation profiles for a marginally over-driven calorically perfect gas detonation ($M = 6.63325$, $\gamma = 1.2$, $Q/RT_0 = 50$, $E_\mathrm{a}/RT_0 = 50$) with friction losses ($c_f = 0.004$)

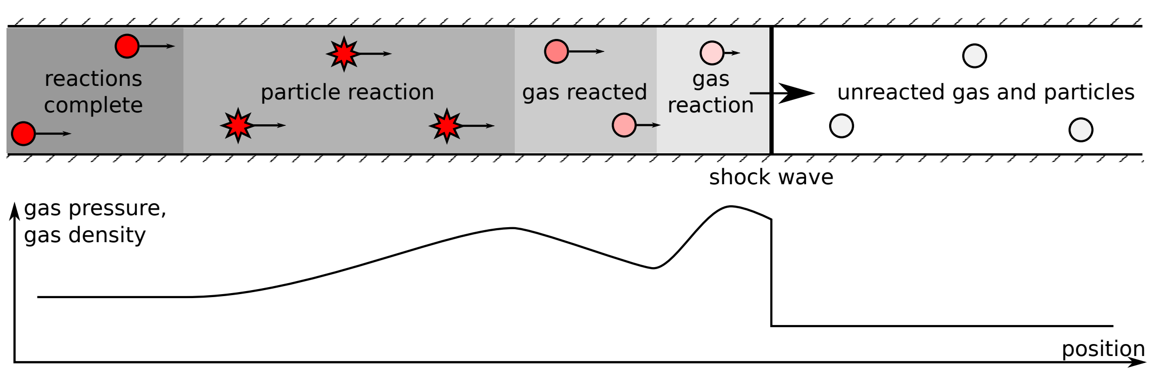

Figure 2.3: Illustration of a steady one-dimensional hybrid detonation, travelling from left to right, with particle velocities related to arrow size, and temperature to redness; typical gas pressure and gas density profile below

a review on the state-of-the-art of detonations through particle-laden gases written by Zhang [112].

In Marble's review article [116], dusty gases were modelled using modified Euler equations. The gas and particles phases were differentiated by their own set of mass, momentum and energy equations. Particles of the same size, shape and density were assumed to be dilute enough as to ignore each other and to be locally subjected to the same forces and velocities, therefore exhibit no pressure or viscous effects between each other. Miura and Glass [117–119] with Saito [120, 121] used the same approach to perform thorough numerical simulations and analysis of shocks in dusty gases.

This type of model has been used by Veyssiere and Khasainov [111, 122] who studied steady hybrid detonations using the reactive Euler equations, with one phase dedicated to the gas phase and others to the solid phase. The phases were coupled through source terms in the energy and momentum equations.

They sought to model gaseous explosives with aluminium particle suspensions [122]. The shock frame of reference in one dimension was used. The particles distribution was composed of finite groups of constant-diameter particles, each with their own identical set of equations. The total number of particles was conserved and interacted only (directly) with the gas phase through source terms. Mass was transferred to the gas phase when the particle temperature crosses an ignition threshold, momentum was transferred through drag on the spherical particles [123], and heat exchange occurred through convection and radiation between particles and gas. In their model, the particles remained inert while they melted and boiled until the temperature reached an ignition threshold, taking flow stagnation into account, after which the particles burnt following an empirical law. The gas phase was modelled using the Euler equations. In addition to the mass, momentum and energy exchanges with the particles phases, friction between gas flow and the wall was included and the gas reactions followed a two step model. Their results are summarized in the next section.

Despite many assumptions and simplifications, the model is complicated and difficult to analyse. This presents a good opportunity to use a simplified model to try and clarify the reasons for the multiple quasi-steady detonation speeds, how the final detonation velocity is chosen, and how internal shocks arise. Fickett's detonation analogue will be used with three source terms: two sequential reactions to mimic the gas and particle reactions, and one loss to mimic the momentum and heat transfer from the gas to the particles.

2.3 Multiplicity of detonation regimes in systems with a multi-peaked thermicity

Authors: S. SM. Lau-Chapdelaine, F. Zhang, M. I. Radulescu.

Status: The paper was submitted for peer review on October 3rd, 2018. Reviews were received on 17 December, 2018. A revised version of the paper is presented below. The paper is under review as of the submission of this thesis.

The model was presented by Radulescu in 2013 at the 24th International Colloquium on the Dynamics of Explosions and Reactive Systems in Taipei, Taiwan, and subsequent work was presented by Lau-Chapdelaine in 2014 at the 15th International Detonation Symposium in San-Francisco, United States of America.

Coauthor contributions: The work was inspired and funded by Dr Zhang of Defence Research and Development Canada whose insight was useful in guiding the work.

ARTICLE TEMPLATE

Multiplicity of detonation regimes in systems with a multi-peaked thermicity

S. SM. Lau-Chapdelaine[a], F. Zhang[b], and M.I. Radulescu[a]

[a]Department of Mechanical Engineering, University of Ottawa, Ottawa, Ontario, Canada, K1N 6N5; [b]Defence Research and Development Canada, Medicine Hat, Alberta, Canada, T1A 8K6

ARTICLE HISTORY

ABSTRACT

The study investigates detonations with multiple quasi-steady velocities that have been observed in the past in systems with multi-peaked thermicity, using Fickett's detonation analogue. A steady state analysis of the travelling wave predicts multiple states, however, all but the one with the highest velocity develop a singularity after the sonic point. Simulations show singularities are associated with a shock wave which overtakes all sonic points, establishing a detonation travelling at the highest of the predicted velocities.

Under a certain parameter range, the steady-state detonation can have multiple sonic points and solutions. Embedded shocks can exist behind sonic points, where they link the weak and strong solutions. Sonic points whose characteristics do not diverge are found to be unstable, and to be the source of the embedded shocks. Numerical simulations show that these shocks are only quasi-stable. This is believed to be due in part to a feature of the model which permits shocks anywhere behind a sonic point.

KEYWORDS

Hybrid detonations; Detonations; Shock Waves; Simplified models; Fickett's detonation analogue;

1. Introduction

The decomposition of certain reactive materials can occur in two or more distinct steps, characterized by multiple peaks in the thermicity (effective rate of energy release). Nitromethane-air detonations [1] and other usual fuels using NO_x as oxidizer [2] give rise to such multiple reaction zone detonation structures. Thermo-nuclear fusion reactions also occur in sequential steps. Detonations in degenerate white dwarfs undergoing supernova explosions of the Type Ia have three sequential steps where carbon, oxygen, and silicon undergo fusion [3]. Hybrid detonations are self-sustained detonation waves in reactive gas mixtures with suspended reactive dust and display two sequential reaction zones in the detonation structure [4–6]. The gas phase reaction first proceeds with influence from the solid phase, including energy used to heat the particles, and momentum lost to the solid phase by entraining the particles with the gas flow. The solid phase reacts exothermically once it has absorbed sufficient energy.

CONTACT S. SM. Lau-Chapdelaine. Email: –

A common feature of multi-peaked thermicity [7] systems is the presence of endothermic processes coupling the multiple reactions. These losses can be manifested by heat and momentum losses to confining walls, mass divergence, or curved geometries. Losses can also be intrinsic to the system, as they are in hybrid detonations, for example, where particle heating and drag withdraw energy from the gas phase. Experiments and numerical simulations in these hybrid systems have shown that the selection rules and detonation wave pressure profiles depend intimately on the kinetics of the reactions in either phase, the amount of energy release, and hydrodynamic resistance of the particles to the gas phase motion; Zhang's recent review [8] provides the state-of-the-art.

In systems with simultaneous exothermic and endothermic processes, the competition between energy addition and loss dictate the structure of the self-sustained wave [9]. Self-sustained, steady travelling detonations with losses have a surface of zero net thermicity within their reaction zone, where energy release is balanced by losses. This surface is sonic with respect to the detonation front, in order to avoid a singularity in the solution, and information beyond it is unable to reach the front. The detonation's velocity is therefore only influenced by the accumulated energy release between the lead shock and this sonic surface. The conditions governing the propagation velocity of detonations with losses are known as the "generalized Chapman-Jouguet (CJ)" conditions and are treated at length in most detonation textbooks [7, 10].

In systems with multiple thermicity peaks, it is plausible that the generalized CJ condition be met multiple times, and it is unclear what governs the speed of the lead shock. Previous investigations have examined the solutions of detonations with multiple exothermic reactions and simultaneous losses.

Veyssière and Khasainov [11–13] numerically studied steady hybrid detonations using two-phase reactive Euler equations. They found three steady propagation regimes. One regime was driven solely by the gas reaction while particles remained inert in the driving region. The second regime had both gas and particle reactions driving the detonation front, consequently travelling faster than previous regime. Finally, the third regime was steady only under certain parameters. At these specific parameters, the detonation propagated at the same velocity as the first regime, however, they found a shock wave embedded within the reaction zone. For other sets of parameters, the embedded shock eventually overtook the detonation front and the velocity increased to that of the second regime, where reactions from the gas and solid phases drove the detonation together.

Bdzil et al. [14] investigated a two-reaction case with losses due to shock curvature, using asymptotic expansions of the reactive Euler equations. They found a range of curvatures (losses) where two quasi-steady detonation velocities were possible. Time-evolution of a blast-initiated detonation showed that, with certain initial conditions, the blast would decay such that the flow would adopt the slower detonation velocity, then in some cases abruptly transition to the fast solution.

A multiplicity of steady velocity solutions for detonations with multi-peaked thermicity were found in these studies, some unstable. Internal shocks were found to be transient in some cases and steady in others. The selection rules for the detonation structure and velocity, however, remain unclear. This is partially because the origin and transient of the internal shocks is uncertain.

This investigation aims to clarify the steady reaction zone structure and velocity of detonations with multi-peaked thermicity. Solutions and selection rules for situations where two sonic planes propagate at different speeds will be explored. The case where the two sonic planes propagate at the same velocity is complex and poorly understood and will also be studied. Experiments and simulations in hybrid systems [4, 5, 8, 12, 15] have suggested that a double reaction zone structure is possible, with an embedded shock located between two sonic planes. It is presently unclear if such a shock is stable, if it depends on external losses, as modelled by previous authors, or is dependent on other three-dimensional effects in the experiments. The wave structure of such double-structure detonations, their stability, and origin of embedded shocks will be studied analytically and numerically.

The flow-fields of detonations with losses and multiple heat releases are very complex and dependant on reaction mechanisms, viscous, turbulent, and multi-dimensional effects that can be particular to specific cases. The granularity of these effects is lost in the continuum and volume-averaged limits, however, models in these limits are still viable and provide qualitative insights on the dynamics of these hyperbolic systems. For example, Brailovsky and Sivashinsky [16, 17], Dionne et al. [18], and Semenko et al. [19] studied the multiplicity of regimes in single-reaction detonations subject to friction and convection losses. Their models were based on the one-dimensional Euler equations and assumed simple, volumetrically-averaged heat addition and losses. These continuum simplifications allowed them to qualitatively explain [16, 17] the complex multi-valued and set-valued [19] behaviours of 'low velocity' detonations in very rough or porous channels.

In the present study, we address the structure and stability of detonations with multiple peaks of thermicity using a simplified model first introduced by Fickett [20] and Majda [21] as a qualitative model for reactive gas dynamics problems. It takes the form of the reactive form of the inviscid Burgers equation

$$\frac{\partial u}{\partial t} + \frac{\partial}{\partial x}\left(\frac{1}{2}u^2 + \lambda Q\right) = 0.$$

It can be shown that the present model can be obtained from the reactive Euler equations in the Newtonian limit (the isentropic exponent approaching unity) and low heat release [22]. It applies to transonic flows in the vicinity of sonic points of detonations [23]. This makes the model directly relevant for analyzing the interplay between multiple transonic layers present in systems with multiple thermicity peaks. Note that this limit also coincides with the conditions for weakly reactive dusty gas with high dust loading [24]. This model problem is studied due to the simplicity it offers over the full reactive Euler equations in interpreting the structure and stability of detonations with multiple peaks of thermicity. The simplicity comes from the presence of a single family of non-linear propagating waves and its coupling to the thermicity.

In the past, this simplified model has found great utility in understanding dynamic phenomena involving detonations, such as their one-dimensional and two-dimensional stability [25–28], dynamics of heterogeneous detonations [29], detonation initiation [30] and the eigenvalue structure and limits in the presence of losses [31, 32]. The present study extends this substantive body of work to reactive systems with multiple thermicity peaks. While the authors recognize the limitations of this simplified model, it is stressed that the present study serves as a stepping stone to the investigation of the full set of reactive multi-phase Euler equations modelling the problem of multi-phase hybrid detonations with multi peaks in thermicity, a problem the authors gauge as being too complex to tackle head-on. The full problem will be addressed in a sequel.

The paper is organized as follows. The mathematical model to be solved is given in section 2. The possible steady travelling wave solutions, akin to the Zeldovich-von Neumann-Döring structure are presented in section 3. Integral curves of the steady solution are studied, and a Hugoniot-Rayleigh analysis is performed in section 4. Unsteady numerical simulations of the model are then presented; the method is described in section 5 and the results are shown in 6. Solutions, stability, and selection rules are then discussed in section 7 in light of the analytical and numerical results. The conclusions are summarized in section 8.

2. Model: Reactive Burgers equation

The formulation follows closely that of Fickett [20, 31], along with the interpretation of the different terms. The hydrodynamic model is

$$\partial_t \rho + \partial_x p = 0 \tag{1}$$

where x is a Lagrangian coordinate, t is time, ρ represents density, and p is the mass flux but serves as the analogue to pressure, by which it will be referred to in the remainder of this article. In this study, the equation of state

$$p = \frac{1}{2}\left(\rho^2 + \sum_i \lambda_i Q_i\right) \tag{2}$$

is used, where λ_i are the reaction progress variables which range from zero (unreacted) to one (reacted). The constants Q_i represent the heat release when positive, and losses when negative.

Two sequential exothermic reactions (subscripts 1 and 2) and one loss (subscript 3) are considered with state-independent rates. The first exothermic reaction and the heat loss begin once shocked, while the second reaction begins upon completion of the first reaction. Simple depletion reaction rates are chosen for the exothermic reactions while a constant rate is used for the loss

$$\begin{aligned} r_1 =& \partial_t \lambda_1 = \mathrm{H}(1-\lambda_1) k_1 (1-\lambda_1)^{\nu_1}, \\ r_2 =& \partial_t \lambda_2 = (1-\mathrm{H}(1-\lambda_1))\mathrm{H}(1-\lambda_2) k_2 (1-\lambda_2)^{\nu_2}, \text{ and} \\ r_3 =& \partial_t \lambda_3 = \mathrm{H}(1-\lambda_3) k_3, \end{aligned} \tag{3}$$

where k_i are scaling constants, and ν_i represent the reaction orders. The Heaviside function

$$\mathrm{H}(n) = \begin{cases} 0 & \text{if } n \leq 0 \\ 1 & \text{if } n > 0 \end{cases}$$

is used to toggle the reactions.

Initial conditions ahead of the wave are uniform, taking the values $p_0 = \rho_0 = \lambda_{i,0} = 0$ for simplicity and without loss of generality.

The parameters used in this study are listed in table 1. The parameters k_1, Q_1, and ν_1 correspond to the scaling constant, heat release, and reaction order of the first exothermic reaction, k_2, Q_2, and ν_2 to the subsequent exothermic reaction, and k_3 and Q_3 are for the loss. They have been chosen so that sonic points are possible for reactions 1 and 2, but their exact values and scale are otherwise arbitrary. Note the selection of $0 < \nu < 1$ allows the reaction to finish in finite time. Three cases are

Table 1. Parameter sets used in study († 1 CJ point, ‡ 2 CJ points)

case		k_1	Q_1	ν_1	k_2	Q_2	ν_2	k_3	Q_3	D_A	D_B
$D_\mathrm{A} < D_\mathrm{B}$	†	1	0.5	0.5	0.2	0.5	0.5	0.1	-0.8	0.59397	0.6
$D_\mathrm{A} = D_\mathrm{B} = D_\mathrm{AB}$	‡	1	0.5	0.5	0.2	0.4782...	0.5	0.1	-0.8	0.59397	0.59397
$D_\mathrm{A} > D_\mathrm{B}$	†	1	0.5	0.5	0.2	0.45	0.5	0.1	-0.8	0.59397	0.58784

presented in the table, corresponding to different detonation velocities D_A and D_B that will be discussed in the next section. Only the heat release of the second reaction, Q_2, is changed, and with it D_B. This model was presented by Radulescu et al. [33] for the single CJ point case and Lau-Chapdelaine et al. [34] for the two CJ point case.

3. Steady analytical solution

A travelling wave solution can be deduced when the hydrodynamic equation 1 is written in characteristic form

$$\frac{\mathrm{d}p}{\mathrm{d}t} = \sigma \text{ along } \frac{\mathrm{d}x}{\mathrm{d}t} = \rho \tag{4}$$

where thermicity is defined as

$$\sigma = \frac{1}{2}\sum_i r_i Q_i. \tag{5}$$

Figure 1 illustrates the structure of the self-supported detonation wave [26]. The detonation structure consists of pressure waves originating from the back (left), travelling along characteristics $\mathrm{d}x/\mathrm{d}t = \rho$ and amplifying according to the characteristic equation (4). The amplification is given by the local evolution of the reacting field, described by the reaction rate equations (3), along the particle paths $x =$ constant. These pressure waves coalesce and sustain a steady moving lead shock with velocity D.

In order to seek the steady structure of the travelling wave solution illustrated in figure 1, the spatial variable x is changed to a shock fixed frame $\zeta = x - Dt$ (with origin at the shock) for a detonation travelling with constant velocity D. The hydrodynamic equation (1) and reaction rate equations (3) can then be transformed into a set of ordinary differential equations

$$\begin{aligned}
\frac{\mathrm{d}\rho}{\mathrm{d}\zeta} &= \frac{1}{D}\frac{\sigma}{\rho - D}, \\
\frac{\mathrm{d}\lambda_1}{\mathrm{d}\zeta} &= -\frac{r_1}{D}, \\
\frac{\mathrm{d}\lambda_2}{\mathrm{d}\zeta} &= -\frac{r_2}{D}, \text{ and} \\
\frac{\mathrm{d}\lambda_3}{\mathrm{d}\zeta} &= -\frac{r_3}{D}.
\end{aligned} \tag{6}$$

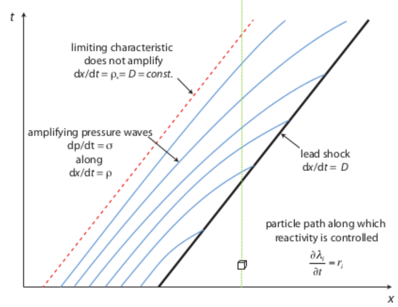

Figure 1. The structure of self-sustained detonations

Integrating these equations yields the analytical results for the wave structure

$$\rho = D \pm \sqrt{D^2 - \left(\sum_i Q_i \lambda_i\right)}, \tag{7}$$

$$\lambda_1 = 1 - \left(-\frac{k_1}{D}(\nu_1 - 1)\zeta + 1\right)^{\frac{1}{1-\nu_1}}, \tag{8}$$

$$\lambda_2 = 1 - \left(\frac{k_2}{D}(\nu_2 - 1)(\zeta_2 - \zeta) + 1\right)^{\frac{1}{1-\nu_2}}, \tag{9}$$

$$\lambda_3 = -\frac{k_3}{D}\zeta, \tag{10}$$

where $\zeta_2 = \frac{D}{k_1(\nu_1 - 1)}$ indicates where the second reaction starts, found by solving equation 8 for ζ with $\lambda_1 = 1$; the first and third reaction begin at $\zeta = 0$.

The travelling wave solution is isolated from the back when the limiting characteristic travels at the same velocity as the steady lead shock, i.e., when $\mathrm{d}x/\mathrm{d}t = \rho = D$; this is the sonic criterion. For this limiting characteristic to travel at constant speed, it also requires vanishing thermicity from the density differential equation (6). Thus the generalized Chapman-Jouguet condition, denoted with the subscript CJ, is fulfilled when

$$\rho = D \qquad \text{and} \qquad \sigma = \frac{1}{2}\sum_i r_i Q_i = 0. \tag{11}$$

The solution exhibits sonic points, with respect to the front anywhere the condition ($\rho = D$) is met . The relation between the detonation speed and the reaction, evaluated along the limiting characteristic, is obtained from the analytical relation for density (7) when the sonic portion of the generalized CJ condition (11) is met, and is

$$D^2 = \sum_i Q_i \lambda_i. \tag{12}$$

This expression illustrates that the detonation velocity for the solution with sonic points is given by the net energy evolved from the lead shock to the sonic plane.

The second portion of the generalized CJ condition (11), the balance of reaction rates (zero thermicity condition), permits the reaction progress values along the limiting characteristic to be established. Since the first and second exothermic reactions are sequential, the balance of rates must occur between either the first and loss (third) reaction, or the second reaction and the loss, i.e. $r_1Q_1 + r_3Q_3 = 0$ or $r_2Q_2 + r_3Q_3 = 0$. Denoting these sonic points as A and B respectively, two solutions are obtained

$$\begin{aligned} \lambda_{1\mathrm{A}} &= 1 - \left(-\frac{k_3Q_3}{k_1Q_1}\right)^{\frac{1}{\nu_1}}, \ \lambda_{2\mathrm{A}} = 0, \text{ and} \\ \lambda_{3\mathrm{A}} &= \frac{k_3}{k_1(\nu_1 - 1)}\left(\left(-\frac{k_3Q_3}{k_1Q_1}\right)^{\frac{1-\nu_1}{\nu_1}} - 1\right) \end{aligned} \tag{13}$$

for the sonic point closest to the shock, and

$$\begin{aligned} \lambda_{1\mathrm{B}} &=1, \ \lambda_{2\mathrm{B}} = 1 - \left(-\frac{k_3Q_3}{k_2Q_2}\right)^{\frac{1}{\nu_2}}, \text{ and} \\ \lambda_{3\mathrm{B}} &= -\frac{k_3}{k_1(\nu_1 - 1)} + \frac{k_3}{k_2(\nu_2 - 1)}\left(\left(-\frac{k_3Q_3}{k_2Q_2}\right)^{\frac{1-\nu_2}{\nu_2}} - 1\right) \end{aligned} \tag{14}$$

for the second. The sonic point positions are found by substituting these results into the wave structure equations (8, 9, and 10),

$$\begin{aligned} \zeta_{\mathrm{A}} &= \zeta_1 - \frac{D}{k_1(\nu_1 - 1)}\left(\left(-\frac{k_3Q_3}{k_1Q_1}\right)^{\frac{1-\nu_1}{\nu_1}} - 1\right), \text{ and} \\ \zeta_{\mathrm{B}} &= \zeta_1 + \frac{D}{k_1(\nu_1 - 1)} - \frac{D}{k_2(\nu_2 - 1)}\left(\left(-\frac{k_3Q_3}{k_2Q_2}\right)^{\frac{1-\nu_2}{\nu_2}} - 1\right). \end{aligned}$$

The solution is now complete for the detonation speed and reaction zone structure in closed algebraic forms.

4. Steady analytical results

4.1. Integral curves

To illustrate the type of solution obtained, consider an example with parameters $D_{\mathrm{A}} < D_{\mathrm{B}}$, where D_{A} is the CJ detonation speed determined by sonic point A (equations 12 and 13), and D_{B} for sonic point B (equations 12 and 14). Figure 2a shows four families of integral curves for the parameters listed in table 1 with $D_{\mathrm{A}} < D_{\mathrm{B}}$ and one CJ point. For these parameters, $D_{\mathrm{A}} = 0.59397$ and $D_{\mathrm{B}} = 0.6$, while the equilibrium detonation speed is $D_{\mathrm{eq}} = \sqrt{Q_1 + Q_2 + Q_3} = 0.447$. The integral curves begin at the shock ($\zeta = 0$) with a value of ρ given by the inert shock jump conditions in Burgers equation, $\rho = 2D$, and proceed towards the burned side.

A steady shock velocity D is chosen, paying attention to its relation to D_{B} and D_{A}. When $D > D_{\mathrm{B}}$, the integral curve (top most curve in figure 2a) does not intersect any

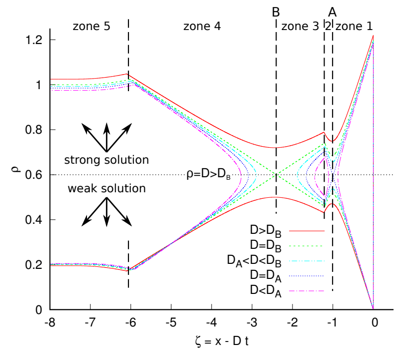

(a) One CJ point, $D_{\mathrm{A}} = 0.59397 < D_{\mathrm{B}} = 0.6$

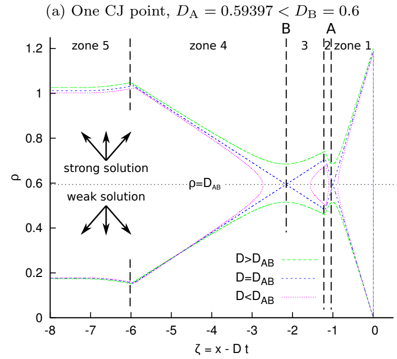

(b) Two CJ points, $D_{\mathrm{A}} = D_{\mathrm{B}} = D_{\mathrm{AB}} = 0.59397$

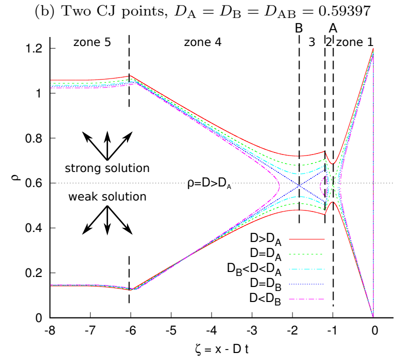

(c) One CJ point, $D_{\mathrm{A}} = 0.59397 > D_{\mathrm{B}} = 0.58784$

Figure 2. Family of steady integral curves for a detonation travelling from left to right with parameters found in table 1

sonic point $\rho = D$; this is the over-driven solution which requires that the rear boundary be maintained at the corresponding value. The evolution of ρ is non-monotonous. Initially (zone 1), the heat release is greater than the loss, i.e. $r_1Q_1 + r_3Q_3 > 0$, and the net positive thermicity leads to positive density and pressure gradients, owing to the amplification of forward-facing pressure waves. The first zero in density gradient corresponds to when $r_1Q_1 + r_3Q_3 = 0$ (point A), the first zero in thermicity. Towards the left (zone 2), $r_1Q_1 + r_3Q_3 < 0$, the density increases as pressure waves are attenuated. Once the second reaction begins and overcomes the endothermic processes (zone 3), $r_2Q_2 + r_3Q_3 > 0$, density once again decreases towards the left. After the second point of vanishing thermicity (point B), obtained when $r_2Q_2 + r_3Q_3 = 0$, the losses overcome the second exothermic reaction (zone 4). The last segment (zone 5) corresponds to when the losses terminate and the second reaction eventually comes to equilibrium.

For a detonation speed corresponding to the largest eigenvalue, $D = D_{\mathrm{B}}$ in this case, a sonic point appears at point B through the balance of the second reaction and the losses. Note that this sonic point is a saddle point (see section 7.2), and both weak and strong solutions can be attained on its left, depending on the rear boundary conditions. The strong solution is subsonic with respect to the detonation front and the weak solution is supersonic with respect to the detonation front. This means signals originating within the strong solution can catch up to the shock while signals from the weak solution cannot. This is the typical behaviour of pathological detonations, and well discussed by Fickett [31].

Sonic point B disappears at detonation speeds between the eigenvalues, $D_{\mathrm{A}} < D < D_{\mathrm{B}}$. The integral curves corresponding to this solution terminate at a singularity in zone 3.

When $D = D_{\mathrm{A}}$, a sonic point occurs at point A, where the first reaction balances the losses. However, a steady solution does not exist, owing to the singularity established in the reaction zone. It can thus be asserted that the smaller eigenvalue is not stable.

For detonation speeds lower than both eigenvalues, sonic point A disappears and the integral curves terminate at a singularity in zone 1. The equilibrium solution, where the detonation velocity is determined by the total heat release, is thus not possible.

The velocities D_{A} and D_{B}, calculated using equation 12 at the CJ points, are determined by the parameter set listed in table 1. Altering these parameters changes the values of λ_i at the CJ points, through equations 13 and 14, and therefore the detonation velocity associated with those CJ points. It is possible to reduce D_{B} by reducing the heat release of the second reaction, Q_2, for example.

Reducing Q_2 to the value in the second row of table 1 lowers the velocity associated with the second sonic point to be equal to the first sonic point velocity, $D_{\mathrm{A}} = D_{\mathrm{B}} = D_{\mathrm{AB}}$. The possibility of two sonic points appearing simultaneously in a steady solution arises. The steady shock speed determined by the generalized CJ criterion is equal for points A and B. This solution corresponds to integral curves passing through two saddle points, as shown in figure 2b. The weak and strong solutions are available to the left of both sonic points. Selection of the solution, strong or weak, between points A and B is independent of the rear boundary conditions because information from the rear boundary cannot cross sonic point B. When the detonation is over-driven, $D > D_{\mathrm{AB}}$, the integral curve does not intersect the sonic points and must be supported by the rear boundary condition. A steady solution does not exist when $D < D_{\mathrm{AB}}$ as singularities are established near points A and B.

Further reducing the second heat release (e.g., third row of table 1) lowers the second CJ point's detonation velocity below that of the first, $D_{\mathrm{B}} < D_{\mathrm{A}}$. In this case, the largest eigenvalue, D_A corresponds to the singularity free solution as shown in figure 2c. Over-driven $D > D_\mathrm{A}$ solutions exist, and singularities occur when $D < D_\mathrm{A}$. When $D = D_\mathrm{B} < D_\mathrm{A}$, a sonic point appears at B and a singularity is present at A.

4.2. Hugoniot and Rayleigh line analysis

The multiplicity of solutions can also be represented in ρ-p phase space analysed by traditional Hugoniot-type arguments [20, 31]. Constructing a solution requires connecting possible unburned and burned loci (Hugoniots) with possible integral curves (Rayleigh lines) intersecting the loci of zero-thermicity (e.g. points A and B shown in figure 2a). Such a representation offers further insight into the solution.

For the simple Fickett model [31] considered here, the Hugoniots are simply given by the equation of state 2. The unreacted shock Hugoniot ($\lambda_1 = \lambda_2 = \lambda_3 = 0$), the equilibrium Hugoniot ($\lambda_1 = \lambda_2 = \lambda_3 = 1$), the Hugoniot corresponding to the eigenvalue A ($\lambda_1 = \lambda_{1\mathrm{A}}$, $\lambda_2 = \lambda_{2\mathrm{A}}$, $\lambda_3 = \lambda_{3\mathrm{A}}$) and the Hugoniot corresponding to the eigenvalue B ($\lambda_1 = \lambda_{1\mathrm{B}}$, $\lambda_2 = \lambda_{2\mathrm{B}}$, $\lambda_3 = \lambda_{3\mathrm{B}}$), are shown in the ρ-p phase space of figure 3 for the single sonic point example studied in the previous section, where $D_\mathrm{A} < D_\mathrm{B}$ and whose integral curves are shown in figure 2a. Rewriting equation 6 as $\mathrm{d}(p - \rho D)/\mathrm{d}\zeta = 0$, with boundary conditions at the leading shock ($p = 2D^2$, $\rho = 2D$, and labelled as N in figure 3), they form the Rayleigh lines

$$p = \rho D. \tag{15}$$

which are shown in figure 3 for the eigenvalue B and the over-driven solution of figure 2a.

The over-driven integral curve ($D > D_\mathrm{B}$, subscript OD in figure 3) starts at the leading shock, point $\mathrm{N_{OD}}$, travels down the over-driven Rayleigh line, reaches point $\mathrm{A_{OD}}$ on the eigenvalue Hugoniot A, and then $\mathrm{B_{OD}}$ on the eigenvalue Hugoniot B, then returns to $\mathrm{S_{OD}}$ on the strong branch of the equilibrium Hugoniot. Points $\mathrm{A_{OD}}$ and $\mathrm{B_{OD}}$ are the local minima in the matching integral curve of figure 2, and correspond to the locus of zero thermicity, as explained above.

The integral curve of eigenvalue B ($D = D_\mathrm{B}$, subscript CJ,B) in figure 3 is tangent to Hugoniot B. It starts at point $\mathrm{N_{CJ,B}}$, travels down the Rayleigh B line, intersects the Hugoniot A at point $\mathrm{A_{CJ,B}}$ (first zero-thermicity point), then proceeds to the sonic point $\mathrm{B_{CJ,B}}$ on the eigenvalue Hugoniot B, shown in detail at the top-left of figure 3. Since this point is a saddle point, as shown in the integral curve, figure 2, the solution can then reach either the strong solution $\mathrm{S_{CJ,B}}$ or the weak solution $\mathrm{W_{CJ,B}}$.

The eigenvalue A integral curve (not shown in figure 3) is tangent to Hugoniot A and slightly lower than that of eigenvalue B for this case. Since Hugoniot A is lower than B, the corresponding velocity is also lower, seen by the Rayleigh line equation 15. Since this Rayleigh line never intersects Hugoniot B, a second zero thermicity point cannot be established in the system. The detonation speed selection rule and possible steady solution can thus also be made using the Hugoniot analysis. A regular solution requires intersection of the Rayleigh line with both zero-thermicity solutions. This can only be achieved for detonation velocities equal to, or larger than, the largest eigenvalue.

In the case where two simultaneous steady sonic points are possible, the Hugoniot curves A and B overlap.

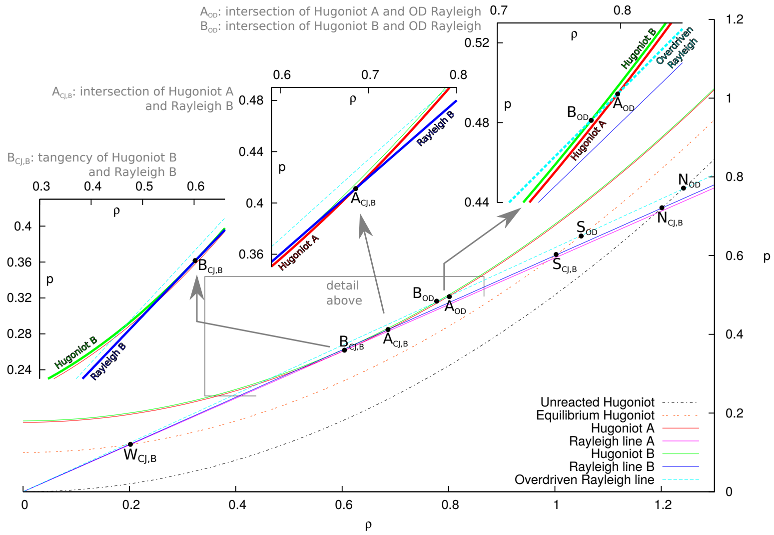

Figure 3. Rayleigh lines and Hugoniot curves on a ρ-p diagram with the leading shock (N), equilibrium (S and W), and the two zero-thermicity (A and B) loci for the single steady sonic point properties; two sets of points are shown: an over-driven detonation ($D > D_{\mathrm{B}} = 0.6 > D_{\mathrm{A}} = 0.59397$, shown with subscript OD), and a detonation travelling at the CJ velocity corresponding to a sonic point at point B only ($D = D_{\mathrm{B}} > D_{\mathrm{A}}$, shown with subscript CJ,B); N represents the unreacted shock condition, S and W correspond to the strong and weak equilibrium solutions respectively

5. Unsteady numerical method

Unsteady numerical simulations were used to study the stability and transients of the model. The domain was discretized with a uniform grid spacing of $\Delta x = 1/500$. A resolution study was performed, using the piston-initiated detonation described in section 6.1. The results in figure 4a show that the error, calculated by the L^2 relative error norm $\sqrt{\sum(\rho^2_{\mathrm{exact}} - \rho^2_{\mathrm{numeric}})/\sum \rho^2_{\mathrm{exact}}}$ once the solution reached steady state, converges with increased resolution at the expected rate, and the quasi-steady-state detonation velocity approaches the analytic result, shown by figure 4b.

Time step size was determined using the Courant-Friedrichs-Lewy (CFL) condition such that $\mathrm{CFL} = 0.5 = \Delta x/(\Delta t \times \max(\rho))$, where $\max(\rho)$ is the maximum value of ρ in the entire domain. A reaction threshold $\rho \geq 0.01$ was set to prevent unshocked gas from reacting. The effect of time step size, controlled by the CFL number, is shown in figure 4. While the steady state profile error increases slightly with decreasing time step, the detonation velocity approaches the CJ velocity and stabilizes at $\mathrm{CFL} = 0.5$ at a velocity slightly larger than CJ, seen in figure 4d.

The Riemann problem was solved at every cell interface using a first-order Godunov method as described by Clarke et al. [35]. Time evolution was done using a first-order upwind method.

A domain with an adaptive size was used where cells were dynamically added ahead

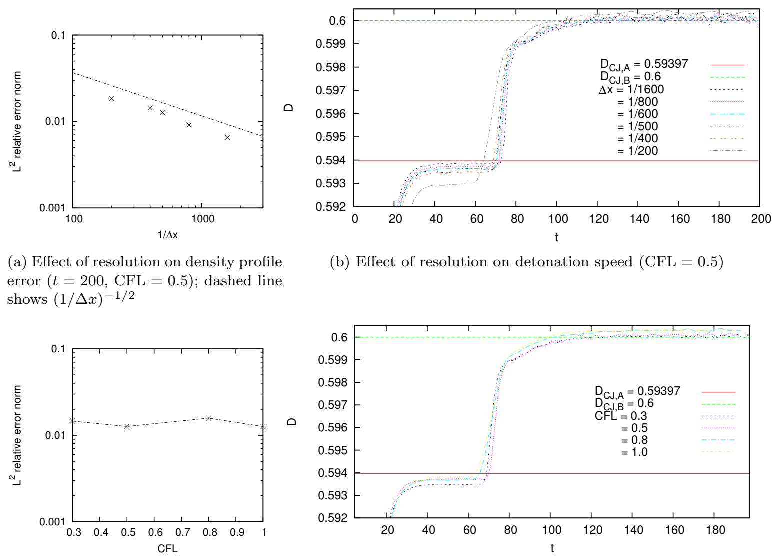

(a) Effect of resolution on density profile error ($t = 200$, CFL = 0.5); dashed line shows $(1/\Delta x)^{-1/2}$

(b) Effect of resolution on detonation speed (CFL = 0.5)

(c) Effect of time step on density profile error ($t = 200$, $\Delta x = 1/500$)

(d) Effect of time step on detonation speed ($\Delta x = 1/500$)

Figure 4. Effect of resolution and time step size on piston-initiated detonation described in section 6.1

of the shock, while cells in the rear were removed once the flow had equilibrated.

6. Unsteady numerical results

6.1. Piston-initiated detonation

An example of the unsteady evolution of piston-initiated detonations, for conditions where the second sonic surface is slightly faster than the first (i.e. $D_{\mathrm{B}} > D_{\mathrm{A}}$), is shown with snapshots of the ρ profile in figure 5 and with characteristics in figure 6.

A piston with velocity $\rho = 0.35$ was chosen in order to have an unsupported detonation, yet terminate at a value slightly larger than the weak solution. The initial condition can be seen in figure 5a.

The first reaction initially drives a shock (figure 5b). An over-expansion occurs once the first reaction weakens, followed by a recompression at the start of the second reaction, seen in figure 5c. The recompression forms into a shock (figure 5d) which weakens and falls behind as the front continues to accelerate (figure 5e), and a compression wave is formed at the piston as the loss reaction terminates just before the end of the second heat release. The piston is now behind the end of the reaction zone. The variable ρ increases at the beginning of the second reaction zone until it reaches the sonic condition, seen in figure 5f. The detonation front now travels at a speed D_{A} corresponding to the sonic surface A.

Recall that the $D = D_{\mathrm{A}}$ steady solution from section 4 terminates in a singularity

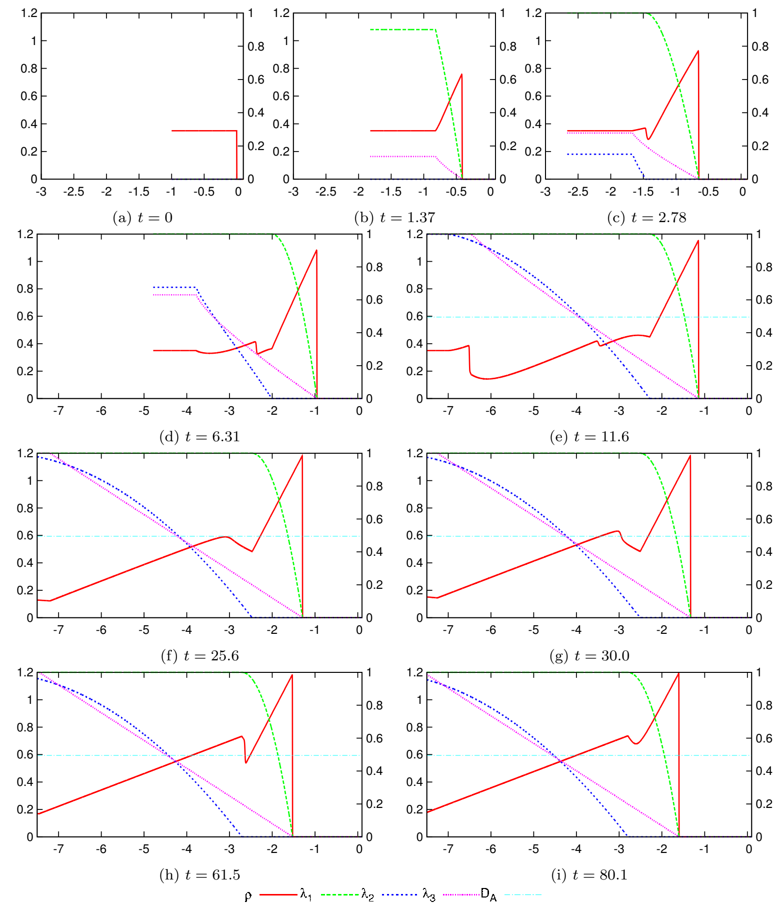

(a) $t = 0$ (b) $t = 1.37$ (c) $t = 2.78$

(d) $t = 6.31$ (e) $t = 11.6$

(f) $t = 25.6$ (g) $t = 30.0$

(h) $t = 61.5$ (i) $t = 80.1$

(j) Legend: left axis for ρ, right axis for λ_i, horizontal axis for $\zeta = x - D_{\mathrm{B}}t$

Figure 5. Wave profiles for piston-initiated detonation for the single sonic point case where $D_{\mathrm{CJ}} = D_{\mathrm{B}} = 0.6 > D_{\mathrm{A}} = 0.59397$

behind sonic point A. In the context of this unsteady solution, a shock that travels faster than sonic surface A is created at sonic surface B (figure 5g), eventually penetrating into the first reaction zone. It can thus be asserted that the smaller eigenvalue D_{A} is not stable, but can be established as an intermediate transient. The shock wave that is formed behind the singularity eventually catches up to the lead shock. A truly steady detonation is eventually established, travelling with a speed corresponding to the largest predicted eigenvalue D_{B}, and with a new corresponding sonic surface B (figure 5i).

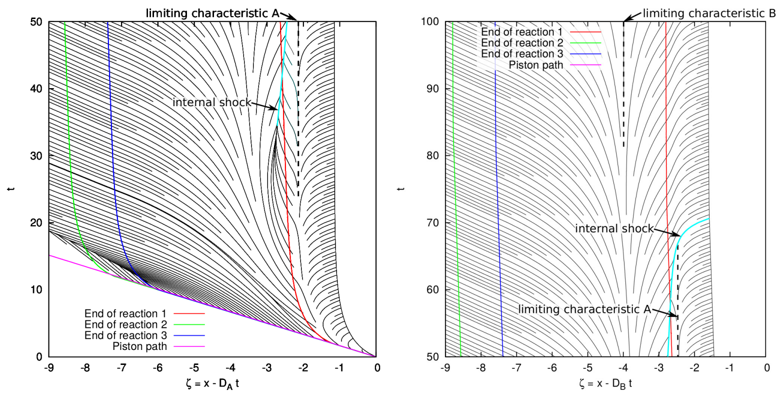

(a) At early times

(b) At later times

Figure 6. Characteristic diagram for a piston-initiated detonation (single sonic point case, $D_{\mathrm{A}} = 0.59397$, $D_{\mathrm{B}} = 0.6$)

The process can also be visualized with the characteristic diagrams of figure 6. Characteristics outside the detonation's domain of influence (i.e. to the right of the front) are omitted. Recall that the model only admits the forward-facing family of characteristics (in the absolute frame of reference). This family of characteristics is shown in the frame of reference travelling at the velocity D_{A} in figure 6a and D_{B} in figure 6b.

Figure 6a shows that the detonation front (the right-most characteristic) quickly becomes vertical as it stabilizes to a speed D_{A}. The limiting characteristic A forms at sonic point A, whose neighbouring characteristics diverge on either side. Characteristics to the left of the sonic point turn back towards sonic point A and create an internal shock where characteristics of the same family intersect, resulting in a two-valued discontinuity. Sonic point B appears at the same time with diverging characteristics on either side.

In the right frame of figure 6, the internal shock is seen travelling towards the front, eventually overtaking the limiting characteristic A and reaching the detonation front. The front then accelerates to the velocity D_{B}. A limiting characteristic is then established at point B, parallel to the detonation front in the $\zeta - t$ plane.

The piston-initiated detonation travelled at the velocity D_{A} once the generalized CJ criterion was satisfied at sonic point A. Figure 4 shows the detonation front velocity travelled steadily until the arrival of the internal shock at the front, after which it travelled steadily at the velocity D_{B}. The creation of the internal shock appears to coincide with appearance of sonic point B, but the reason for its formation may lie hidden behind the complex transient evolution of the problem.

6.2. Two simultaneous CJ points

A small modification was made in the second heat release as discussed in section 4, listed in the second row of table 1. This allowed for two steady sonic points to exist simultaneously, both with the steady detonation velocity of point A. The possible integral curves for this example connecting the quiescent gas to rear conditions are shown in figure 2b when $D = D_{\mathrm{AB}}$.

The piston-initiated detonation of the double sonic point solution, with the same piston velocity as the previous case, evolved qualitatively similar to the single sonic point case discussed in the previous section. Upon establishing the two sonic points A and B predicted by the analytical solution, a shock was produced at point B as before. The shock reached the front and a steady state emerged with only a single sonic point, as opposed to the two predicted by the integral curves. This discrepancy is reviewed in section 7.

The piston-initiated detonation reached the predicted steady state before creating a shock, meaning that analytical steady-state solutions with two simultaneous sonic points can be used as initial conditions to study the origin of the internal shock.

The steady state starts ($\zeta = 0$) in the strong regime since the detonation is lead by a shock. Two options are available to the flow at each sonic point, following either the strong or weak solution, making for four possible steady states when two CJ points are present. This number is increased by the possibility of shocks joining the weak and strong solutions. The shock speed S in the Burgers equation, simply given by the average of left and right states [20]

$$S = \frac{1}{2}(\rho_{\mathrm{left}} + \rho_{\mathrm{right}}), \tag{16}$$

allows shocks that travel at exactly the leading shock speed. Internal shocks can only exist to the left of the sonic points where there can be a jump from the weak to the strong solution.

The shock-free initial steady-state curves will be referred to with an abbreviated notation. This notation will break the flow profile into three sections: the rear solution, the solution between the sonic points, and the solution behind the leading shock. A strong solution will be abbreviated with the letter S and a weak solution with the letter W. For example, WWS would refer to a detonation whose rear boundary follows the weak solution, has the weak solution between sonic points, and necessarily has the strong solution behind the leading shock. The WWS initial condition can be seen in figure 7a.

Simulations initiated with internal shock waves, such as the one produced at point B, behaved in the same manner as those which evolved shocks on their own and are therefore excluded from further presentation.

6.2.1. WWS initial condition

The first simulation was initiated with the WWS integral curve described in the previous paragraph and seen in figure 7a. The exact WWS solution was imposed on the domain at $t = 0$ then evolved through time. This solution can be achieved naturally with an under-driven piston, as demonstrated by the single CJ point, piston-initiated detonation seen in figure 5f, and behaves much in the same way. Following initiation, a disturbance travels rearwards (figure 7b) from the valley at the boundary between zones 2 and 3. A shock forms at point B following the arrival of the disturbance (figure 7c). The shock travels faster than sonic point A, and eventually catches up to it and the front. During this transit, the detonation is slightly under-driven, while the final result is slightly over-driven and has a single sonic point at B (figure 7d), appearing

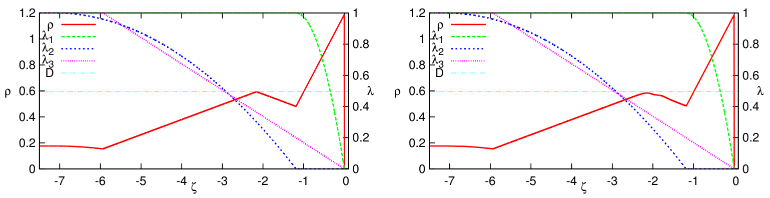

(a) Initial condition ($t = 0$)

(b) A disturbance approaches point B ($t = 12$)

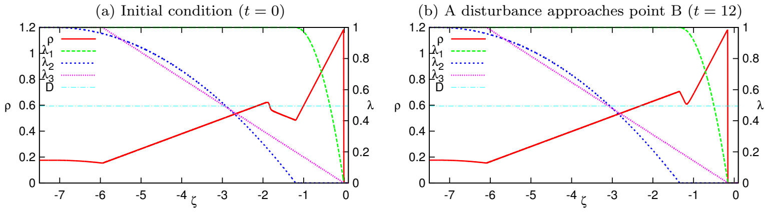

(c) A shock forms and travels forward once the disturbance reaches point B ($t = 44$)

(d) Detonation is slightly over-driven following the internal shock's arrival at the front ($t = 450$)

Figure 7. Wave profiles for WWS steady-state-initiated detonation for the double sonic point case ($D_{\mathrm{CJ}} = D_{\mathrm{AB}} = 0.59397$)

qualitatively similar to case $D = D_{\mathrm{B}}$ in figure 2a.

The unsteady simulation can also be visualized using the characteristic diagram in figure 8. Two quasi-steady runs of diverging characteristics are initially seen at points A and B. The internal shock forms early on ($t < 50$) and reaches the detonation front between $t = 400$ and $t = 450$. The detonation front is initially slightly under-driven and slopes slightly towards the left, but then slopes to the right as it becomes over-driven when the internal shock reaches the front.

6.2.2. SWS initial condition

Next consider a simulation initiated with the SWS integral curve shown in figure 9a. A disturbance (figure 9b) creates an internal shock (figure 9c) which catches up to the detonation front (figure 9d) in the same manner as described in the WWS case. Another shock is then created downstream of sonic point B, joining newly supersonic flow (with respect to the detonation front) behind point B to subsonic flow of the rear boundary condition. This new shock wave distances itself from the front (figure 9e).

The characteristics are shown in figure 9f. Formation of the first internal shock occurs like in the WWS case. The second shock then forms behind sonic point B, where characteristics now diverge, and slowly travels away from the front. The rear of the domain is largely uniform with characteristics travelling towards the shock.

6.2.3. SSS and WSS initial conditions

The third and fourth possibilities, the SSS and WSS initial conditions, are not shown due to their simplicity. The SSS initial condition is nearly achieved in figure 9d and evolves the same way to a slightly over-driven detonation with a shock behind the second sonic point, like figure 9e.

For the WSS initial condition, point A drifts up into the strong solution, and the

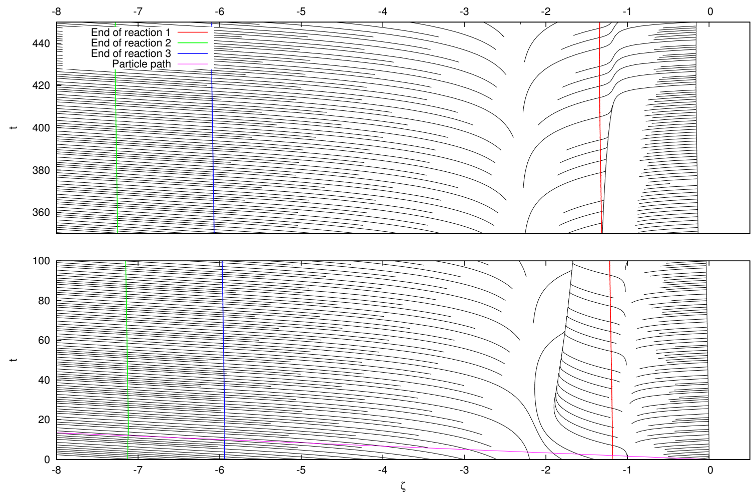

Figure 8. Characteristic diagram for the double sonic point detonation initiated with the WWS steady-state solution shown in figure 7; intermediate time omitted in favour of clarity ($D_{\mathrm{CJ}} = D_{\mathrm{AB}} = 0.59397$)

solution travels in a manner similar to the final state of figure 7d, again slightly over-driven.

6.3. Inclusion of viscosity

In the case of two simultaneous steady CJ points, the velocity of both sonic points should be equal $D_{\mathrm{A}} = D_{\mathrm{B}} = D_{\mathrm{AB}}$ and the integral curves predict steady sonic points at A and B. Peculiarly, simulations of all initial conditions lead to an over-driven point A in the strong solution, instead of being sonic.

A hint to the reason can be found in the resolution study shown in figure 4b. Low resolution simulations tend to travel slower than predicted by the generalized CJ criterion when sonic point A controls the detonation speed, and faster than predicted when the detonation speed is controlled by sonic point B. This discrepancy is reduced by increasing resolution but not eliminated.

While the inviscid analysis predicts that the sonic point speeds should be equal, $D_{\mathrm{A}} = D_{\mathrm{B}} = D_{\mathrm{AB}}$, numerical diffusion effectively causes the first sonic surface to travel slower than the second, $D_{\mathrm{A}} < D_{\mathrm{B}}$. When two sonic points are present, a perturbation from point B forces point A to become subsonic and the detonation adopts the faster velocity, as seen in the case with single steady CJ point, figure 5f onwards.

A 'physical' viscosity was added to Fickett's detonation analogue hydrodynamic equation 1 as

$$\partial_t \rho + \partial_x p = \mu \partial_{xx} \rho \tag{17}$$

to assess whether this is a numerical artifact or if physical diffusion will have the

17

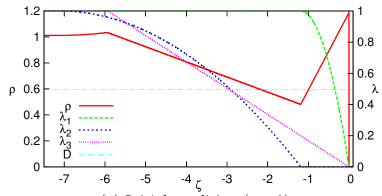

(a) Initial condition ($t = 0$)

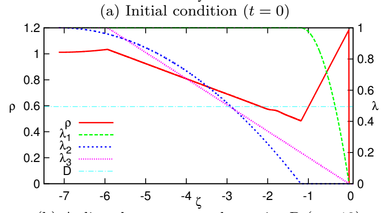

(b) A disturbance approaches point B ($t = 12$)

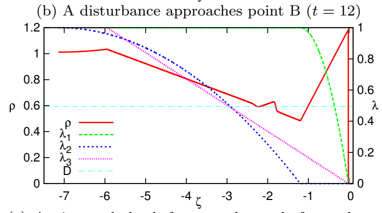

(c) An internal shock forms and travels forward once the disturbance reaches point B ($t = 52$)

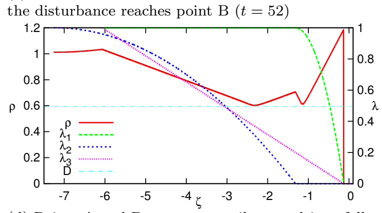

(d) Points A and B are temporarily over-driven following the internal shock's arrival at the front ($t = 351$)

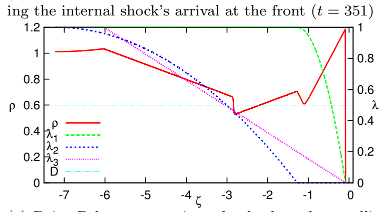

(e) Point B becomes sonic and a backwards-travelling internal shock is formed ($t = 600$)

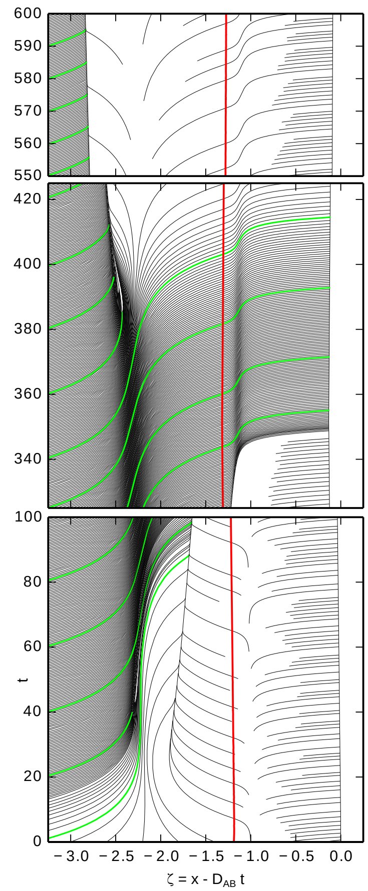

(f) Characteristic diagram; intermediate times omitted, characteristics are periodically highlighted green, and the vertical red line indicates end of first reaction

Figure 9. Wave profiles and characteristic diagram for SWS steady-state-initiated detonation with the double sonic point case ($D_{\mathrm{CJ}} = D_{\mathrm{AB}} = 0.59397$)

same effect. The constant viscosity coefficient $\mu = 0.01$ was chosen to be an order of magnitude smaller than the heat release coefficients. The second-order derivative was discretized using centred differences, and the maximum time step size was selected by

$$\Delta t = \min\left(\mathrm{CFL} \times \frac{\Delta x}{\rho_{\max}}, \mathrm{CFL} \times \frac{1}{2}\frac{\Delta x^2}{\mu}\right)$$

for numerical stability. The reaction threshold was raised to $\rho \geq 0.05$ to prevent reactions from starting in the diffusive foot of the incident shock. The viscous simulations with two simultaneous CJ points (section 6.2) were initiated with the ideal inviscid steady state profiles.

In the WWS case, the sharp corners of the initial profile are quickly rounded (figure 10a) and the shock slows, as seen by the negative slope of the shock path in figure 10d. Signals near point B now travel faster than the decayed shock and begin to move towards the front. The valley between the points A and B transitions (figure 10b) from the weak solution to the strong solution and point A becomes non-sonic. The shock accelerates to a steady speed $D < D_{\mathrm{AB}}$, seen by the change in slope of the shock path in figure 10d, driven by the net heat release between the shock and sonic point B. The WWS initial condition has transitioned to a WSS detonation with a non-sonic point A (figure 10c), like the inviscid case in figure 7d but travelling slower due to the additional viscous losses.

Detonations initiated with the SWS or SSS cases end up qualitatively resembling the $D > D_{\mathrm{AB}}$ case of figure 2b, without sonic points in the solution as both points A and B become overdriven. A steady, overdriven viscous SSS solution is established, supported by the rear boundary condition at the inviscid CJ speed.

The addition of physical viscosity exaggerates the overdrive of point A seen in the inviscid two CJ point cases. Viscosity slows the detonation below its inviscid CJ speed, because of the additional viscous losses. The state-dependent diffusive losses are more important between the front and point A than point B, under these parameters, causing point A to become overdriven when two CJ points would coexist without viscosity.

This suggests the discrepancy seen in the inviscid simulations is caused by numerical diffusive losses, since a similar structure is observed in viscous calculations. Numerical error causes the detonation to travel slightly faster than CJ and this difference is communicated to the front through the creation of an internal shock at point B.

7. Creation of internal shocks

The piston initiation of a detonation with a single steady CJ point yielded the steady integral curves. As the detonation front accelerated from the piston face, it began with a velocity $D < D_{\mathrm{A}} < D_{\mathrm{B}}$. The detonation velocity temporarily stabilized when $D = D_{\mathrm{A}}$ because the creation of sonic point A stopped signals from the rear boundary from affecting the front. A shock formed behind point A, as inferred by the singularity in the integral curve (figure 2a), and sonic point B appeared behind the shock. Both sonic points A and B coexisted until the internal shock reached the detonation front, accelerating it to $D = D_{\mathrm{B}}$. The detonation then continued steadily with the single sonic point predicted in the integral curves of figure 2a.

This supports the results of unsteady simulations by Khasainov and Veyssière [13] that found the regime with a slower detonation speed was always accelerated to the

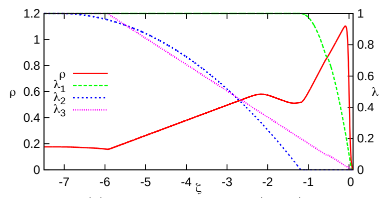

(a) Rounding of corners ($t = 1$)

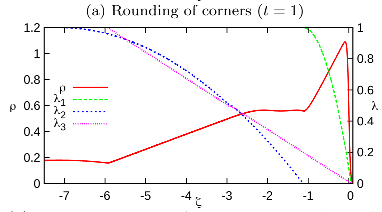

(b) Flow between points A and B transitions from the weak to the strong solution ($t = 4$)

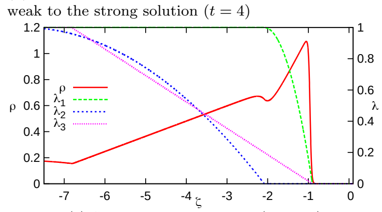

(c) Steady viscous solution ($t = 400$)

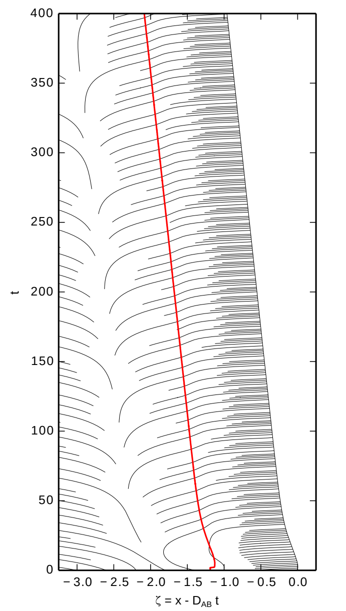

(d) Characteristic diagram; the vertical red line indicates end of first reaction

Figure 10. Wave profiles and characteristic diagram for the viscous WWS initiated with the inviscid steady-state detonation profile (figure 7a) with the double sonic point case ($\mu = 0.01$, $D_{\mathrm{AB}} = 0.59397$)

faster velocity regime when multiple solutions were possible.

The same sequence of events was seen under parameters that should have yielded two steady CJ points. The detonation evolved to have a single CJ point instead of the two predicted in figure 2b. The piston initiation transient was removed by initiating simulations with the predicted steady integral curves to investigate the discrepancy. However, none of the steady profiles prove to be stable, ending up with a CJ point B and subsonic point A (with respect to the detonation front, i.e. in the strong solution). The detonation front propagated slower than expected while under the influence of point A, shown to be a result of numerical diffusion.

Interestingly, the internal shocks, when created, always formed at sonic point B. This indicates sonic points A and B may be unstable when they coexist. The creation of internal shocks at sonic points will be investigated using the method of characteristics in section 7.1 and using linear stability analysis in section 7.2.

7.1. Inspection of sonic points by the method of characteristics

In the following analysis, sonic points will be labelled in the same manner as the steady-state solutions: sonic points lying between two weak solutions (e.g. point B seen in the WWS structure of figure 5f) will be called a sonic point of type WW.

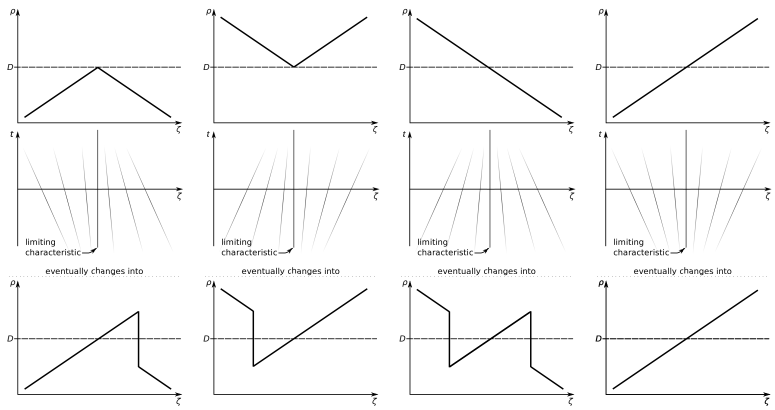

(a) WW sonic point results in an upstream shock

(b) SS sonic point results in a downstream shock

(c) SW sonic point results in shocks on either side

(d) WS sonic point remains stable

Figure 11. Illustration of shock creation in vicinity of a sonic point: initial signal speed ρ (top), initial instantaneous characteristics (middle), and resulting signal speed ρ (bottom)

Likewise, a sonic point between two strong solutions ($\rho > D$) will be named SS, WS will be used for sonic points with a strong upstream solution and weak downstream solution ($\rho < D$), and SW will be used when there is a weak upstream and strong downstream solution. The top frames of figure 11 serve as illustrations.

Internal shocks were created in all simulations, with the exception of the WSS structure and the over-driven viscous SSS structure. Point B was always the source for these shocks except when of type WS. SS-type sonic points quickly became subsonic with respect to the detonation front, but WS sonic points remained stable until shocked. It appears WS sonic points are stable, unless shocked, while the others are unstable.

The method of characteristics was used near the two sonic points to assess their stability. Figure 11 shows the flow in vicinity of the four types of sonic points. The top frames show ρ, which can be interpreted as the signal speed in Fickett's analogy, for the four types of sonic point. The bottom frames show the resulting profiles of ρ expected from the simulations and following analysis. The middle frames show the instantaneous characteristics (information paths) corresponding to the top frames. Perturbations travel along these characteristic lines which each have a slope $\mathrm{d}t/\mathrm{d}\zeta \propto 1/(\rho - D)$. The limiting characteristic travels at the same speed as the detonation front along the sonic point. For the strong solution, perturbations from the rear (left) are able to reach the limiting characteristic (and detonation front) as they travel faster than the front. For the weak solution, perturbations cannot keep up with the front and are therefore carried towards the left, away from the limiting characteristic.

For a sonic point of type WW (figure 11a) the characteristic diagram shows that any perturbation downstream (left) of the sonic point will easily be dissipated to the rear as the information speeds away from the front in that direction. Upstream perturbations (to the right), will accumulate and eventually disturb the sonic point. If the perturbations cross the sonic line, a shock wave must be formed to link the weak upstream solution to the new strong solution immediately to the right of the sonic point. Flow immediately to the right of the sonic point now satisfies the strong solution while there is no change to the downstream weak solution. The WW sonic point transitions to a WS sonic point, seen in the bottom frame of figure 11a, with an upstream shock that connects the strong solution to the weak solution. This behaviour is mirrored for SS sonic points, in opposite directions.

The sharp profile at the WW point may become temporarily curved and supersonic, seen at point B in figure 5f, allowing perturbations from the upstream side to slip downstream. This is mirrored in SS points which become temporarily subsonic, seen at point A of figures 7d and 9e. These curved super/subsonic profiles are not solutions of the inviscid steady equations with two CJ points, but are caused by numerical (or physical) diffusion. The solutions with internal shocks shown in the bottom frames of figure 11 are valid forms of the inviscid steady equations.

Sonic points of type SW, shown in figure 11c, are also unstable. Perturbations accumulate on either side, like they do on the right and left sides of WW and SS sonic points. Shocks are eventually created on either side of the sonic point which finally takes the WS form, as seen in figure 9.

Finally, the characteristics around a type WS sonic point (figure 11d) show that perturbations should easily be dissipated away on either side. This explains the stability of this type of sonic point seen in the simulations.

This analysis suggests that only WS sonic points are stable due to their diverging characteristic paths. The other types of steady sonic point should transform to create shocks and stable WS sonic points. This leads to a further consequence: in order for a solution with two coexisting sonic points to remain steady and stable, the sonic points must be separated by a shock wave. The location of this shock between the two sonic points is arbitrary in the framework of this model. Although this internal shock is protected from disturbances behind the second sonic point, it is affected by disturbances originating between the sonic points. In simulations, internal shocks between the sonic points always reached the detonation front. This instability is ascribed to the effect of numerical diffusion and a feature of the model, whereby the internal shock may exist anywhere between two sonic points. It is not clear how this translates to more complex models (such as the Euler equations) and more realistic descriptions of kinetic rates, where shocks may be anchored by the state dependence of reactions. Steady internal shocks between CJ points have been seen by Veyssière and Khasainov [11, 12]. While investigating these double-front detonations, they found [13] that "the distance between the two subsonic zones evolves very slowly" at the end of their unsteady simulations. The internal shock in the Euler equations may also be unstable, but further study is required.

7.2. Linear stability analysis of sonic points

The stability of the sonic points can also be studied using linear stability analysis. A new independent variable s is defined such that $\mathrm{d}\zeta/\mathrm{d}s = \rho - D$ in order to remove the singularity from equation 6, yielding a system of equations

$$\frac{\mathrm{d}\zeta}{\mathrm{d}s} = \rho - D, \qquad \frac{\mathrm{d}\rho}{\mathrm{d}s} = \frac{\sigma}{D}, \qquad \text{and} \qquad \frac{\mathrm{d}\lambda_i}{\mathrm{d}s} = -\frac{r_i}{D}(\rho - D). \tag{18}$$

Setting these equations to zero reveals fixed points where the generalized CJ criterion of equation 11 is met at sonic points A and B, i.e. $\rho = D$ and $\sigma = 0$. Linearising the

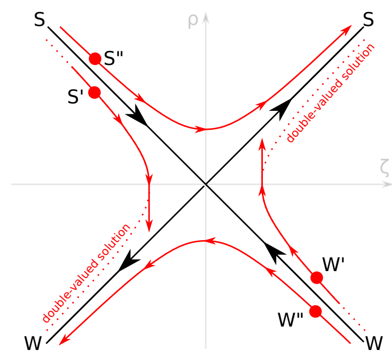

Figure 12. Illustration of the linear stability analysis around the sonic points in the ζ-ρ plane, revealing the existence of a saddle node; typical points S and W (strong and weak) lying on the detonation profile are shown with their trajectories in red; single prime labels points between the eigenvectors, double prime for points above and below

singularity-free system (equation 18) around sonic point A, whose reaction progress variables are in equation 13, gives the Jacobian of $[\zeta, \rho, \lambda_1, \lambda_2, \lambda_3]$

$$J_{\mathrm{A}} = \begin{bmatrix} 0 & 1 & 0 & 0 & 0 \\ 0 & 0 & -\frac{k_1Q_1\nu_1}{2D}\left(-\frac{k_3Q_3}{k_1Q_1}\right)^{\frac{\nu_1-1}{\nu_1}} & 0 & 0 \\ 0 & -\frac{k_1}{D}\left(-\frac{k_3Q_3}{k_1Q_1}\right) & 0 & 0 & 0 \\ 0 & 0 & 0 & 0 & 0 \\ 0 & -\frac{k_3}{D} & 0 & 0 & 0 \end{bmatrix}$$

with eigenvalues $e_{\mathrm{A}} = \pm\sqrt{\frac{k_1^2Q_1\nu_1}{2D^2}\left(-\frac{k_3Q_3}{k_1Q_1}\right)^{\frac{2\nu_1-1}{\nu_1}}}$ and $e_{\mathrm{A}} = 0$. All parameters being positive, with the exception of Q_3, the two non-zero eigenvalues are real and of opposite signs. A saddle node [36] therefore exists at point A with eigenvectors

$$E_{\mathrm{A}} = \left[\frac{1}{e_{\mathrm{A}}}, 1, -\frac{k_1}{D}\left(\frac{-k_3Q_3}{k_1Q_1}\right)\frac{1}{e_{\mathrm{A}}}, 0, \frac{-k_3}{D}\frac{1}{e_{\mathrm{A}}}\right]^T.$$

This analysis at point B yields the same eigenvalues, with parameters of the first reaction replaced by those of the second, and same for the eigenvectors.

The saddle node is illustrated in figure 12 in ρ-ζ space. The unstable eigenvector with a positive slope and the stable eigenvector with a negative slope are drawn in black. The typical trajectories of signals are plotted in red.

Consider a sonic point of type SS which is perturbed on the left side to have a value of ρ slightly above its ideal value, it can be written as S$''$S in accordance with the figure. The signal from the point S$''$ will first travel towards the saddle node then be repulsed and move away from the node in the S direction on the right side. This gives rise to a curved subsonic point like seen at A in figures 5i, 9e, and 7d whose perturbation may be caused by rounding through diffusion. The same process works in the reverse direction for a type WW$''$ point.

A signal S$'$ of the strong branch starting below the eigenvector on the left side will travel towards the node, but following its trajectory will eventually force a double-valued ρ which is inadmissible along the ζ axis so a shock will form. The story is the same for a signal originating from the W$'$ position.

The linear stability analysis mirrors the conclusions made using the method of characteristics. Disturbances from the bottom left or top right are repulsed from the node and do not cause shocks, so WS sonic points remain stable. Sonic points of type S$''$S and WW$''$ will become non-sonic, and points with S$'$ or W$'$ will create shocks.

8. Conclusion

Detonations with two sequential heat releases and a concurrent loss were studied using Fickett's detonation analogue. The study aimed to clarify the steady reaction zone structure and velocity when the two sonic planes propagated with different speeds (the general case). It was found that a steady detonation must travel at the maximum velocity dictated by the net heat release between the front and each zero-thermicity point. Singularities were found in the flow structure at lesser velocities, and the lack of sonic point at larger velocities opened the detonation front to perturbations. This supports other studies [11–14] which found transitions from the lower detonation velocities to higher ones, but not vice-versa.

Piston-initiated unsteady numerical simulations showed that the lower detonation velocities were quasi-steady. The formation of a forward-travelling shock and its subsequent arrival at the front caused the detonation to accelerate to its higher velocity. This phenomenon is believed to be the cause of the detonation front's sudden acceleration previously mentioned by Bdzil et al. [14].

The second goal of this study was to determine the stability of the internal shock sometimes present in double-structured detonations. This was done by studying cases where both sonic planes coexisted. The presence of one sonic point in the flow allows the existence of an internal shock behind. Internal shocks were found to be unstable due to diffusive effects and to the independence of reaction rates from the flow field, which allows internal shocks to exist anywhere. It is not clear if or how reaction dependence on hydrodynamics could anchor internal shocks, further work is needed to establish in what capacity internal shocks can be stable, as suggested by Veyssière and Khasainov [11, 12].

Finally, the origin of the internal shock was sought. Perturbations were found to accumulate at any sonic point with characteristics that do not diverge on both sides, leading to the creation of internal shocks in many cases. This is supported by a linear stability analysis which clarifies why perturbations form shocks or rounded points. As a consequence, two sonic points may only co-exist in a stable fashion (WS) if they are separated by a shock. This clarifies the roots of double front detonations seen in previous work [4, 5, 8, 12, 15], and is also the mechanism by which detonations transition from slower quasi-steady velocities to faster ones.

Acknowledgements

The authors would like to acknowledge funding from the Defence Research and Development Canada (DRDC), the Ontario Graduate Scholarship (OGS) fund, as well as the Natural Science and Engineering Research Council (NSERC) of Canada in the form of a Canadian Graduate Scholarship (CGS).

References

[1] H. Presles, D. Desbordes, M. Guirard, and C. Guerraud, *Gaseous nitromethane and nitromethane-oxygen mixtures: a new detonation structure*, Shock Waves 6 (1996), pp. 111–114.

[2] F. Joubert, D. Desbordes, and H.N. Presles, *Detonation cellular structure in* no_2/n_2o_4*-fuel gaseous mixtures*, Combustion and Flame 152 (2008), pp. 482–495.

[3] V. Gamezo, J. Wheeler, A. Khokhlov, and E. Oran, *Multilevel structure of cellular detonations in type ia supernovae*, The Astrophysical Journal 512 (1999), p. 827.

[4] F. Zhang, *Detonation in reactive solid particle-gas flow*, Journal of propulsion and power 22 (2006), pp. 1289–1309.

[5] E. Afanasieva, V. Levin, and Y.V. Tunik, *Multifront combustion of two-phase medium*, Shock Waves, Explosions, and Detonations: AIAA Progress in Astronautics and Aeronautics (1983), pp. 394–413.

[6] B. Khasainov and B. Veyssiere, *Steady, plane, double-front detonations in gaseous detonable mixtures containing a suspension of aluminum particles*, Dynamics of explosions (1988), pp. 284–299.

[7] W. Fickett and W. Davis, *Detonation: Theory and experiment* (1979).

[8] F. Zhang, *Detonation of gas-particle flow*, in *Shock Wave Science and Technology Reference Library, Vol. 4*, Springer, 2009, pp. 87–168.

[9] I.B. Zeldovich and A.S. Kompaneets, *Theory of detonation*, Academic Press, 1960.

[10] J.H. Lee, *The detonation phenomenon*, Vol. 2, Cambridge University Press Cambridge, 2008.

[11] B. Veyssiere and B. Khasainov, *A model for steady, plane, double-front detonations (dfd) in gaseous explosive mixtures with aluminum particles in suspension*, Combustion and Flame 85 (1991), pp. 241–253.

[12] B. Veyssiere and B. Khasainov, *Structure and multiplicity of detonation regimes in heterogeneous hybrid mixtures*, Shock Waves 4 (1995), pp. 171–186.

[13] B. Khasainov and B. Veyssiere, *Initiation of detonation regimes in hybrid two-phase mixtures*, Shock Waves 6 (1996), pp. 9–15.

[14] J. Bdzil, M. Short, G. Sharpe, T. Aslam, and J. Quirk, *Higher-order DSD for detonation propagation: DSD for detonation driven by multi-step chemistry models with disparate rates*, in *Proceedings of the 13th International Detonation Symposium, Norfolk, Virginia.* 2006, pp. 726–736.

[15] B. Veyssiere, *Double-front detonations in gas-solid particles mixtures*, Dynamics of Shock Waves, Explosions, and Detonations, Progress in Astronautics and Aeronautics 94 (1984), pp. 264–276.

[16] I. Brailovsky and G.I. Sivashinsky, *Hydraulic resistance as a mechanism for deflagration-to-detonation transition*, Combustion and flame 122 (2000), pp. 492–499.

[17] I. Brailovsky and G. Sivashinsky, *Effects of momentum and heat losses on the multiplicity of detonation regimes*, Combustion and flame 128 (2002), pp. 191–196.

[18] J.P. Dionne, H.D. Ng, and J.H. Lee, *Transient development of friction-induced low-velocity detonations*, Proceedings of the Combustion Institute 28 (2000), pp. 645–651.

[19] R. Semenko, L. Faria, A.R. Kasimov, and B. Ermolaev, *Set-valued solutions for non-ideal detonation*, Shock Waves 26 (2016), pp. 141–160.

[20] W. Fickett, *Detonation in miniature*, Am. J. Phys 47 (1979), pp. 1050–1059.

[21] A. Majda, *A qualitative model for dynamic combustion*, SIAM Journal on Applied Mathematics 41 (1981), pp. 70–93.

[22] L.M. Faria, A.R. Kasimov, and R.R. Rosales, *Theory of weakly nonlinear self-sustained detonations*, Journal of Fluid Mechanics 784 (2015), pp. 163–198.

[23] J.B. Bdzil and R. Klein, *Weakly nonlinear dynamics of near-CJ detonation waves*, in *Combustion in High-Speed Flows*, ICASE/LaRC Interdisciplinary Series in Science and Engineering Vol. 1, Springer, 1994, pp. 513–540.

[24] F.E. Marble, *Dynamics of dusty gases*, Annual Review of Fluid Mechanics 2 (1970), pp. 397–446.

[25] P. Clavin and F.A. Williams, *Dynamics of planar gaseous detonations near Chapman-Jouguet conditions for small heat release*, Combustion Theory and Modelling 6 (2002), pp. 127–139.

[26] M.I. Radulescu and J. Tang, *Nonlinear dynamics of self-sustained supersonic reaction waves: Ficketts detonation analogue*, Physical review letters 107 (2011), p. 164503.

[27] A.R. Kasimov, L.M. Faria, and R.R. Rosales, *Model for shock wave chaos*, Physical review letters 110 (2013), p. 104104.

[28] D.I. Kabanov and A.R. Kasimov, *Linear stability analysis of detonations via numerical computation and dynamic mode decomposition*, Physics of Fluids 30 (2018), p. 036103.

[29] X. Mi and A.J. Higgins, *Influence of discrete sources on detonation propagation in a Burgers equation analog system*, Physical Review E 91 (2015), p. 053014.

[30] J. Tang, *Study of the instability and dynamics of detonation waves using fickett's analogue to the reactive euler equations*, Master's thesis, University of Ottawa, 75 Laurier Avenue East, Ottawa, ON, K1N 6N5, Canada, 2013.

[31] W. Fickett, *Introduction to detonation theory*, Vol. 5, Univ of California Press, 1985.

[32] L.M. Faria and A.R. Kasimov, *Qualitative modeling of the dynamics of detonations with losses*, Proceedings of the Combustion Institute 35 (2015).

[33] M.I. Radulescu, J. Tang, and F. Zhang, *Multiplicity of detonation regimes in systems with a multi-peaked thermicity. Part 1: Ficketts detonation analogue*, in *Proceedings of the 24th ICDERS*, Taipei, Taiwan. 2013.

[34] S. Lau-Chadeplaine, J. Tang, F. Zhang, and M. Radulescu, *On the existence and stability of double-front detonations*, in *Proceedings of the 15th International Detonation Symposium*, Jul., San-Francisco, California, USA. 2014.

[35] J. Clarke, P. Roe, L. Simmonds, and E. Toro, *Numerical studies of a detonation analogue*, Journal of Energetic Materials 7 (1989), pp. 265–296.

[36] S.H. Strogatz, *Nonlinear dynamics and chaos: with applications to physics, biology, chemistry, and engineering*, Westview press, 2014.

Chapter 3

Summary of work

An investigation of detonation dynamics was performed in this thesis from two different fronts. The first addressed the two-dimensional cellular instability observed in detonations that has been correlated to detonation propagation limits. At the heart of this cellular instability are periodic shock reflections that are believed to be responsible for reaction enhancing phenomena, such as vorticity generation. Three papers investigating shock reflections under detonation-like conditions were presented in order to address some of these phenomena.

In the first paper, section 1.8, shock reflection from a wedge was simulated using a state of the art solver of the Euler equations. The paper confirmed observations that shock reflection in the Euler equations was highly dependant on resolution, solver type, and wedge implementation. Its novel contribution was finding that the initial instances of shock reflection play a crucial role on the asymptotic solution. Two reflections, identical in every way but corner geometry, can have two different outcomes depending on whether or not the corner is rounded, even as the corner size becomes small compared to the reflection.

The paper has spurred investigations on the phenomenon and its limits by other authors [124–127] but its main role in this thesis was to highlight problems with simulations of the Euler equations from ramps. These problems are addressed in the second paper, section 1.9. Shock-resolved solutions of the Navier-Stokes equations are used to remove the solver dependency and non-convergence of the Euler equations, and novel initial conditions, the reflection of a triple shock, remove issues of wedge implementation. These simulations are used to probe the role of Kelvin-Helmholtz instability in increasing turbulence, thus reaction rates, in detonations. The paper's main finding, asides from the new numerical technique, is that Kelvin-Helmholtz instability likely do not arise on the auto-ignition time scales of the shocks in detonations, however, they may become important in near-limit propagation and on the cellular scale.

The new numerical technique was used in the third paper, section 1.10, to investigate forward jetting and Mach stem bifurcations, additional shock reflection phenomena that may promote detonation propagation. The simulations were paired with new experiments of unsteady shock reflection from a plane of symmetry. Mach stem bifurcations were found in experiments, which are a rare experimental phenomenon, and mapped by simulations.

Simulations showed that the jet and bifurcation formation were delayed by viscosity, but in gross driven by hydrodynamics.

These three papers investigated shock reflection phenomena, namely the effect of viscosity on Kelvin-Helmholtz instability, forward jetting, and Mach stem bifurcation, which have previously been proposed as mechanisms that enhance reaction rates in detonations. In doing so, new numerical and experimental techniques were developed to study shock reflections under geometries similar to those of detonations.

The second part of the thesis approached detonation dynamics using one-dimensional simplified models. The simplified models allowed analysis that is otherwise difficult using the Euler or Navier-Stokes equations. The fourth paper, section 2.3, addressed the stability of detonations with multiple thermicity peaks. Its main findings were that the final speed selected by the detonation is the fastest, as determined by the generalized Chapman-Jouguet criterion. Detonations at slower speeds are unstable because faster sonic points promulgate a shock that overtakes and accelerates the front.

References

[1] J. H. Lee, *The detonation phenomenon*, vol. 2. Cambridge University Press Cambridge, 2008.

[2] M. I. Radulescu and J. H. Lee, “The failure mechanism of gaseous detonations: experiments in porous wall tubes,” *Combustion and Flame*, vol. 131, no. 1, pp. 29–46, 2002.

[3] I. Moen, A. Sulmistras, G. Thomas, D. Bjerketvedt, and P. Thibault, “Influence of cellular regularity on the behavior of gaseous detonations,” *Dynamics of explosions*, pp. 220–243, 1986.

[4] J. Shepherd, “Detonation in gases,” *Proceedings of the Combustion Institute*, vol. 32, no. 1, pp. 83–98, 2009.

[5] R. R. Bhattacharjee, *Experimental Investigation of Detonation Re-initiation Mechanisms Following a Mach Reflection of a Quenched Detonation*. Masters thesis, University of Ottawa, 2013.

[6] Y. N. Denisov and Y. K. Troshin, “Pulsating and spinning detonation of gaseous mixtures in tubes,” in *Dokl. Akad. Nauk SSSR*, vol. 125, pp. 110–113, 1959.

[7] R. A. Strehlow and J. R. Biller, “On the strength of transverse waves in gaseous detonations,” *Combustion and Flame*, vol. 13, no. 6, pp. 577–582, 1969.

[8] R. Strehlow, R. Stiles, and A. Adamczyk, “Transient studies of detonation waves,” *Astronautica Acta*, vol. 17, no. 4-5, p. 509, 1972.

[9] L. Maley, R. Bhattacharjee, S.-M. Lau-Chapdelaine, and M. I. Radulescu, “Influence of hydrodynamic instabilities on the propagation mechanism of fast flames,” *Proceedings of the Combustion Institute*, vol. 35, no. 2, pp. 2117–2126, 2015.

[10] L. Maley, *On Shock Reflections in Fast Flames*. Masters thesis, University of Ottawa, 2015.

[11] V. Subbotin, “Collision of transverse detonation waves in gases,” *Combustion, Explosion, and Shock Waves*, vol. 11, no. 3, pp. 411–414, 1975.

[12] M. I. Radulescu and B. M. Maxwell, "The mechanism of detonation attenuation by a porous medium and its subsequent re-initiation," *Journal of Fluid Mechanics*, vol. 667, pp. 96–134, 2011.

[13] R. Sorin, R. Zitoun, B. Khasainov, and D. Desbordes, "Detonation diffraction through different geometries," *Shock Waves*, vol. 19, no. 1, pp. 11–23, 2009.

[14] R. Bhattacharjee, S. S. M. Lau-Chapdelaine, G. Maines, L. Maley, and M. I. Radulescu, "Detonation re-initiation mechanism following the Mach reflection of a quenched detonation," *Proceedings of the Combustion Institute*, vol. 34, no. 2, pp. 1893–1901, 2013.

[15] Y. Mahmoudi and K. Mazaheri, "High resolution numerical simulation of the structure of 2-d gaseous detonations," *Proceedings of the Combustion Institute*, vol. 33, no. 2, pp. 2187–2194, 2011.

[16] P. Mach and M. Radulescu, "Mach reflection bifurcations as a mechanism of cell multiplication in gaseous detonations," *Proceedings of the Combustion Institute*, vol. 33, no. 2, pp. 2279–2285, 2011.

[17] P. Mach, *Bifurcating Mach Shock Reflections with Application to Detonation Structure*. Masters thesis, University of Ottawa, 2011.

[18] H. Hornung, "Regular and mach reflection of shock waves," *Annual Review of Fluid Mechanics*, vol. 18, pp. 33–58, 1986.

[19] G. Ben-Dor, *Shock wave reflection phenomena*. Springer, 2007.

[20] J. Von Neumann, *Oblique reflection of shocks*. United States Navy Department: Bureau of Ordnance, 1943.

[21] Ames research staff, "Equations, tables, and charts for compressible flow," National Advisory Committee for Aeronautics 1135, Ames Aeronautical Laboratory, Moffet Field, California, USA, 1953.

[22] H. Cabannes, "Lois de la réflexion des ondes de choc dans les écoulements plans non stationnaires," O.N.E.R.A. 80, O.N.E.R.A., 1955.

[23] L. Henderson and A. Lozzi, "Experiments on transition of mach reflexion," *Journal of Fluid Mechanics*, vol. 68, no. 01, pp. 139–155, 1975.

[24] L. Henderson and A. Lozzi, "Further experiments on transition to mach reflexion," *Journal of Fluid Mechanics*, vol. 94, no. 03, pp. 541–559, 1979.

[25] H. Hornung, H. Oertel, and R. Sandeman, "Transition to Mach reflexion of shock waves in steady and pseudosteady flow with and without relaxation," *Journal of Fluid Mechanics*, vol. 90, no. 03, pp. 541–560, 1979.

[26] H. Hornung and M. Robinson, "Transition from regular to mach reflection of shock waves part 2. the steady-flow criterion," *Journal of Fluid Mechanics*, vol. 123, pp. 155–164, 1982.

[27] C. Law and I. Glass, "Diffraction of Strong Shock Waves by a Sharp Compressive Corner," tech. rep., 1970.

[28] G. Ben-Dor and I. Glass, "Domains and boundaries of non-stationary oblique shock-wave reflexions. 1. diatomic gas," *Journal of Fluid Mechanics*, vol. 92, no. 03, pp. 459–496, 1979.

[29] H. Hornung and J. Taylor, "Transition from regular to mach reflection of shock waves part 1. the effect of viscosity in the pseudosteady case," *Journal of Fluid Mechanics*, vol. 123, pp. 143–153, 1982.

[30] H. Hornung, "The effect of viscosity on the mach stem length in unsteady strong shock reflection," in *Flow of Real Fluids*, pp. 82–91, Springer, 1985.

[31] F. J. Barbosa and B. W. Skews, "Experimental confirmation of the von Neumann theory of shock wave reflection transition," *Journal of Fluid Mechanics*, vol. 472, pp. 263–282, 2002.

[32] M. K. Hryniewicki, *On the Transition Boundary Between Regular and Mach Reflections From a Wedge in Inviscid and Polytropic Gases*. Ph.D. thesis, University of Toronto, 2016.

[33] M. K. Hryniewicki, J. J. Gottlieb, and C. P. T. Groth, "Transition boundary between regular and Mach reflections for a moving shock interacting with a wedge in inviscid and polytropic air," *Shock Waves*, pp. 1–28, 2016.

[34] E. I. Vasilev, T. Elperin, and G. Ben-Dor, "Analytical reconsideration of the von neumann paradox in the reflection of a shock wave over a wedge," *Physics of Fluids*, vol. 20, no. 4, p. 046101, 2008.

[35] A. Semenov, M. Berezkina, and I. Krasovskaya, "Classification of shock wave reflections from a wedge. part 1: Boundaries and domains of existence for different types of reflections," *Technical Physics*, vol. 54, no. 4, pp. 491–496, 2009.

[36] A. Semenov, M. Berezkina, and I. Krasovskaya, "Classification of shock wave reflections from a wedge. part 2: Experimental and numerical simulations of different types of mach reflections," *Technical Physics*, vol. 54, no. 4, pp. 497–503, 2009.

[37] A. Semenov, M. Berezkina, and I. Krassovskaya, "Classification of pseudo-steady shock wave reflection types," *Shock Waves*, vol. 22, no. 4, pp. 307–316, 2012.

[38] H. Li and G. Ben-Dor, "Reconsideration of pseudo-steady shock wave reflections and the transition criteria between them," *Shock waves*, vol. 5, no. 1-2, pp. 59–73, 1995.

[39] S. Ando, "Pseudo-Stationary Oblique Shock-Wave Reflection in Carbon Dioxide-Domains and Boundaries," Technical Note 231, University of Toronto Institute for Aerospace Studies, Apr. 1981.

[40] B. Zaslavskii and R. Safarov, "Mach reflection of weak shock waves from a rigid wall," *Journal of Applied Mechanics and Technical Physics*, vol. 14, no. 5, pp. 624–629, 1973.

[41] R. Courant and K. O. Friedrichs, *Supersonic flow and shock waves*, vol. 21. Springer Science & Business Media, 1977.

[42] G. Ben-Dor, "A reconsideration of the three-shock theory for a pseudo-steady mach reflection," *Journal of Fluid Mechanics*, vol. 181, pp. 467–484, 1987.

[43] G. L. Brown and A. Roshko, "On density effects and large structure in turbulent mixing layers," *Journal of Fluid Mechanics*, vol. 64, no. 04, pp. 775–816, 1974.

[44] P. Woodward and P. Colella, "The numerical simulation of two-dimensional fluid flow with strong shocks," *Journal of Computational Physics*, vol. 54, no. 1, pp. 115–173, 1984.

[45] A. Rikanati, O. Sadot, G. Ben-Dor, D. Shvarts, T. Kuribayashi, and K. Takayama, "Shock-wave mach-reflection slip-stream instability: a secondary small-scale turbulent mixing phenomenon," *Physical review letters*, vol. 96, no. 17, p. 174503, 2006.

[46] A. Rikanati, O. Sadot, G. Ben-Dor, D. Shvarts, T. Kuribayashi, and K. Takayama, "A secondary small-scale turbulent mixing phenomenon induced by shock-wave mach-reflection slip-stream instability," in *Shock Waves*, pp. 1347–1352, Springer, 2009.

[47] S. Rubidge, *Kelvin-Helmholtz Instability on the Mach reflection shear layer.* Masters thesis, 2013.

[48] S. Rubidge and B. Skews, "Shear-layer instability in the mach reflection of shock waves," *Shock Waves*, vol. 24, no. 5, pp. 479–488, 2014.

[49] R. E. Hall, B. Skews, and R. Paton, "The compressible shear layer of a Mach Reflection," in *30th International Symposium on Shock Waves 1*, pp. 659–663, Springer, 2017.

[50] R. A. Strehlow, *Fundamentals of combustion.* International Textbook Co., 1968.

[51] L. Massa, J. Austin, and T. Jackson, "Triple-point shear layers in gaseous detonation waves," *Journal of Fluid Mechanics*, vol. 586, pp. 205–248, 2007.

[52] H. Glaz, P. Colella, I. Glass, and R. Deschambault, "A numerical study of oblique shock-wave reflections with experimental comparisons," *Proceedings of the Royal Society of London. A. Mathematical and Physical Sciences*, vol. 398, no. 1814, pp. 117–140, 1985.

[53] H. Glaz, P. Colella, I. Glass, and R. Deschambault, "A detailed numerical, graphical, and experimental study of oblique shock wave reflections," *Lawrence Berkeley National Laboratory*, 1985.

[54] P. Colella and H. M. Glaz, "Numerical calculation of complex shock reflections in gases," in *Ninth International Conference on Numerical Methods in Fluid Dynamics*, pp. 154–158, Springer, 1985.

[55] X. Shi, Y. Zhu, X. Luo, and J. Yang, "High temperature effects in moving shock reflection with protruding Mach stem," *Theoretical and Applied Mechanics Letters*, vol. 6, no. 5, pp. 222–225, 2016.

[56] H. Li and G. Ben-Dor, "Analysis of double-mach-reflection wave configurations with convexly curved mach stems," *Shock Waves*, vol. 9, no. 5, pp. 319–326, 1999.

[57] L. Henderson, E. Vasilev, G. Ben-Dor, and T. Elperin, "The wall-jetting effect in mach reflection: theoretical consideration and numerical investigation," *Journal of Fluid Mechanics*, vol. 479, pp. 259–286, 2003.

[58] E. Vasilev, G. Ben-Dor, T. Elperin, and L. Henderson, "The wall-jetting effect in Mach reflection: NavierStokes simulations," *Journal of Fluid Mechanics*, vol. 511, pp. 363–379, 2004.

[59] X. Shi, Y. Zhu, X. Luo, and J. Yang, "Numerical Study on Double Mach reflection of Strong Moving Shock involving Laminar Transport," (Xiamen, China), 2017.

[60] J. M. Austin, *The role of instability in gaseous detonation*. PhD, 2003.

[61] D. G. Goodwin, H. K. Moffat, and R. L. Speth, "Cantera: An object-oriented software toolkit for chemical kinetics, thermodynamics, and transport processes." http://www.cantera.org, 2015. Version 2.2.0.

[62] W. Sutherland, "The viscosity of gases and molecular force," *Philosophical Magazine*, vol. 36, no. 223, pp. 507–531, 1893.

[63] S. S.-M. Lau-Chapdelaine, G. Sharpe, and M. I. Radulescu, "Viscous Solutions of the Triple Shock Reflection Problem," in *Proceedings of the 25th International Colloquium on the Dynamics of Explosions and Reactive Systems*, (Leeds UK), 2015.

[64] J. Quirk, "Amrita - a computational facility (for CFD modelling)," in *VKI 29th CFD lecture series*, Feb. 1998.

[65] S. Falle and S. Komissarov, "An upwind numerical scheme for relativistic hydrodynamics with a general equation of state," *Monthly Notices of the Royal Astronomical Society*, vol. 278, no. 2, pp. 586–602, 1996.

[66] J. Shi, Y.-T. Zhang, and C.-W. Shu, "Resolution of high order WENO schemes for complicated flow structures," *Journal of Computational Physics*, vol. 186, no. 2, pp. 690–696, 2003.

[67] R. Samtaney and D. Pullin, "On initial-value and self-similar solutions of the compressible euler equations," *Physics of Fluids*, vol. 8, no. 10, pp. 2650–2655, 1996.

[68] M. Sun and K. Takayama, "A note on numerical simulation of vortical structures in shock diffraction," *Shock Waves*, vol. 13, no. 1, pp. 25–32, 2003.

[69] M. J. Berger and P. Colella, "Local adaptive mesh refinement for shock hydrodynamics," *Journal of computational Physics*, vol. 82, no. 1, pp. 64–84, 1989.

[70] M. Cramer, "Numerical estimates for the bulk viscosity of ideal gases," *Physics of Fluids*, vol. 24, no. 6, 2012.

[71] P. Thompson, *Compressible-Fluid Dynamics*. Rensselaer Polytechnic Institute, 3 ed., 1988.

[72] E. F. Toro, *Riemann solvers and numerical methods for fluid dynamics: a practical introduction*. Springer Science & Business Media, 2013.

[73] S. K. Godunov, "A difference method for numerical calculation of discontinuous solutions of the equations of hydrodynamics," *Matematicheskii Sbornik*, vol. 89, no. 3, pp. 271–306, 1959.

[74] K. Takayama and Z. Jiang, "Shock wave reflection over wedges: a benchmark test for CFD and experiments," *Shock Waves*, vol. 7, no. 4, pp. 191–203, 1997.

[75] S.-M. Lau-Chapdelaine and M. I. Radulescu, "Non-uniqueness of solutions in asymptotically self-similar shock reflections," *Shock Waves*, vol. 23, no. 6, pp. 595–602, 2013.

[76] J. J. Quirk, *A contribution to the great Riemann solver debate*. Springer, 1997.

[77] K. Takayama, G. Ben-Dor, and J. Gotoh, "Regular to Mach reflection transition in truly nonstationary flows-Influence of surface roughness," *AIAA Journal*, vol. 19, no. 9, pp. 1238–1240, 1981.

[78] K. Takayama, J. Gotoh, and G. Ben-Dor, "Influence of surface roughness on the shock transition in quasi-stationary and truly non-stationary flow," in *Shock Tubes and Waves: Proceedings of the Thirteenth International Symposium on Shock Tubes and Waves*, (New York), State University of New York Press, 1981.

[79] G. Ben-Dor, G. Mazor, K. Takayama, and O. Igra, "Influence of surface roughness on the transition from regular to Mach reflection in pseudo-steady flows," *Journal of Fluid Mechanics*, vol. 176, pp. 333–356, 1987.

[80] S. Xu, T. Aslam, and D. S. Stewart, "High resolution numerical simulation of ideal and non-ideal compressible reacting flows with embedded internal boundaries," 1997.

[81] S. Falle, "Self-similar jets," *Monthly Notices of the Royal Astronomical Society*, vol. 250, no. 3, pp. 581–596, 1991.

[82] S. S. Lau-Chapdelaine and M. I. Radulescu, "Viscous solution of the triple-shock reflection problem," *Shock Waves*, vol. 26, no. 5, pp. 551–560, 2016.

[83] M. Short and G. J. Sharpe, "Pulsating instability of detonations with a two-step chain-branching reaction model: theory and numerics," *Combustion Theory and Modelling*, vol. 7, no. 2, pp. 401–416, 2003.

[84] P. Blythe, A. Kapila, and M. Short, "Homogeneous ignition for a three-step chain-branching reaction model," *Journal of engineering mathematics*, vol. 56, no. 2, pp. 105–128, 2006.

[85] G. J. Sharpe and N. Maflahi, "Homogeneous explosion and shock initiation for a three-step chain-branching reaction model," *Journal of Fluid Mechanics*, vol. 566, pp. 163–194, 2006.

[86] P. Clavin and F. A. Williams, "Dynamics of planar gaseous detonations near Chapman-Jouguet conditions for small heat release," *Combustion Theory and Modelling*, vol. 6, no. 1, pp. 127–139, 2002.

[87] L. M. Faria, A. R. Kasimov, and R. R. Rosales, "Theory of weakly nonlinear self-sustained detonations," *Journal of Fluid Mechanics*, vol. 784, pp. 163–198, 2015.

[88] R. R. Rosales and A. Majda, "Weakly nonlinear detonation waves," *SIAM Journal on Applied Mathematics*, vol. 43, no. 5, pp. 1086–1118, 1983.

[89] W. Fickett, "Detonation in miniature," *Am. J. Phys*, vol. 47, no. 12, pp. 1050–1059, 1979.

[90] W. Fickett, *Introduction to detonation theory*, vol. 5. Univ of California Press, 1985.

[91] A. Majda, "A qualitative model for dynamic combustion," *SIAM Journal on Applied Mathematics*, vol. 41, no. 1, pp. 70–93, 1981.

[92] J. M. Burgers, "A mathematical model illustrating the theory of turbulence," *Advances in applied mechanics*, vol. 1, pp. 171–199, 1948.

[93] J. J. Erpenbeck, "Stability of Idealized One-Reaction Detonations," *Physics of Fluids*, vol. 7, no. 5, pp. 684–696, 1964.

[94] W. Fickett and W. W. Wood, "Flow Calculations for Pulsating One-Dimensional Detonations," *Physics of Fluids*, vol. 9, no. 5, pp. 903–916, 1966.

[95] S. H. Strogatz, *Nonlinear dynamics and chaos: with applications to physics, biology, chemistry, and engineering*. Westview press, 2014.

[96] H. Ng, A. Higgins, C. Kiyanda, M. Radulescu, J. Lee, K. Bates, and N. Nikiforakis, "Nonlinear dynamics and chaos analysis of one-dimensional pulsating detonations," *Combustion Theory and Modelling*, vol. 9, no. 1, pp. 159–170, 2005.

[97] A. K. Henrick, T. D. Aslam, and J. M. Powers, "Simulations of pulsating one-dimensional detonations with true fifth order accuracy," *Journal of Computational Physics*, vol. 213, no. 1, pp. 311–329, 2006.

[98] J. Tang and M. Radulescu, "Dynamics of shock induced ignition in Ficketts model: Influence of ," *Proceedings of the Combustion Institute*, vol. 34, no. 2, pp. 2035–2041, 2013.

[99] M. I. Radulescu and J. Tang, "Nonlinear dynamics of self-sustained supersonic reaction waves: Ficketts detonation analogue," *Physical review letters*, vol. 107, no. 16, p. 164503, 2011.

[100] A. R. Kasimov, L. M. Faria, and R. R. Rosales, "Model for shock wave chaos," *Physical review letters*, vol. 110, no. 10, p. 104104, 2013.

[101] J. Tang, *Study of the Instability and Dynamics of Detonation Waves using Fickett's Analogue to the Reactive Euler Equations*. Masters thesis, University of Ottawa, 2013.

[102] A. Bellerive and M. I. Radulescu, "A nonlinear evolution equation for pulsating detonations using Fickett's model with chain branching kinetics," in *Fifteenth International Detonation Symposium*, (San-Francisco, California, USA), 2014.

[103] A. Bellerive and M. I. Radulescu, "Chaos in a Third Order Nonlinear Evolution Equation for Pulsating Detonations using Ficketts Model," in *Proceedings of the 25th ICDERS*, (Leeds UK), 2015.

[104] S. Lau-Chadeplaine, A. Bellerive, and M. Radulescu, "Stability Characteristics of Pulsating One-Dimensional Detonations using a Simple Analogue," in *ICTAM*, vol. XXIV, (Montreal, Canada), 2016.

[105] M. Short, "A nonlinear evolution equation for pulsating Chapman-Jouguet detonations with chain-branching kinetics," *Journal of Fluid Mechanics*, vol. 430, pp. 381–400, 2001.

[106] W. Fickett and W. Davis, *Detonation Theory and Experiment*. New York: Dover Publications, INC, 1979.

[107] L. M. Faria and A. R. Kasimov, "Qualitative modeling of the dynamics of detonations with losses," *Proceedings of the Combustion Institute*, 2014.

[108] F. Zhang, "Detonation in reactive solid particle-gas flow," *Journal of propulsion and power*, vol. 22, no. 6, pp. 1289–1309, 2006.

[109] E. Afanasieva, V. Levin, and Y. V. Tunik, "Multifront combustion of two-phase medium," *Shock Waves, Explosions, and Detonations: AIAA Progress in Astronautics and Aeronautics,(edited by JR Bowen, N. Manson, AK Oppenheim, and RI Soloukhin)*, pp. 394–413, 1983.

[110] B. Khasainov and B. Veyssiere, “Steady, plane, double-front detonations in gaseous detonable mixtures containing a suspension of aluminum particles,” *Dynamics of explosions*, pp. 284–299, 1988.

[111] B. Veyssiere and B. Khasainov, “Structure and multiplicity of detonation regimes in heterogeneous hybrid mixtures,” *Shock Waves*, vol. 4, no. 4, pp. 171–186, 1995.

[112] F. Zhang, “Detonation of gas-particle flow,” in *Shock Wave Science and Technology Reference Library, Vol. 4*, pp. 87–168, Springer, 2009.

[113] B. Veyssiere, “Double-front detonations in gas-solid particles mixtures,” *Dynamics of Shock Waves, Explosions, and Detonations, Progress in Astronautics and Aeronautics*, vol. 94, pp. 264–276, 1984.

[114] M. Baer and J. Nunziato, “A two-phase mixture theory for the deflagration-to-detonation transition (DDT) in reactive granular materials,” *International journal of multiphase flow*, vol. 12, no. 6, pp. 861–889, 1986.

[115] R. Saurel and O. Lemetayer, “A multiphase model for compressible flows with interfaces, shocks, detonation waves and cavitation,” *Journal of Fluid Mechanics*, vol. 431, pp. 239–271, 2001.

[116] F. E. Marble, “Dynamics of dusty gases,” *Annual Review of Fluid Mechanics*, vol. 2, no. 1, pp. 397–446, 1970.

[117] H. Miura and I. I. Glass, “On a dusty-gas shock tube,” in *Proceedings of the Royal Society of London A: Mathematical, Physical and Engineering Sciences*, vol. 382, pp. 373–388, The Royal Society, 1982.

[118] H. Miura and I. I. Glass, “On the passage of a shock wave through a dusty-gas layer,” in *Proceedings of the Royal Society of London A: Mathematical, Physical and Engineering Sciences*, vol. 385, pp. 85–105, The Royal Society, 1983.

[119] H. Miura and I. Glass, “Development of the flow induced by a piston moving impulsively in a dusty gas,” in *Proceedings of the Royal Society of London A: Mathematical, Physical and Engineering Sciences*, vol. 397, pp. 295–309, The Royal Society, 1985.

[120] H. Miura, T. Saito, and I. Glass, “Shock-wave reflection from a rigid wall in a dusty gas,” in *Proceedings of the Royal Society of London A: Mathematical, Physical and Engineering Sciences*, vol. 404, pp. 55–67, The Royal Society, 1986.

[121] T. Saito, “Numerical analysis of dusty-gas flows,” *Journal of computational physics*, vol. 176, no. 1, pp. 129–144, 2002.

[122] B. Veyssiere and B. Khasainov, “A model for steady, plane, double-front detonations (DFD) in gaseous explosive mixtures with aluminum particles in suspension,” *Combustion and Flame*, vol. 85, no. 1, pp. 241–253, 1991.

[123] C. B. Henderson, "Drag coefficients of spheres in continuum and rarefied flows," *AIAA journal*, vol. 14, no. 6, pp. 707–708, 1976.

[124] F. A. Previtali, E. Timofeev, and H. Kleine, "On unsteady shock wave reflections from wedges with straight and concave tips," in *45th AIAA Fluid Dynamics Conference*, 2015.

[125] F. A. Previtali, H. Kleine, and E. Timofeev, "New Findings on the Shock Reflection from Wedges with Small Concave Tips," in *Proceedings of the 22nd International Shock Interaction Symposium*, pp. 385–396, Springer, 2016.

[126] E. Timofeev, F. A. Previtali, and H. Kleine, "On unsteady shock wave reflection from a concave cylindrical surface," in *Proceedings of the 22nd International Shock Interaction Symposium*, pp. 367–383, Springer, 2016.

[127] F. A. Previtali, E. Timofeev, and H. Kleine, "On InMR-TRR transition on a concave cylindrical reflector," in *Proceedings of the 31st International Symposium on Shock Waves*, 2017.